Radiometric Thermometry for Wearable Deep Tissue Monitoring

by

Parisa Momenroodaki

B.S., Shariaty University, 2008

A thesis submitted to the

Faculty of the Graduate School of the

University of Colorado in partial fulfillment

of the requirements for the degree of

Doctor of Philosophy

Department of Electrical, Computer, and Energy Engineering

2017

This thesis entitled:
Radiometric Thermometry for Wearable Deep Tissue Monitoring
written by Parisa Momenroodaki
has been approved for the Department of Electrical, Computer, and Energy Engineering

Professor Zoya Popović

Professor Edward Kuester

Date

The final copy of this thesis has been examined by the signatories, and we find that both the content and the form meet acceptable presentation standards of scholarly work in the above mentioned discipline.

Momenroodaki, Parisa (Ph.D., Electrical Engineering)

Radiometric Thermometry for Wearable Deep Tissue Monitoring

Thesis directed by Professor Zoya Popović

Microwave thermometry is an attractive non-invasive method for measuring internal body temperature. This approach has the potential of enabling a wearable device that can continuously monitor core body temperature. There are a number of health-related applications in both diagnostics and therapy, which can benefit from the knowledge of core body temperature. However, there are a limited number of device solutions, which are usually not wearable or cannot continuously monitor internal body temperature non-invasively. In this thesis, a possible path toward implementing such a thermometer is presented. The device operates in the "quiet" frequency band of 1.4 GHz which is chosen as a compromise between sensing depth and radio frequency interference (RFI).

A major challenge in microwave thermometry is detecting small temperature variations of deep tissue layers from surface (skin) measurements. The type and thickness of tissue materials significantly affect the design of the probe, which has the function of receiving black-body radiation from tissues beneath it and coupling the power to a sensitive radiometric receiver. High dielectric constant contrast between skin, fat (/bone), and muscle layers suggests structures with dominant tangential component of the electric field, such as a patch or slot. Adding a layer of low-loss, low-dielectric constant superstrate can further reduce the contribution of superficial tissue layers in the received thermal noise. Several probe types are designed using a full-wave electromagnetic simulator, with a goal of maximizing the power reception from deep tissue layers. The designs are validated with a second software tool and various measurements. A stable, narrow-band, and highly sensitive radiometer is developed, enabling the device to operate in a non-shielded RF environment. To use the microwave thermometer in a RF congested environment, not only narrow-band probe and radiometers are used but an additional probe is introduced for observing the environmental

interference. By applying an adaptive filter, the effect of RFI is mitigated in long-term measurements. Several solid and liquid tissue phantoms, required for accurate modeling of the probe and human body interaction, are also developed. The concept of human body microwave thermometry is validated through several measurements on the single-layer and multiple-layer tissue phantoms as well as on the surface of the human body, specifically on the cheek where the internal temperature can easily be changed and independently measured with a thermocouple. Measurement results prove the capability of the device in tracking the temperature of buried tissue layer phantoms to within 0.2K, as well as monitoring internal human body temperature.

Dedication

To my family

Contents

Chapter

Tables

Table

Figures

Figure

Chapter 1

Introduction

Contents

1.1 Motivation

There are a number of health-related applications, ranging from monitoring and diagnostics to therapy, which benefit from the knowledge of internal (core) body temperature. The internal temperature of the human body can be considerably different than the temperature of the skin. Rapid changes in internal temperature do not necessarily result in changes in skin temperature [1]. The difference between core body temperature (e.g. heart) and skin varies up to $\pm 2^{\circ}$ K over the

circadian cycle for a healthy person [2]. As shown in Figure 1.1, the skin and muscle temperature vary in an opposite directions during exercise. While muscle temperature increases with increasing exercise intensity, the skin temperature decreases due to sweating (evaporative cooling).

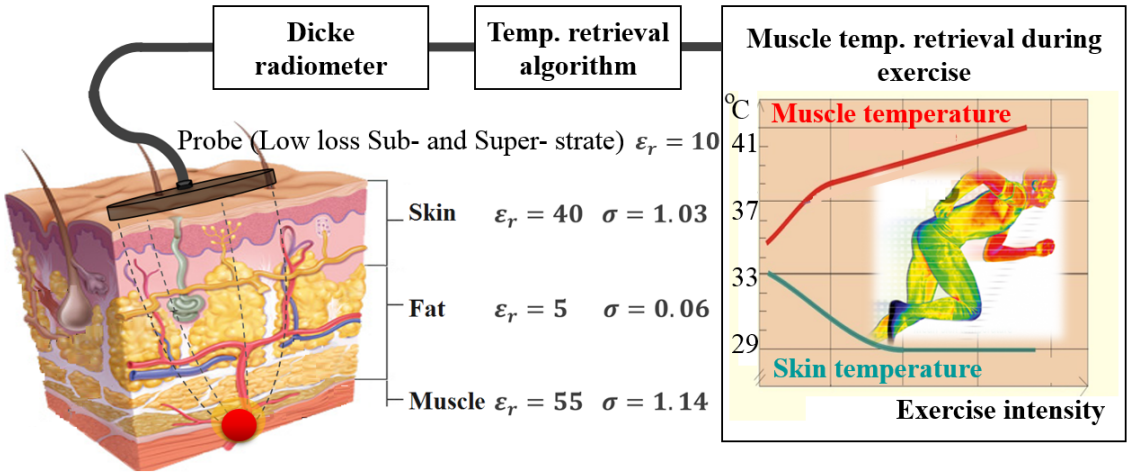

Figure 1.1: Skin and muscle temperatures follow different trends during exercise. The goal of microwave radiometry is noninvasive muscle temperature tracking. Human body model is taken from [3] and the temperature-exercise profile is from [4].

Tracking the difference between internal and skin temperature is important, for example, in diagnostics for soldiers under heavy training, and fire fighters and astronauts under challenging ambient conditions for preventing hypothermia, hyperthermia, and heat stroke. It is also important in diagnostics for patients with sleep disorders. Additionally, it has been shown that disrupted circadian rhythm can result in seasonal affective disorder [5], type-2 diabetes [6], and heart disease [7]. Excessively elevated core temperatures of athletes under heavy training can even lead to death [8]. Most internal body temperature measurement methods can measure temperature after ending physical activity, at this point overheating is already a risk.

In medical treatment, it is important to measure internal tissue temperature in cancer detection [9], monitoring drug delivery for cancer treatment [10], hyperthermia temperature control [11]-[12], and hypothermic neural rescue of infants suffering from hypoxia-ischemia [13].

1.2 Existing Methods

Existing internal temperature measurements are illustrated in Figure 1.2 and include internal thermometers, which are generally invasive, and external which are not portable, are expensive, and potentially influenced by environmental conditions.

1.2.1 Internal thermometers

Internal thermometers, such as oral, rectal and esophageal (Figure 1.2a-c), are not portable, not convenient for long-term monitoring, difficult to insert, and can cause irritation [14]. Indigestible telemetric pills measure temperature while in the digestive track for a limited period of time [15], but are not reusable, and their precise position in the body is unknown. Also, it has been shown that drinking cool fluids increases the error to more than 6°C. Surgically inserted thermometers (implantable thermometers) are not non-invasive.

1.2.2 External thermometers

External methods, such as Magnetic Resonance Imaging (MRI) (Figure 1.2-d), grant high spatial temperature resolution, but are expensive and not portable [16]. In MRI thermometry, a particular temperature sensitive MRI property is monitored. Extracting this parameter can be proton density, diffusion contrast, relaxation times, magnetization transfer ratio, intermolecular zero-quantum coherence, or water proton resonance frequency [16]. Other active external thermometers, such as computed tomography (CT) imaging [17] and ultrasound [18], use other temperature sensitive parameters such as CT number and speed of sound. Active methods, such as ionizing x-rays, can in some situations induce cancer [19]. Another method, Zero Heat Flux (ZHF), eliminates heat loss to the environment by an isothermal path. As shown in Figure 1.2-e, the sensor consists of two thermometers, separated by an insulator, and covered by a heater. The heater is controlled to keep the two temperatures identical. An isothermal tunnel develops below the skin surface, which makes subcutaneous temperature equal to skin temperature where it can be measured non-invasivly

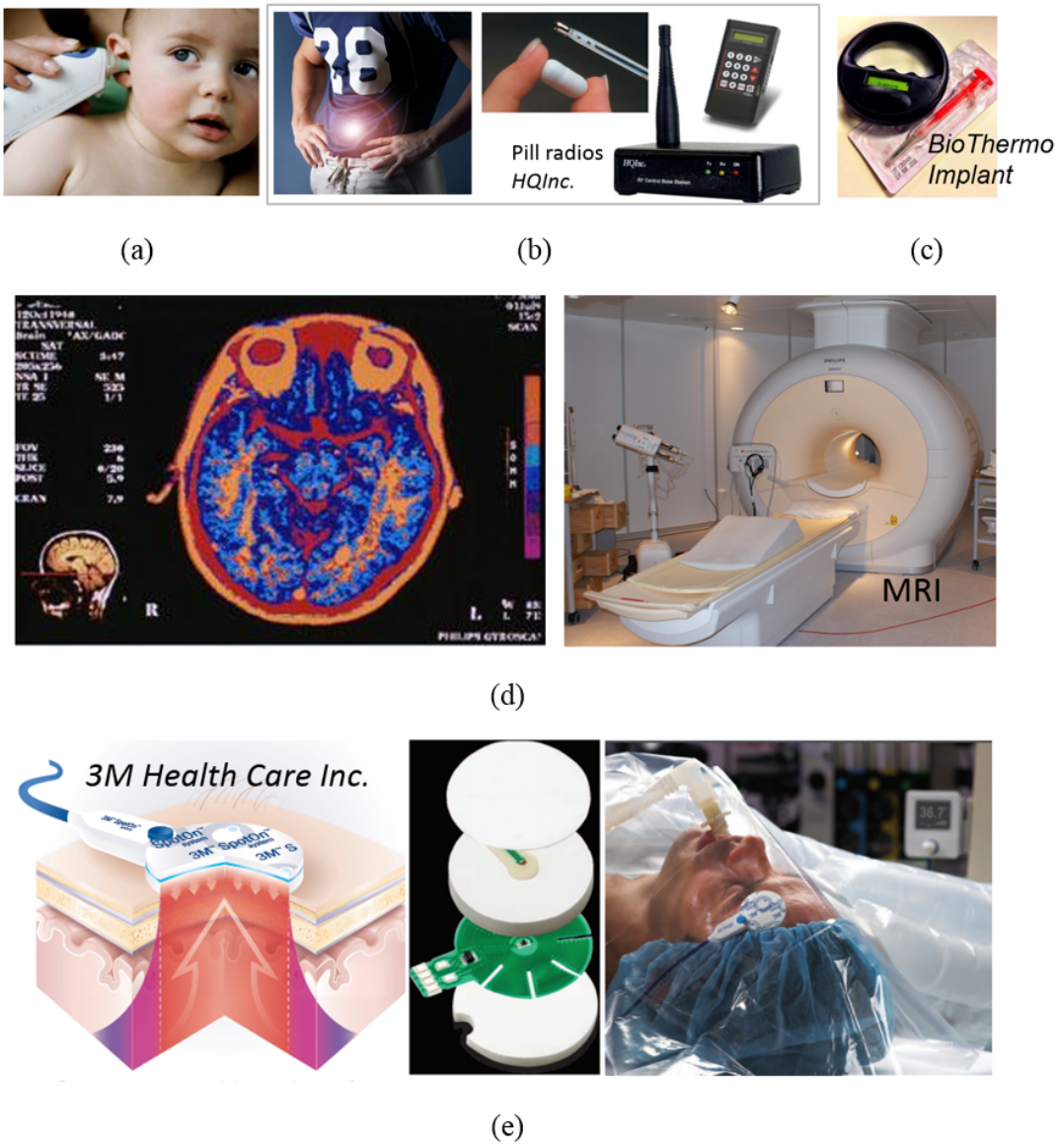

Figure 1.2: Existing internal and external thermometers: (a) esophageal (b) telemetric pill, (c) implant thermomter. (d) MRI thermometry; (e) zero heat flux, where sensor is placed on the skin during surgery. The sensor consists of two thermometers, separated by an insulator, and covered by a heater. The controlled heater keeps the subcutaneous temperature equal to skin temperature where it can be measured non-invasivly [1].

[1]. This method is currently limited to hospitals for measuring patient subcutaneous temperature during surgery. This approach becomes less accurate for thick tissue layers that are poor thermal conductors, such as fat.

1.3 Microwave thermometry and thermal noise

Electrical noise is a random variable with a voltage/current mean equal to zero, but with non-zero power. The dominant noise from passive devices at non-zero temperatures through the microwave frequency range is thermal (Johnson, white) noise.

A clear treatment of black body radiation and thermal noise is given in the classic paper by Oliver [20] and starts from the basic laws of thermodynamics. The thermal spectral power density is first derived on a matched transmission line in thermal equilibrium, showing that under the assumption that $hf << kT$, both terminations emit a power spectral density equal to kT, where k is the Boltzmann and h the Plank constant. This conclusion is based on mode counting in a transmission line resonator which is a one-dimensional electromagnetic system, where we can notice that there is no frequency dependence in the approximate expression for the total noise power spectral density kT. By extending the derivation to three dimensions, we find that the three-dimensional mode density results in a power spectral density that depends on the square of frequency, and interestingly enough, the antenna effective area theorem results from this calculation.

The relevance of these results to the work in this thesis are fundamental: in order to measure the temperature of an object, one measures the noise power radiated in a known bandwidth B and it is straightforward to then calculate T. The radiometer has a one-dimensional port on one side, where $p = kTB$, and a three-dimensional port on the other side where an antenna (in the far field) or probe (in the near field) receives a power that has to be equivalent to kTB for a matched system.

In three dimensions, the cavity mode density increases as the square of frequency and the total spectral volume mode density becomes [20], [21], and [22]

$$m_3 = \frac{8\pi f^2}{c^3}(1/m^3.Hz) \tag{1.1}$$

The average blackbody energy density in the cavity is equal to total number of modes times the energy density $\overline{W}$ in the cavity

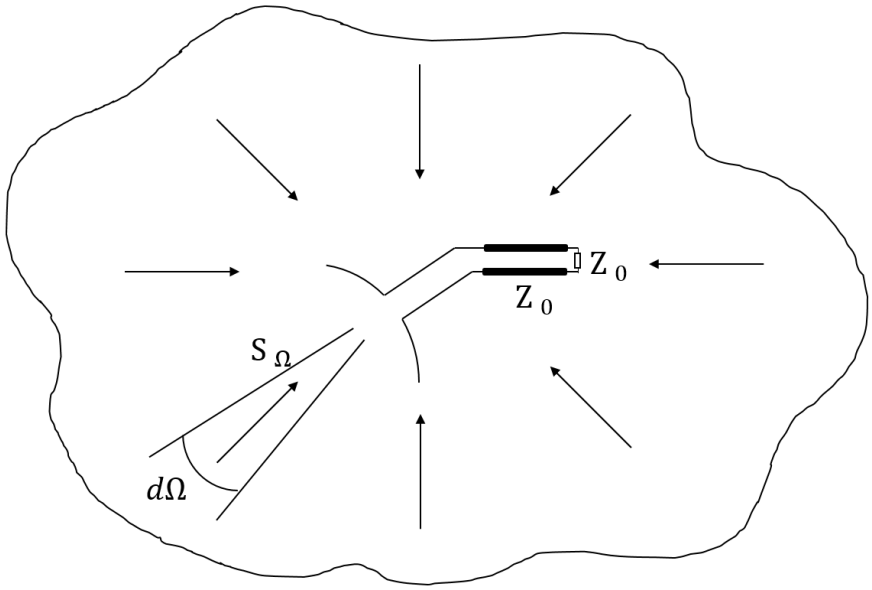

Figure 1.3: An antenna and a terminated transmission line inside a large enclosure [21] and [22].

$$\rho_3 = m_3\overline{W} = \frac{8\pi h f^3}{c^3}\frac{1}{e^{hf/kT}-1}(J/m^3.c.s) \tag{1.2}$$

In three dimensions, the black-body object can be treated as a matched transmission line connected to an antenna inside an anechoic chamber at a constant temperate T in thermal equilibrium, Figure1.3 [21]. The transmission-line feed termination generate thermal noise power which is delivered to the antenna, radiated out to the chamber and absorbed by the walls. Meanwhile, the antenna receives the noise power from the enclosure and delivers it to the transmission line. The two processes must balance in thermal equilibrium. The noise energy flux incident on the antenna is S_Ω, and the the noise power per unit area incident on the antenna from a small cone $d\Omega$ is $S_\Omega d\Omega$. If the enclosure is large S_Ω will be the same for every direction. Since the free-space wave travels at the speed of light c, the noise energy density (per unit volume) is $S_\Omega d\Omega/c$. The total noise energy density at the point is a summation of contributions from all directions. This must be just the black-body radiation density ρ, so that we can write

$$\rho = \int (S_\Omega/c)d\Omega = 4\pi S_\Omega/c \tag{1.3}$$

or

$$S_\Omega = \rho c/4\pi \tag{1.4}$$

According to the definition of the effective aperture A_{eff} of an antenna, the amount of power received by the antenna from direction (θ, ϕ) is

$$dP = \frac{1}{2} S_\Omega A_{eff}(\theta, \phi) d\Omega \tag{1.5}$$

where $A_{eff}(\theta, \phi)$ is the effective aperture in that particular direction. The factor of $1/2$ enters because the noise energy has random polarization and so only half of this energy is properly polarized to be received by the antenna [21] and [22]. Therefore, using (1.4), the total power received by the antenna can be written as

$$P = \frac{c\rho}{8\pi} \int A_e(\theta, \phi) d\Omega \tag{1.6}$$

The effective aperture intergrated over all directions is equal to λ^2. Therefore, using 1.2, the noise power received by the antenna is

$$P = \frac{hfB}{e^{hf/kT} - 1} \tag{1.7}$$

This equation under the condition of $hf/kT << 1$ again can be approximated as

$$P = kTB \tag{1.8}$$

which is exactly the same as the noise power generated by the termination and radiated from the antenna. This result is relevant to the work in this thesis, as we are dealing with both one and three-dimensional noise power as a means to measure temperature.

1.4 Background

There has been some research in microwave core-body thermometry, mainly limited to infant brain temperature measurements [12], [23], [24], for monitoring astronaut temperature in space-suits [25], and for monitoring abnormal bladder functions [26]. In these cases typically the environment is shielded or relatively large shielded probes are used, resulting in non-wearable devices. Other works in this field includes an approach with two waveguide probes with water bolus and a multi-band radiometer at 1-4 GHz were used to retrieve temperature profile within the cooled head model (detailed in Figure 1.4-a) [12], [23] and [13]. The potential of multi-frequency microwave radiometry for detecting the location of a hot spot (tumor) inside the muscle phantom cylinder has been investigated in [27]. A company in Russia has developed a radiometer instrument for breast cancer detection suitable for use in hospitals (Figure 1.4-b) [28]. In 2004, [29] presented a cavity for detecting the temperature profile of a simplified human head model (Figure 1.5-a). A near-field patch antenna array for the radiometric sensing of food temperature is described in [30]. A combination of microwave heating and radiometry as a means of the noninvasive measurement of blood perfusion is investigate in [31], [32], [33]. A non-contact cavity-backed slot probe was developed to work at 1.4 GHz on a tissue phantom stack of high-permittivity models for skin, muscle and blood [25] (Figure 1.5-b). Different radiometer and probe designs have been investigated to work on human head and kidney phantoms [34] and [35] (Figure 1.5-c). A dual-frequency radiometer at 1.4 GHz and 2.7 GHz for temperature retrieval of a three-layer tissue phantom is investigated in [36] (Figure 1.4-c). The efficiency of a log-spiral probe was investigated on the human head phantom in [37].

Figure 1.6 shows the block diagram of a wearable internal body temperature measurement system. The power received from tissue layers by the narrowband probe is coupled to a Dicke radiometer, which consist of a switch that is required for calibration, a low-noise amplifier (LNA) followed by band-pass filters, and a diode detector circuit. The hot and cold loads are used for continuous temperature calibration of the radiometer. The detector output is a DC voltage which can be integrated over time to increase the signal-to-noise ratio (SNR). This output is digitized,

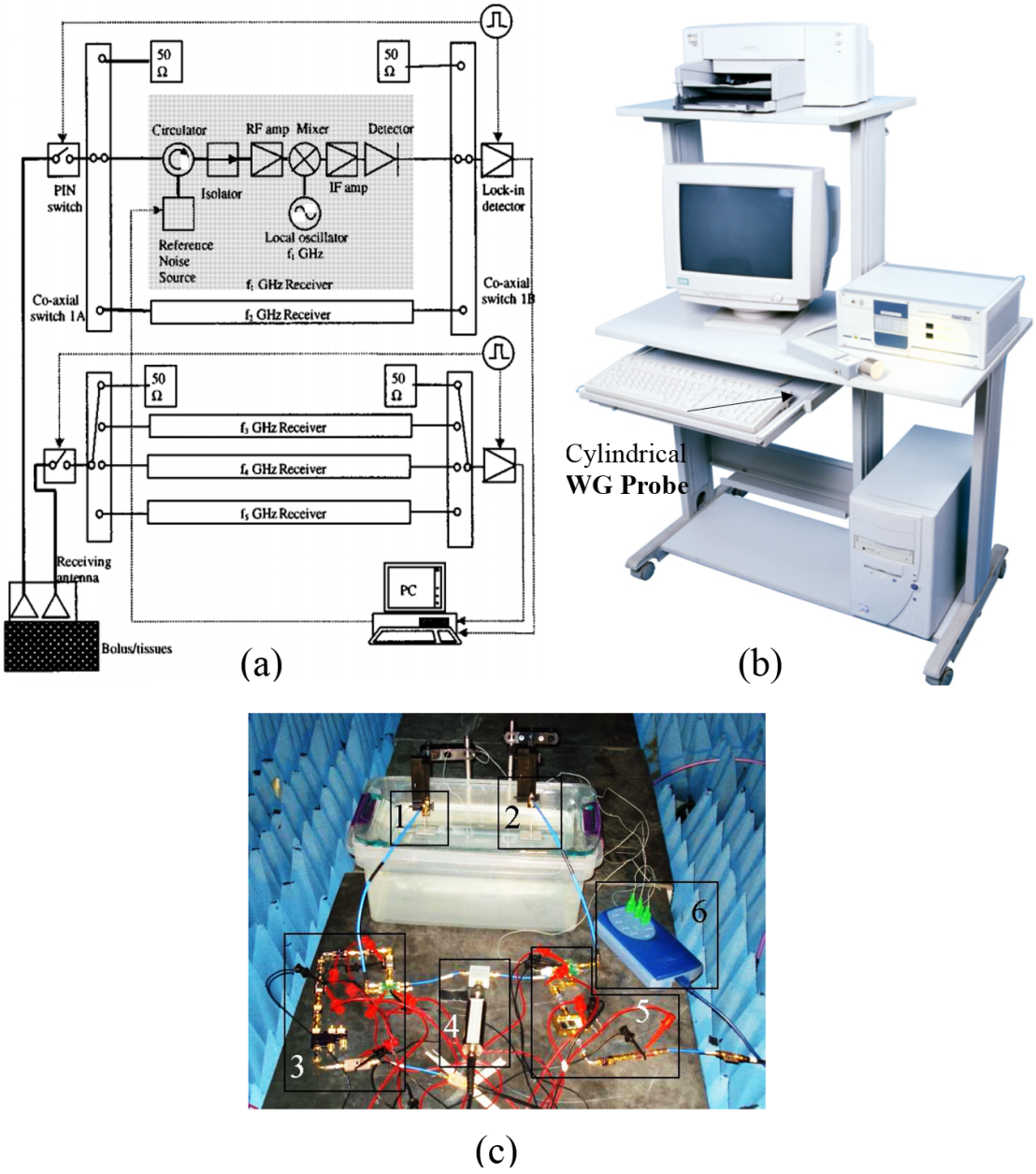

Figure 1.4: Review of some of previous works in multi-frequency microwave thermometry. (a) A 400 MHz bandwidth 5-band radiometer uses rectangular waveguide for detecting brain phantom temperature under skull and bone with the accuracy of 1.5C [12], [23], [24], (b) A double-frequency radiometer is used for locating breast cancer tumors. Probe is a cylindrical waveguide and power consumption is 5 W and device mass is 4 Kg [28], (c) A double-frequency radiometer is used to detect temperature of sub-layer water phantom under layers of water and glass [36].

processed, and transmitted through a wireless unit. A micro-controller unit (MCU) controls the radiometer switches enabling phase-sensitive detection of the very low human black-body power

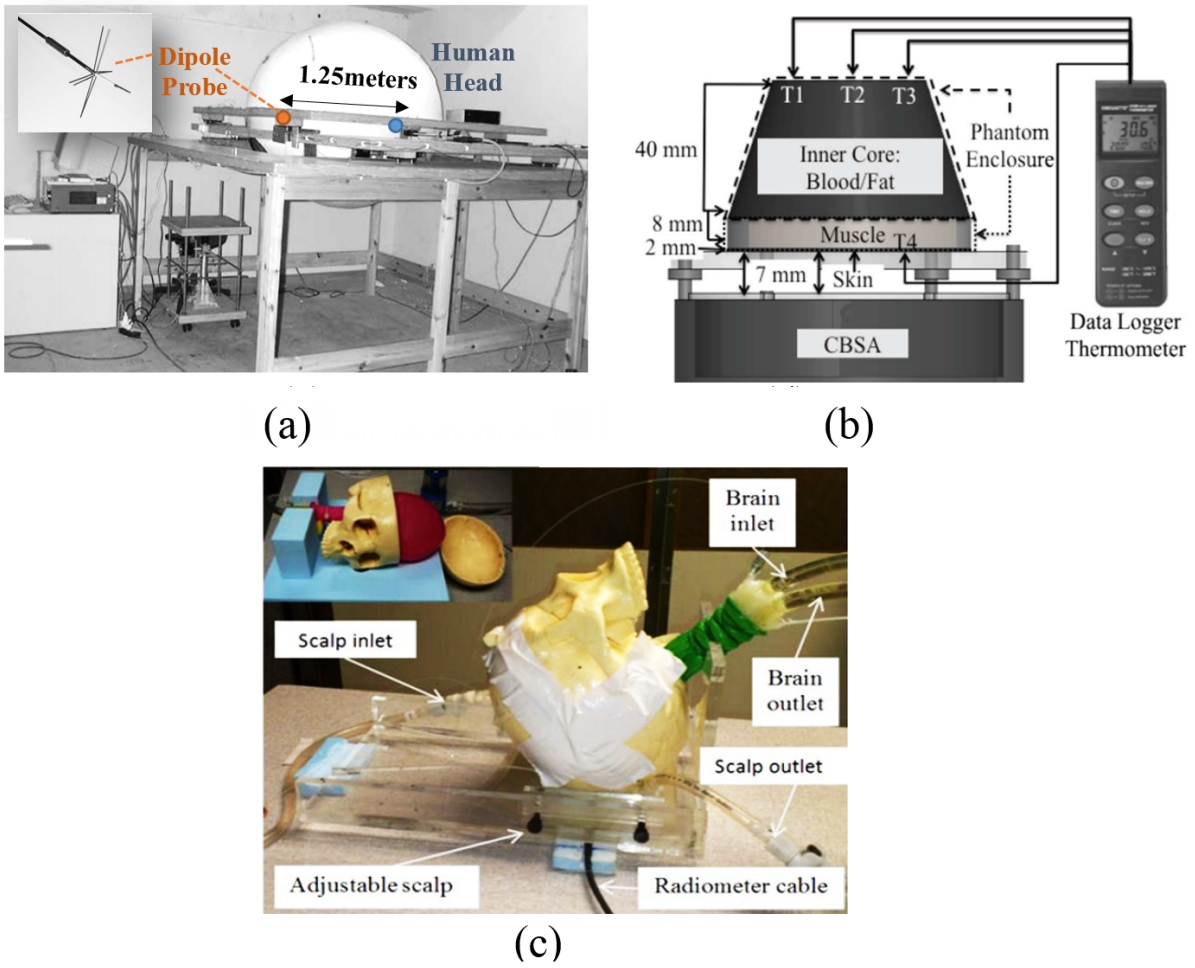

Figure 1.5: Review of some of previous works in single-frequency microwave thermometry. (a) A 200 MHz bandwidth radiometer and an isotropic-dipole are used at 3.5 GHz for detecting conductivity of head phantom inside a 1.5 m ellipsoidal conductive-wall cavity [29], (b) A 400 MHz bandwidth radiometer is used at 1.4ĠHz to detect temperature of blood under skin and muscle. Probe size is 9 cm ×2.7 cm [25], (c) A 500 MHz bandwidth radiometer is used at 1.35 GHz for detecting brain temperature under skull and scalp. The probe is a log-spiral 2.5 cm ×1.5 cm [34].

levels.

1.5 Challenges

The challenges associated with designing a manufacturable and cost-effective wearable wireless radiometer can be categorzied to several main regions.

- The first challenge in designing a microwave thermometer is to detect the very low level of

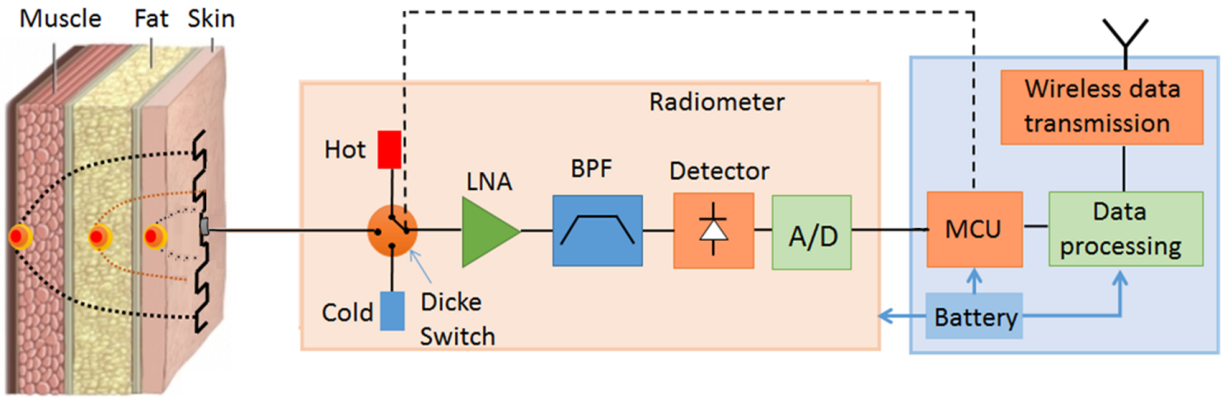

Figure 1.6: Block diagram of internal body temperature measurement system. The power received from tissue layers by the narrowband probe is coupled to the Dicke radiometer circuits, which consist of a switch that is required for calibration, a low-noise amplifier (LNA) followed by band-pass filters, and a diode detector circuit. The hot and cold loads are used for continuous temperature calibration of the radiometer. The detector output is a DC voltage which can be integrated over time to increase the signal-to-noise ratio (SNR). This output is digitized, processed, and transmitted through a wireless unit. A micro-controller unit (MCU) controls the radiometer switche enabling detection of small gain fluctuations in the system.

black-body noise power emitted by the human body. To measure internal tissue temperature at centimeter-depth under the skin, lower microwave frequencies are used, forcing operation on the tail of the black-body curve. At 1.4-1.427 GHz, the human body radiates about -100dBm of thermal noise power.

- An additional problem is the high amount of power loss in the tissue layers. This problem originates from high conductivity of skin and muscle as well as high dielectric contrast between skin, fat, and muscle layers.

- Another challenge is associated with susceptibility to interference due to the very low levels of power emitted by the tissues. This can be mitigated by multiple stages of filtering in the probe and circuit design, by miniaturization of the probe and circuits, by shielding the radiometer, and also by signal processing techniques.

- The power variation at the input of the radiometer due to a 0.1 degree of temperature change is less than 0.01dB. This enforces a a highly sensitive radiometer design which translates to

very high required system gain, which can result in instabilities.

- Maintaining small size and low power consumption are also important in designing a wearable radiometer.

- In addition to challenges in designing the probe and radiometer, retrieving the temperature of a buried tissue layer requires solving an inverse problem. This requires the knowledge of near-field power transfer, and electromagnetic and geometric properties of the tissue, as well as an efficient estimation method. Given that each human is different and the electric properties of tissues vary, the model calibration is a challenge.

- Finally, in many applications relative temperature measurements or monitoring over time are sufficient, while in other cases absolute temperature is required. This is a more difficult measurement and would most likely require an independent known temperature source for additional calibration during measurements.

1.6 Tissue properties and phantom development

Knowledge of the dielectric properties is essential for design of the probe, frequency selection, and inversion of the radiometric observations to determine the physical temperature of the tissue. The dielectric properties of tissues have been widely studied, and the standard resource is a series of articles from S. Gabriel and C. Gabriel that include a literature survey, measurements, and models for various human tissues [38], [39], [40]. For the designer, there are several resources where these tissue properties are available. For dielectric properties of various tissues in the frequency range of 10 Hz to 100 GHz, an Internet resource for the calculation of the dielectric properties of body tissues, based on S. Gabriel and C. Gabriel data, is available from the Italian National Research Council [41]. Additionally, the "Tissue Properties Database" from the IT'IS Foundation has not only the dielectric properties of the tissues, but also physical properties such as density and thermal conductivity. IT'IS also has a virtual population of body models [42] that can be used to estimate tissue thicknesses for different people to account for inter subject variability. Although the

temperature dependence and detailed frequency dependence of tissue parameters are important for design, here it will suffice to point out that the dielectric constant at 1 GHz varies from 5.5 (fat) to 55 (muscle), while the conductivity varies from 0.05S/m to 0.98S/m, respectively. Knowledge of the dielectric properties is essential for design of the probe, frequency selection, and inversion of the radiometric observations to determine the physical temperature of the tissues.

Figure 1.7: Top figure: Skin and muscle tissue phantoms are developed based on the recipe presented at [43]. Agar tissue phantom is also developed in the lab based on the recipe presented at [44] (Appendix A). These tissue phantoms can melt during some of the measurements. As a backup smoked salmon and chicken breast are used as the skin and muscle tissue phantoms at 1.4 GHz.

In research for medical applications, chicken breast is often used to mimic dielectric properties similar to those of human muscle [45]. However, chicken breast can spoil after few days. Smoked salmon, is an alternative used for some of the measurements which will be presented in following chapters. Skin and muscle solid tissue phantoms are developed based on the recipes presented at [43]. These tissue phantoms mimic the electromagnetic properties of the real tissues at microwave frequencies. Agar solid tissue phantom (representing skin and muscle) is also developed in the lab based on the recipe presented in [44]. Preparation of Agar tissue phantom in [44] is easier than skin and muscle tissue phantoms in [43] and is given in the Appendix A for the sake of completeness.

In some of the measurements presented in Chapter 5, solid tissue phantoms are replaced by

saltwater, the temperature of which is easily controlled in the laboratory (without the melting issue of the solid tissue phantom). Adding salt to water increases the electromagnetic loss of the water which in turn makes it closer to the conductivity of skin and muscle [46], for example, salinity of 9 parts-per-thousand (ppt) corresponds to conductivity of 1.545 S/m.

Table 1.1 summarizes the electrical properties of skin, fat, and muscle at 1.4 GHz along with developed skin, muscle, and Agar tissue phantoms.

Table 1.1: Tissue and phantom electromagnetic properties at 1.4 GHz [41], [47], [42], [48], and [45]. Tissue phantoms developed in the lab based on the recipes presented at [43], [46], and [44]. *Agar recepie is provided in Appendix A.

Tissue	Permittivity	$tan\delta$	σ (S/m)
Skin	39.661	0.335	1.036
Fat (Infiltrated)	5.395	0.154	0.065
Fat (Non infiltrated)	11.2	0.172	0.15
Muscle	54.112	0.270	1.142
Skin phantom	42.920	0.404	1.350
Muscle phantom	52.791	0.389	1.600
Agar*	76.000	0.390	1.540
Chicken breast	39.661	0.335	1.036
Smoked salmon	52.500	0.370	1.510
FR4	4.400	0.020	0.001
Rohacell	1.050	0.000	0.000
Rogers 6010	10.200	0.002	0.002
Water	78.000	0.058	0.350
Salt water (Salinity=9ppt)	78.000	0.260	1.545

1.7 Operating frequency

The first step in designing the microwave thermometer is to choose an operating frequency. The penetration depth in the skin for a plane wave at IR is about 2 mm. At microwave frequencies, electromagnetic waves penetrate through the body tissues as much as a few centimeters, enabling the radiometer to track deep tissue temperature variations. Working at microwave frequencies, however, limits the received thermal noise power to the tail of the black-body radiation curve. At human body temperature (310K), and radiometer bandwidth of 27 MHz, (1.8) predicts $P \ -100\,dBm$ of

incident power at the antenna surface. In this work the "quiet" frequency band of 1.4-1.427 GHz, allocated for radio astronomy, is selected. This frequency band provides a reasonable compromise between sensing depth and RF interference. At higher microwave frequencies, the penetration depth reduces to a few millimeters, while at frequencies below 1 GHz, the spatial resolution associated with finite probe size is reduced [24].

1.8 Summary

In this introductory chapter, microwave radiometery applications, existing core-body thermometers, and available microwave thermometers are overviewed. The disadvantages and advantages of previously demonstrated methods are presented as a motivation to the research of this thesis. Various solid and liquid tissue phantoms are discussed, since they are required for design and experimental validation. This chapter also reviews basic theory of black-body radiation as a foundation for microwave thermometry and introduces the challenges related to the design of a microwave thermometer, including frequency choice and sensitivity. The final device operating frequency range of 1.4-1.427 GHz is chosen since it is a quiet band allocated to radio astronomy and is less susceptible to radio frequency interference, while providing a few centimeters of sensing depth in tissues.

1.9 Thesis goal and outline

With current trends to personalize medicine with wearable wireless sensors, there is a need for continuous temperature monitoring devices placed on different parts of the body. The goals of microwave thermometry are non-invasive, fast, wearable, cheap, and passive temperature measurement, which operating at a sufficiently low frequency for several centimeter penetration into tissues [49]. This thesis demonstrates the feasibility of designing a system for tracking the internal body temperature. Challenges include understanding black-body radiation in the near field, efficient probe design that includes tissue properties and variation of tissue layers across the body, compact sensitive stable radiometer design, estimating internal temperature from total power external

measurements, and RFI mitigation.

Chapter 2 discusses reciprocity between absorption and emission in the near field, showing that simulating volume power loss density in the body due to a transmitting probe on the skin can predict the emitted power from the volume received by the same probe. Tissue temperature retrieval using weighting functions for each tissue layer that enables calibration of the instrument, is also presented in this chapter.

Chapter 3 describes the design method, implementation and validation of different near-field antenna probes, that can be used in a wearable thermometer.

Chapter 4 discusses radiometer architectures and three different radiometers are characterized. Design method and practical considerations in designing a stable radiometer are also detailed in this chapter.

Chapter 5 presents measurements on single-layer, and two and three-layer phantoms, and these are compared to thermocouple measurements [50], and [51] to validate the approach. This chapter also discusses errors due to RFI [52]. Measurements on a human cheek are also compared to internal and external thermocouple data, showing that the black-body radiation is instantaneous and that the thermal conduction does not contribute to measurements performed on a fast scale [53], [54], and [55].

Chapter 6 In the final chapter, the contributions of this work and directions for future research are presented.

Chapter 2

Temperature Retrieval

Contents

As mentioned in the first chapter, the microwave thermometer relies on black body radiation from buried tissue layers, which results in a measurement of total radiated heat power. Following efficient reception of this power, an inverse problem needs to be solved in order to estimate the temperature of a buried tissue layer. This chapter discusses the physical principles of near-field radiative heat transfer as well as temperature estimation based on radiometric measurements, specifically as they apply to internal temperature measurements. Radiative heat transfer is commonly discussed in the far field, especially in the context of low-noise receiving antenna systems such as in radioastronomy, e.g. [56]. However, it can be extended to the near field as is relevant to the thermometry application, as discussed in the next section of this chapter. Retrieving the temperature from the total measured power is an inverse problem, also solved for the near field.

2.1 Reciprocity

Reciprocity between emission and absorption is well known in the case of far-field radiation [56]. For a black body, the radiated and absorbed power are equal. In what follows, reciprocity

between absorption and emission in the near field is discussed, showing that simulating volume power loss density in the body due to a transmitting probe on the skin can predict the emitted power from the volume received by the same probe. This conclusion is shown later in the thesis to be fully supported by a large number of different measurements.

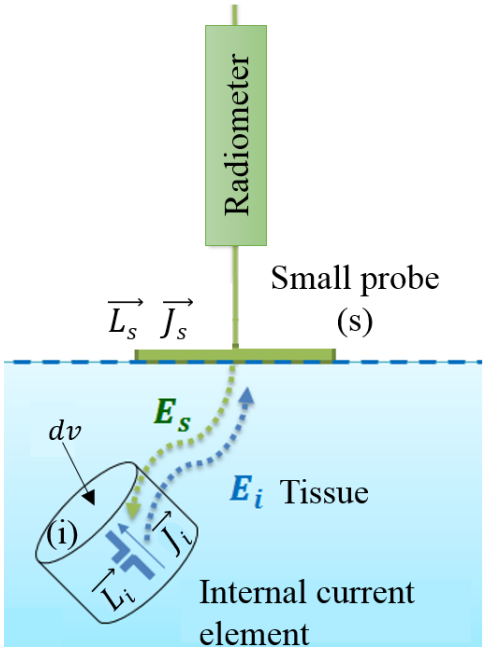

Figure 2.1: A small probe (s) is placed on top of the tissue and a small current element (i) in the tissue. Two sets of sources $\overrightarrow{J_s}$ and $\overrightarrow{J_i}$ are radiating inside the tissue at the same frequency and producing electric fields of $\overrightarrow{E_s}$ and $\overrightarrow{E_i}$, respectively. The length of both radiators, $\overrightarrow{L_i}$ and $\overrightarrow{L_s}$, are short, forcing a uniform electric field on the probes.

As shown in Figure 2.1, assume that a small probe (blackbody radiated from a volume element of the body) (s) is placed on top of the tissue and an infinitesimally small radiator (i) is embedded in the tissue. Two sets of sources $\overrightarrow{J_s}$ and $\overrightarrow{J_i}$, produce electric fields $\overrightarrow{E_s}$ and $\overrightarrow{E_i}$, respectively.

Since the medium is linear, but not necessarily homogeneous, the Lorentz reciprocity theorem can be written as

$$\iiint_V (\overrightarrow{E_i}.\overrightarrow{J_s} - \overrightarrow{E_s}.\overrightarrow{J_i})dV = 0 \tag{2.1}$$

Assuming that the $\overrightarrow{L_i}$ and $\overrightarrow{L_s}$ are very short, the electric field is uniform across them and the

induced voltage on open circuit terminals of each radiator is

$$V_{oci} = \overrightarrow{E_s}.\overrightarrow{L_i} \tag{2.2}$$

$$V_{ocs} = \overrightarrow{E_i}.\overrightarrow{L_s} \tag{2.3}$$

Note that for simplicity we are considering only one component of a current source that could in principle be volumetric and contain all components. The analysis presented here is meant to be simplified and to give a physical intuition, rather than a strict proof. It is already known that absorption and radiation are reciprocal, but this is usually discussed in the far-field context. Here, it suffices to present a simple case that shows intuitively that reciprocity also holds in the near field, as expected. Under this simplification, we can find the current on each radiator as the surface integral of the current density over the surface

$$I_i = \iint_s \overrightarrow{J_i}.d\vec{s} \tag{2.4}$$

$$I_s = \iint_s \overrightarrow{J_s}.d\vec{s} \tag{2.5}$$

Comparing (2.2) - (2.5) with (2.1) yields the reciprocity theorem applied to our case

$$V_{oci}I_i = V_{ocs}I_s \tag{2.6}$$

First, assume the small probe radiates, Figure 2.2-a. The equivalent network of the internal current element in receiving mode is given in Figure 2.2-b. The impedance of the the internal current element Z_i is assumed to be the conjugate of the impedance of its tissue load ($Z_i = R_i - jX_i$). This assumption is made for convenience.

The power delivered by the small probe to the internal probe is equal to

$$P_i = \frac{1}{2}Re(Z_i(II^*)) = \frac{|V_{oci}|^2}{8R_i} \tag{2.7}$$

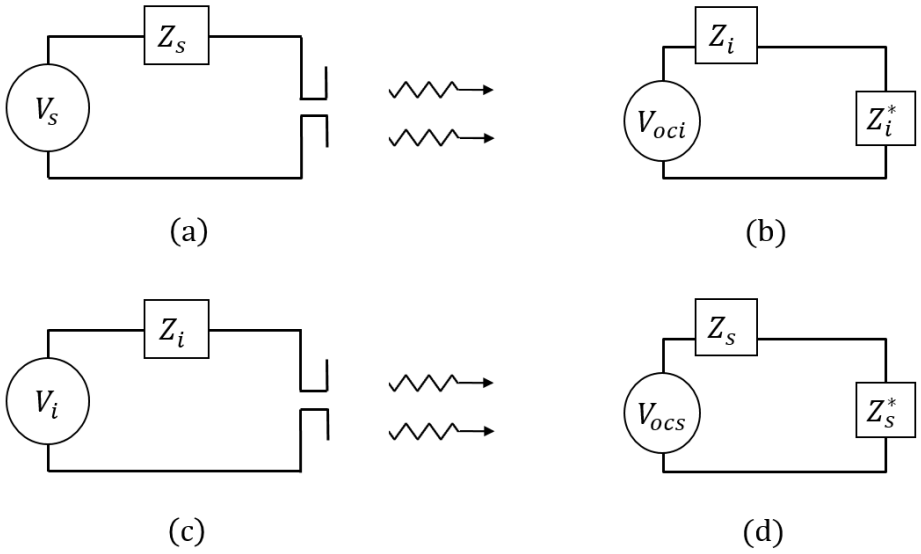

Figure 2.2: (a) the equivalent network of small probe in transmitting mode and (b) the internal current element in receiving mode. The impedance of the the internal current element Z_i is assumed to be conjugate of the impedance of the load. (c) the equivalent network of internal current element in transmitting mode and (d) the small probe in the receiving mode. The internal impedance of the the main probe Z_s is assumed to be the conjugate of the impedance of its load.

The power absorbed in the internal current element is equal to

$$\Delta P_i = \sigma_i |\overrightarrow{E_s}|^2 \Delta v \tag{2.8}$$

where σ_i is the conductivity of the tissue. By substituting (2.2) and (2.8) into (2.7), the internal resistance of the current element becomes

$$R_i = \frac{|L_i|^2}{4\sigma_i \Delta v} \tag{2.9}$$

Next, assume the internal current element emits black-body thermal noise, Figure 2.2-c. As shown in Figure2.3 (a-b), the power delivered by a current element placed inside a closed enclosure at temperature T in thermal equilibrium is equal to the power delivered by a resistor maintained at the same temperature (assuming each is connected to a matched receiver of bandwidth B) [57]. The thermal noise power can be modeled by an equivalent Thevenin circuit consisting of a noise voltage and a noise less resistor (R_i), as shown in Figure 2.3-c. If the load impedance is 0 Ω, no

power is transferred to it since the voltage is zero. If the load has infinite input impedance, again no power is transferred to it since there is no current. Maximum power transfer occurs when the source and load impedance are equal. Thus, the black-body thermal noise radiator can be modeled by a voltage source with an impedance matched to the internal impedance of the voltage source. Under this circumstances, the rms noise voltage at maximum power transfer is:

$$V_i = \sqrt{4kT_iR_iB} \tag{2.10}$$

where k is Boltzmann's constant, T_i is the temperature of tissue, and B is the bandwidth of the radiometer. The noise current is

$$I_i = \sqrt{4kT_iB/R_i} \tag{2.11}$$

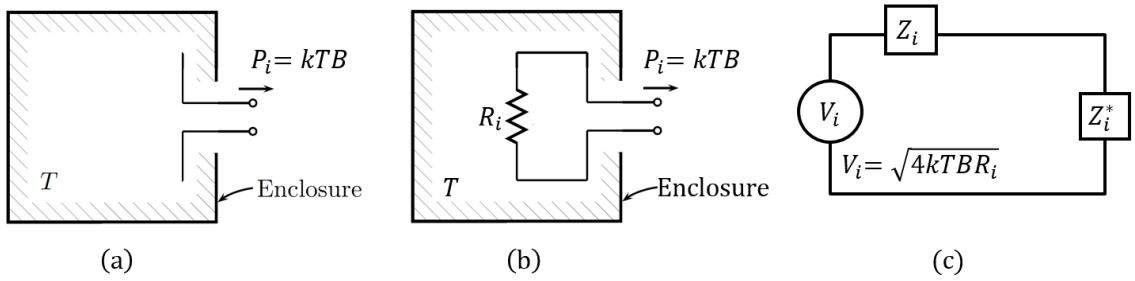

Figure 2.3: (a) the power delivered by a current element placed inside a closed system at thermal equilibrium enclosure of temperature T (b) this power is equal to the power delivered by a resistor maintained at the same temperature (assuming each is connected to a matched receiver of bandwidth B) [57], (c) the equivalent voltage model of black-body radiator. The internal current element impedance Z_i is assumed to be the complex conjucate of its load impedance.

From 2.6, the open circuit voltage at the terminals of the small probe can be found as

$$V_{ocs} = V_{oci}I_i/I_s \tag{2.12}$$

Substituting (2.2) and (2.11) into (2.12) yields

$$V_{ocs} = (\overrightarrow{E_s}.\overrightarrow{L_i}/I_s)(\sqrt{4kT_iB/R_i}) \tag{2.13}$$

In a similar manner, using the equivalent circuit model of small probe in receiving mode, as illustrated in Figure 2.2 (c-d), the power delivered by the internal current element to the small probe is

$$\Delta P_s = \frac{|V_{ocs}|^2}{8R_s} \tag{2.14}$$

Substituting (2.9) and (2.13) into (2.14) yields

$$\Delta P_s = 2\sigma_i \frac{kT_iB}{R_sI_s^2} \left|\overrightarrow{E_s}\right|^2 \Delta v \tag{2.15}$$

Since the blackbody radiation has no polarization in nature, and the receiving probe is polarized, only half of the power can be received by the small probe [21]. So, a factor of 0.5 should be included in (2.15).

Equation (2.6) can be written in the form of $R_iI_i^2 = R_sI_s^2$. Therefore,

$$R_s = R_iI_i^2/I_s^2 = 2P_{in}/I_s^2 = 2kT_iB/I_s^2 \tag{2.16}$$

Substituting (2.16) in (2.15) shows that

$$\Delta P_s = \frac{1}{2}\sigma_i|\overrightarrow{E_s}|^2\Delta v \tag{2.17}$$

In summary, it was shown that by reciprocity, the thermal noise power delivered by a tissue at non-zero temperature to a near-field small probe, is directly proportional to the absorbed power by the same tissue volume delivered by the same probe in transmitting mode.

This equation is the point form is the Joule's law and directly proportional to the definition of the volume loss density (VLD). This parameter can be obtained by full-wave near-field electromagnetic simulations with finite difference time domain (e.g. Sim4Life) or finite element method (e.g. HFSS) and it is defined as

$$P_v = \frac{1}{2}Re(\bar{E}.\bar{J}^* + j\omega\mu\bar{H}.\bar{H}^*) \tag{2.18}$$

where E is the electric field, $\bar{J}$ is the conjugate of the volumetric current density, B is the magnetic flux density, and $\bar{H}$ is the conjugate of the magnetic field.

In the future chapters, volume loss density pattern will be used to compare the sensing region of different probes.

2.2 Temperature retrieval methods

Once the power is measured by a radiometer, a model is needed for the tissue stack-up to determine the temperature distribution. Based on the application, different methods can be applied.

- To find temperature distribution, one method is finding the spatial Green's function of randomly fluctuating current sources (Jr). As it mentioned earlier, in this method stochastic Maxwell's equations should be solved for layered media. In [29], the spatial Green's function is solved for a simple isotropic dipole located in a cavity and a comprehensive spatial temperature profile of head model is presented. This method can not be easily extended to complex non-homogeneous media in direct contact with a complex probe.

- Another method applies multi-frequency radiometry to find the temperature profile of different tissue layers [23] and [12]. This method requires multiple radiometers which in turn increases the size, power consumption, cost, and complexity of the system. This method becomes less accurate when the weighting function of a deep tissue layer is dispersive. Also, data analysis is not trivial as it becomes sensitive to many unknown parameters [23]. The theory of two-frequency near-field microwave probing of planar-stratified media with measurements of water/glass/water phantom is investigated in [36]. Quiet frequencies of 1.4 and 2.7 GHz are chosen.

- Modeling the temperature profile with the bio-heat transfer equation has also been proposed in [58]. Combining the knowledge of multi-layer radiometry and the bio-heat equation can provide a spatial temperature profile [23]. This method can improve the accuracy and stability of the retrieved spatial temperature [35], however, information about heat rate,

heat exchange, blood perfusion, and heat generation are not easy to obtain for different people, under different activities.

The goal of the research in this thesis is not imaging - rather than being interested in the spatial temperature profile, the important quantity for the applications listed in the introduction is tracking of relative internal temperature. Therefore, the temperature of skin and fat layers are not of interest. The only unknown is the mean temperature of the muscle (core) layer which can be found by a single frequency measurement.

Typically, the single frequency estimation has been done with near-field weighting functions estimated from loss simulation [34]. A standard parameter used to describe power that penetrates into the body is the Specific Absorption Rate (SAR), expressed in W/kg. It will be shown that from reciprocity, absorption is reciprocal to black-body emission, so the knowledge of power loss in the tissue gives indirectly the black body effective temperature, provided the electrical properties of the tissues are well known.

2.3 Radiometer buried layer thermometer calibration

Thermometer calibration consists of instrument calibration and model calibration. Instrument calibration corrects the gain fluctuation of the radiometer, as it will be explained in Chapter 4. Model calibration, however, refers to near-field EM analysis, as well as reflection, loss, and mismatch in the system and will be explained in this section.

Figure 2.4 shows the setup of a radiometer placed on Layer 1 (skin), with other tissue layers (e.g. fat, muscle, etc.) denoted by Layer 2, Layer 3, etc. The radiometer receives radiation through the probe which is at a physical temperature T_p. The total power received from the tissue stack corresponds to a probe radiometric temperature $T = P/kB$.

Therefore, the equivalent thermal noise temperature of a tissue stack, each tissue layer at different temperature, is the temperature contribution of each layer weighted by a factor W_i as

$$T = \sum_i W_i(f, d, T, f_n, \sigma) T_i \tag{2.19}$$

where T_i is the physical temperature of the i-th layer and $W_i(f)$ is the i-th layer weighting function, which depends on frequency, thickness(d), conductivity(σ), and the near-field pattern of the probe (f_n).

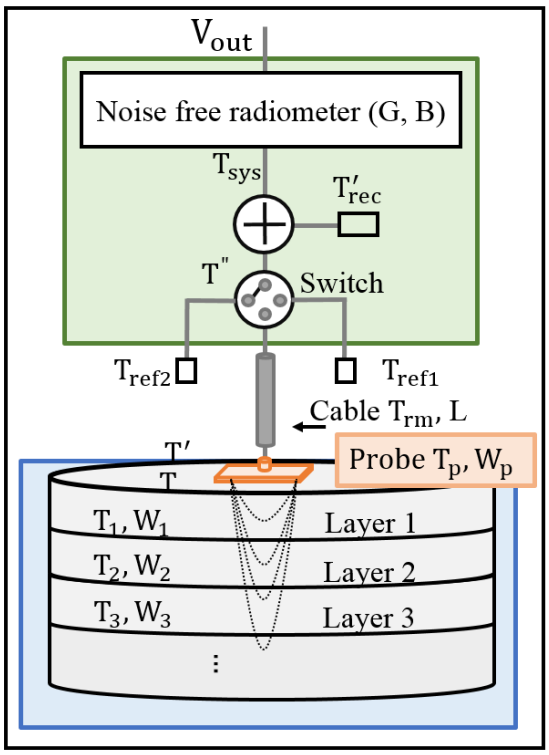

Figure 2.4: Diagram of the setup for estimating temperature of a buried tissue layer. A near-field antenna probe at a physical temperature T_p is placed on the skin surface on top of various tissue layers (1,2,3,...) at physical temperatures $(T_1, T_2, T_3, ...)$. The Dicke radiometer measures the total radiometric power. The weighting functions of each layer $(W_1, W_2, W_3...)$ are used in the estimation of each layer temperature. The radiometer receives radiation through the probe which is at a physical temperature T_p.

In order to estimate the deep tissue layer temperature, the first step is to express the radiometric temperature of the probe at the feed point (T) in terms of the temperatures of all relevant tissue layers as given in Eq. (2.19) which for the three considered layers becomes:

$$T = T_1 W_1 + T_2 W_2 + T_3 W_3 \tag{2.20}$$

where T_i is the temperature of the i-th layer and $W_i(f)$ is the i-th layer weighting function, which depends on frequency, thickness, physical temperature and conductivity of the material as well as near-field probe pattern.

Weighting function of each layer can be expressed as the power dissipated in a particular layer normalized to the total dissipated power

$$W_i = \frac{P_{d,i}}{\sum P_d} \tag{2.21}$$

where P_{di} is the power dissipated in the i-th layer and P_d is the total dissipated power in the volume. The volume used for calculating the weights is bound by power loss density values below $10\,\mathrm{W/m^3}$. This is a good approximation since a very small amount of power (50dB less than the maximum power) is absorbed by the remaining volume.

With these assumptions, the radiometer temperature is first corrected due to reflection as

$$T' = \eta_L T + (1 - \eta_L) T_p \tag{2.22}$$

where η_L is the efficiency of the probe which accounts for the impedance mismatch, conduction loss, dielectric loss as well as radiation efficiency. T_p is the physical temperature of the probe. The radiometer temperature is next corrected for the loss in the cable:

Next, antenna temperature is corrected due to the loss in the cable as

$$T'' = LT' + (L - 1) T_{rm} \tag{2.23}$$

where T_{rm} is the physical temperature of the cable, and L is the loss in the cable ($L_{dB} = 10 log L$). The cable loss of the reference noise sources should also be calibrated in the same manner. This procedure corrects the radiometric observations up to the plane of the radiometer (shown with dashed-line in Figure 4.3). The radiometer also needs to be calibrated for gain fluctuations, which is performed every 20 seconds ($\tau = 20\,\mathrm{s}$). Therefore, the overall system temperature is given by

$$T = \begin{cases} T'' + T'_{rec} & \text{if } 0<\text{t}<1/3 \text{ sec}, \\ T_{ref1} + T'_{rec} & \text{if } 1/3<\text{t}<2/3 \text{ sec}, \\ T_{ref2} + T'_{rec} & \text{if } 2/3<\text{t}<1 \text{ sec}. \end{cases} \tag{2.24}$$

where T'_{rec} is the receiver temperature and $T_{ref1,2}$ are the noise source temperatures. For a diode detector sensitivity of C_d, and noise-source and probe bandwidths $B_{ref1,2}, B_{probe}$, the total radiometric temperature becomes

$$T_{sys} = \begin{cases} C_d G k B_{probe}(T'' + T'_{rec}) & \text{if } 0<\text{t}<1/3 \text{ sec}, \\ C_d G k B_{ref1}(T_{ref1} + T'_{rec}) & \text{if } 1/3<\text{t}<2/3 \text{ sec}, \\ C_d G k B_{ref2}(T_{ref2} + T'_{rec}) & \text{if } 2/3<\text{t}<1 \text{ sec}. \end{cases} \tag{2.25}$$

in which, the the sensitivity of diode detector is shown with C_d.

For some phantom measurements, due to loading of the probe, the bandwidth of the probe is narrower than that of the hot and cold noise sources, which follow the bandwidth of the radiometer. To take into account the bandwidth mismatch, a new calibration constant, b, is added to the calibration. This constant can be estimated by finding the operating bandwidth of the probe and that of the radiometer from:

$$B_{ref1} = B_{ref2} = b \times B_{probe} \tag{2.26}$$

Therefore, by direct thermocouple temperature measurements of the probe and surface tissue layer (skin), the unknown core tissue layer temperature can be estimated. In addition to the two independently measured temperatures, other inputs needed for estimation are the loss of the cable, the noise figure of the radiometer, the efficiency of the probe, and the weighting functions obtained from full-wave simulations.

2.4 Summary

This chapter discusses the the interaction of human tissue layers with a probe and calibration procedure for a microwave thermometer. A background on temperature retrieval methods from the literature is presented. Reciprocity between radiated and absorbed thermal noise power density in the near-field tissue layers is discussed and proven for a simple case. The measured radiometer temperature is formulated as the summation of contribution of each tissue layer times their physical temperature, and the required device calibration shown to be a function of the efficiency of the probe, cable loss, gain fluctuations of the radiometer device and probe bandwidth. Contributions related to this chapter are included in [53] and [54].

Chapter 3

Near-field antenna probe

Contents

3.1 Introduction

In microwave thermometery, the probe receives thermal power radiated by the tissue. However, standard antenna design and analysis is not directly applicable, since the probe is in the near field of the tissues. Receiving very low levels of black-body noise power, on the order of -110 dBm, from buried tissue layers is challenging. As shown in Fig. 2.21, tissue layers have high dielectric-

constant contrast and typically the skin dominates the received power due to its high conductivity, making it difficult to receive power from deeper layers, e.g., the muscle layer.

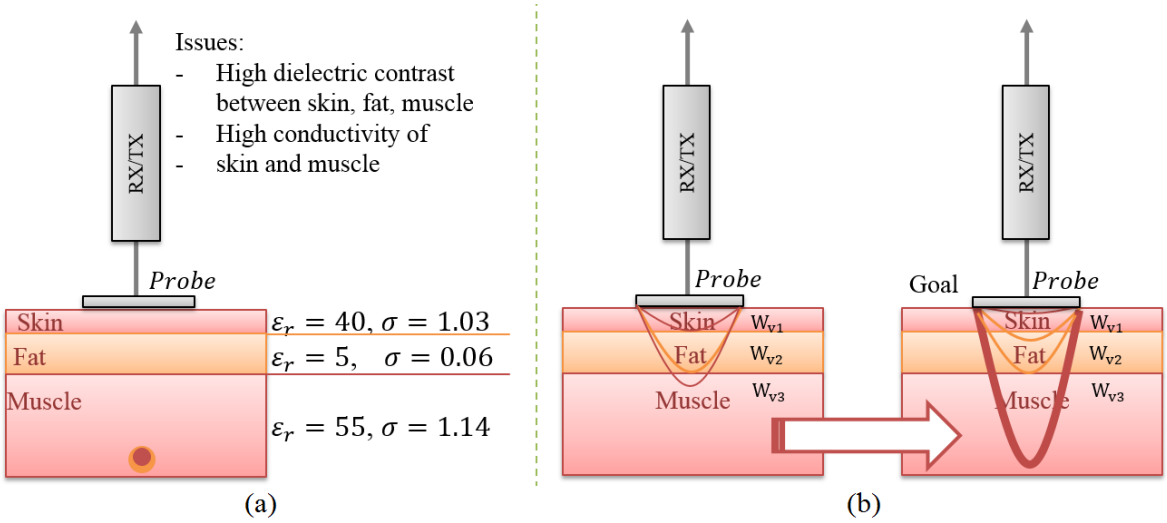

Figure 3.1: (a) A near-field probe positioned on the stack of skin-fat-muscle. High dielectric contrast between tissue layers and high conductivity of skin and muscle layers result in attenuation in tissue layers. (b) the probe needs to be engineered to receive a large portion of power from the muscle layer while minimizing the reception from the skin and fat layers. Electromagnetic properties of the tissues are given at 1.4 GHz [42].

Some of the previous probes used for human body thermometry – listed in Table 3.1 – include waveguide probes [23], [28], cavity-backed slots [25], ring slots [59], folded dipoles [49] and cavity-back log-spirals [37]. Some of these probes are not optimized for power reception from a specific tissue layer, or do not take high dielectric-constant contrast between tissue layers into account. Most are also wideband in order to collect more power, but that makes them more susceptible to RFI. A probe which receives thermal power from deeper tissue layers, while minimizing the effect of surface tissues is desirable. In this work, the developed system is intended for long-term temperature monitoring and therefore the architecture is chosen towards implementing a wearable device. Therefore, the skin-mounted probe needs to be small, and receive most of the power from the tissue stack and as little as possible external power (RFI).

This chapter presents an overview of several near-field probes operating at 1.4 GHz. The goal is to present design, implementation and validation of the probes that can maximize black-body

Table 3.1: Example probe for microwave thermometry from literature.

No.	Freq. (GHz)	Architecture	Dimensions (cm)	Near-field loading for	Ref.
1	1-2 GHz	Ring slot	5.20×5.20×1.52	Agar-based muscle phantom	[59]
2	1.2-1.6 GHz	Cavity backed slot	9.00×9.00×2.70	Skin/muscle/fat-blood phantom	[25]
3	3.5 GHz	Cavity backed elliptical patch	5.00×5.00×3.20	Human arm	[60]
4	0.9-1.8 GHz	Folded dipole	3.70×3.00×4.20	Water/glass/water	[36]
5	2.52 GHz	L-notch patch	4.00×4.00×1.27	Water phantom	[61]
6	1.15 GHz	Circular waveguide	6.70×4.40×4.40	Human breast	[28]
7	3.5 GHz	Isotropic dipole	2.50×1.50	Skull/brain phantom	[29]
8	1.35 GHz	Cavity log spiral	2.50×1.50	Scalp/skull/brain phantom	[37]
9	1-3.8 GHz	Dielectric filled waveguide	2.10×2.80	Water phantom	[62]
10	1-3.5 GHz	Archimedean spiral	3.50×3.50	Water phantom	[63]

reception from deep tissue layers. The design approach presented here can be applied to different tissue stacks for a range of applications, e.g. power transfer to embedded tissue implants, and RF heating of deep tissue layers for burning fat or wrinkle reduction with reduced surface skin layer damage [64].

3.2 Probe design

As explained in the previous chapter, analysis of a near-field antenna probe can be done in the reciprocal case by analyzing a probe in transmitting and calculating the amount of absorbed power in the tissue. This is typically quantified by the volume power loss density (VPLD), which is a measure of the volume Joule loss density, $p_J = \sigma E^2 = \rho J^2$ (in W/m^3). In this chapter, full-wave electromagnetic simulation tools such as HFSS from Ansys or Sim4Life are used to determine the probe sensing pattern and during the design process, volume loss density was simulated at all points in the tissue stack to maximize the absorbed power density in the buried muscle layer.

The human body can be treated as layered media of different electromagnetic properties

(Figure 3.1). In our work, the probe is placed on a stack of skin, fat, and muscle layers. By considering the boundary conditions for the electric field vector and high dielectric-constant contrast between the skin, fat, and muscle layers, it is shown that the desired component of the electric field vector produced by a near-field body-worn probe is the one tangential to the skin surface, since E_{tang} is continuous across the interface of tissue layers. Therefore, good probe candidates are patch and slot antennas, which can be designed to have dominant E_{tang} and can be made flexible and conformal to the skin.

The probes described in this chapter include: (a) a circular patch; (b) a patch with a superstrate for field focusing; (c) a circular patch with superstrate and shorting-pin for size reduction; (d) an array of shorted-pin superstrate patch probes; (e) a ring-slot probe with a superstrate; (f) a flower-shaped slot probe with a superstrate for increasing effective radiating area; and (g) a microstrip-fed cross slot probe. Probes (b-d) are fabricated and measurement data is presented. Probe (d) increases the power reception from the muscle compare to other designs. Probes (e-f) are shown to behave as an array of 3 dipoles, while probe (g) acts as a 4-elements radiator. All probes are designed on high dielectric constant substrates (Rogers 6010) with $\epsilon_r = 10.2$ for size reduction. Probe (b-d) are fabricated and validated experimentally. A comparison is given with respect to received power from the muscle layer, impedance matching, size, and bandwidth.

3.2.1 Circular patch

A coaxially-fed circular patch fabricated on a Rogers 6010 1.58-mm thick substrate (ϵ_r=10.2) is designed (Figure 3.2) for size and simplicity. The inherent narrow bandwidth of a patch is also beneficial for RFI mitigation since there are a number of cellular bands in the neighborhood of the quiet 1.4-GHz band. The ground plane has two functions: to help shielding from RFI and to provide an RF ground for both the probe and radiometer. The circular patch probe is designed specifically for a tissue stack of skin, fat and muscle and is optimized with HFSS using tissue models listed in Table 1.1. The first layer is Agar skin-phantom (2 mm thick), the second layer is an FR4 fat phantom (5 mm) and the third layer is assumed to be an Agar muscle phantom much thicker

than the penetration depth at 1.4 GHz. The skin exhibits high relative permittivity which in turn reduces the size of the probe.

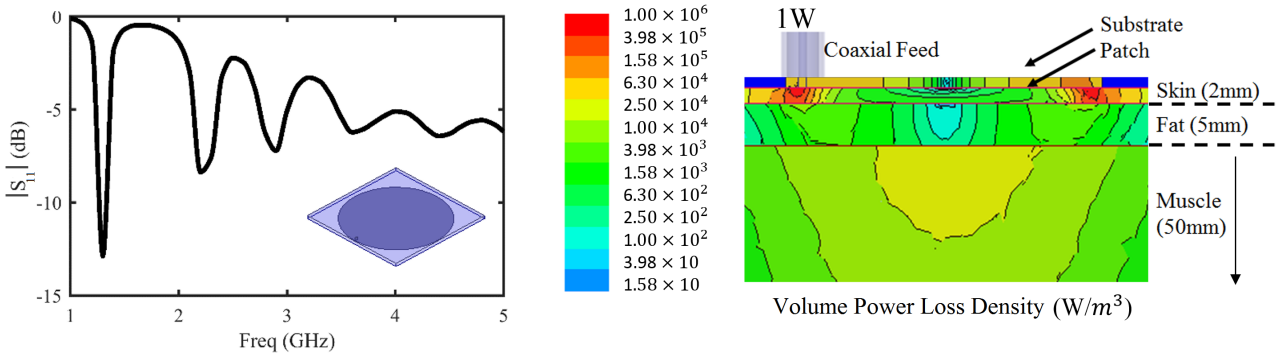

Figure 3.2: (a): Simulated circular patch probe reflection coefficient when placed on a stack of skin-fat-muscle. (b): Simulated volume power loss density of the circular patch probe placed on the body model when the probe is fed with a $1W$ matched source.

According to Figure 3.2, when the patch is placed on the tissue stack and fed with a 1 W matched source in a full-wave simulation (HFSS), the resulting volume power loss power density in the cross-section at the center under the probe shows that 33% of the total power is absorbed in the muscle layer, while the skin layer absorbs 50% of the power. It can be seen that a large fraction of the power is absorbed in the fat layer, although it has the lowest loss. This is due to the large mis-match in the real part of the permittivity between fat and the neighboring skin and muscle (refer to Figure 3.1).

3.2.2 Circular patch with superstrate

The simplified layered model of a part of human body is shown in Figure 3.1. According to boundary conditions, the tangential component of electric field is continuous at the boundary between tissue layers while the normal component is inversely proportional to its dielectric constant as

$$\frac{E_{norm1}}{E_{norm2}} = \frac{\varepsilon_2}{\varepsilon_1} \tag{3.1}$$

$$E_{tang1} = E_{tang2} \tag{3.2}$$

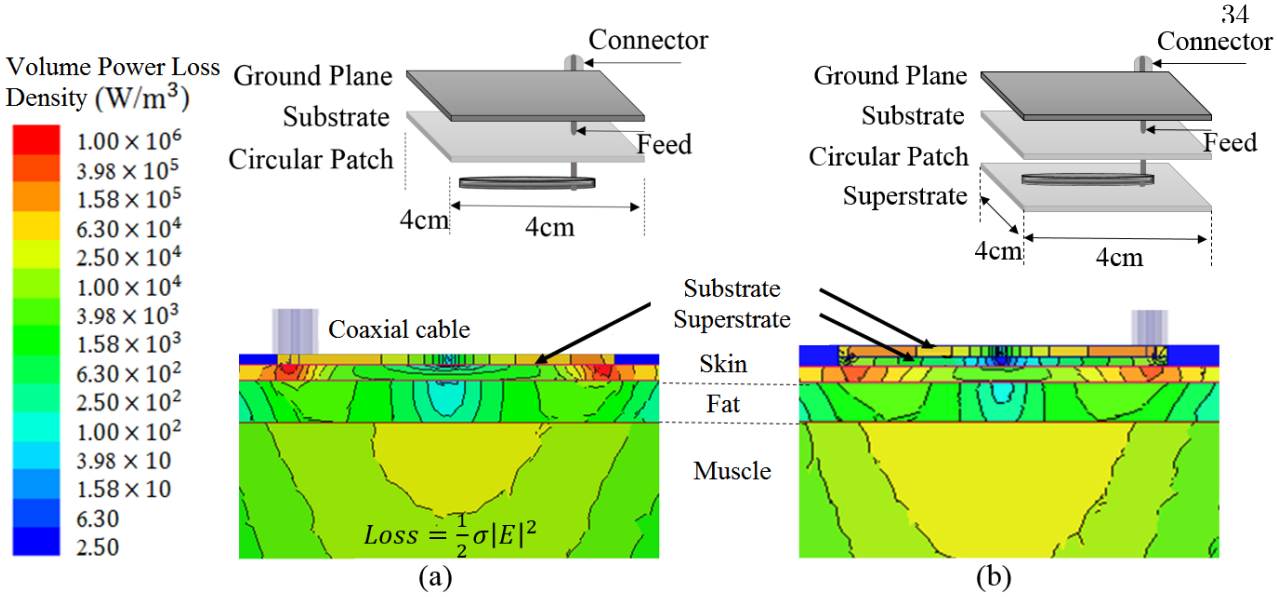

Figure 3.3: Volume loss density of circular patch with and without superstrate are compared. (a) Patch is designed to maximize power deposition into the buried muscle layer. (b) Adding appropriate superstrate matches the probe to deeper tissue layers and doubles the power transfer to the muscle layer. In this simulation, 2-mm and 5-cm Agar are used as skin and muscle phantoms and 5 mm FR4 is used as the fat phantom.

Considering these boundary conditions, adding an appropriate superstrate (cover) to the circular patch can reduce the absolute value of the electric field, and therefore the absorbed power, in the top skin layer.

Figure 3.3 shows that the absorbed power in the muscle increases from 33% to 61% for a 1.58-mm thick superstrate with ϵ_r=10.2. In Figure 3.4 the effect of the superstrate in the near field, is investigated in more detail. The normal E-field component is proportional to the ratio of the permittivities ($\approx$11) and conductivities ($\approx$19), (Figure 3.4-a). Adding a superstrate (ϵ_r=10.2) introduces a high dielectric-constant contrast (10.2:40) at the probe-skin interface, which results in confining E_{norm} to the low-loss superstrate. This effect significantly reduces the contribution of the skin in the total thermal noise power absorbed by the probe. Figure 3.4-b confirms the continuity of E_{tang} across the interface of tissue layers. Therefore, E_{tang} is the only immune component of E-field to high dielectric-contrast between tissue layers in the human body. Comparing Figure 3.4-c and d shows that E_{tang} is the dominant component of electric field in the muscle.

Since the thickness of tissue layers varies on different parts of the body, as well as from person

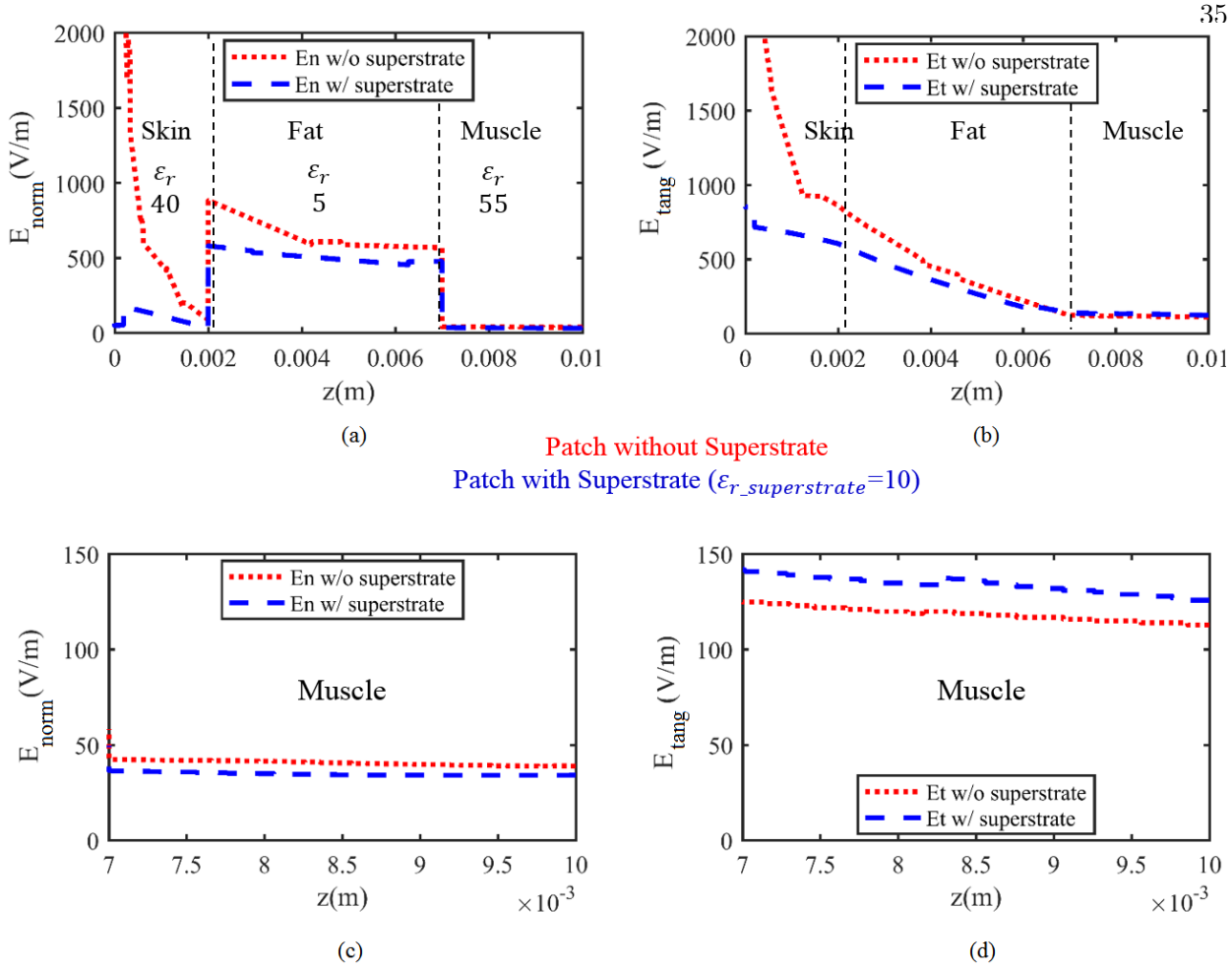

Figure 3.4: Simulated E_{tang} and E_{norm} in different tissue layers with an without probe superstrate. The skin surface is at z=0. (a) the normal E-field component is proportional to the ratio of the permittivities ($\approx$11) and conductivities ($\approx$19). (a) adding a superstrate (ϵ_r=10.2) introduces a high dielectric-constant contrast (10.2:40) at the probe-skin interface, which results in confining E_{norm} to the low-loss superstrate. This effect significantly reduces the contribution of the skin in the total thermal noise power absorbed by the probe. (b) this figure confirms the continuity of E_{tang} across the interface of tissue layers. Therefore, E_{tang} is the only immune component of E-field to high dielectric-contrast between tissue layers in the human body. (c) and (d): E_{tang} is the dominant component of electric field in the muscle.

to person, a superstrate also reduces the sensitivity of the probe to surrounding media. It should be noted that low-permittivity glue between substrate and superstrate introduces a small frequency shift which needs to be taken into account in the design.

Figure 3.5 shows a photograph of the probe which includes a high-permittivity (ϵ_r = 10,

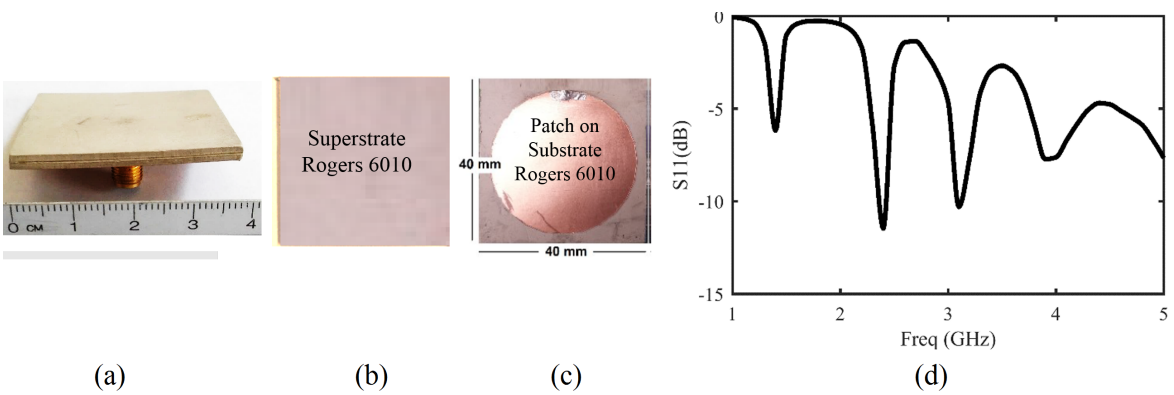

Figure 3.5: (a) Fabricated superstrate circular patch, (b) superstrate (cover), (c) patch, (d) Simulated matching on the tissue stack of skin, fat, and muscle.

Rogers 6010, 1.27 mm) superstrate. The probe is fabricated on a 1.27 mm-thick substrate and coaxially fed. The size of the ground plane and superstrate is $0.18\lambda_0 \times 0.18\lambda_0$ at 1.4 GHz. The measured return loss of the probe, calibrated to the SMA feed connector, is shown in Figure 3.5-d when placed on a phantom stack, consisting of a 2-mm layer of skin on top of a 5-mm thick fat and muscle. On this tissue stack, the match is about 7 dB at the design frequency. In order to improve the matching, the size of the probe should be further increased. In order to reduce the size of the probe and maintain a good match, a shorting-pin inductive loading technique is described in the next section.

3.2.3 Circular patch with superstrate and short-pin loading

In order to reduce the overall size of the probe, an inductive shorting pin to ground is used, Figure 3.6. Adding this parallel inductance to the probe shifts the resonant frequency of the probe to a lower frequency, reducing the overall patch diameter from 3.65 cm to 1.55 cm. For a wearable more compact probe, the size of the ground plane can be reduced by a factor of 4 (2cm×2cm) with only slight simulated degradation in RFI reception. Figure 3.6-a demonstrates the architecture of the circular patch with superstrate and shorting-pin loading. Figure 3.6-b-c shows the fabricated probe, while Figure 3.6-d shows the measured return loss of the probe for several scenarios, including a real human body (cheek) and different tissue phantoms including a two-layer phantom consisting of salmon, and water, and a three-layer phantom consisting of salmon, Rogers 6010, and saline.

The match at 1.4 GHz is better than 9 dB for all cases, with poor matching at the common cellular frequencies (0.9, 1.8 and 2 GHz). Although matching does not necessarily enhance the thermal noise power reception from the core tissue layers, it is important because of the generally very low SNR.

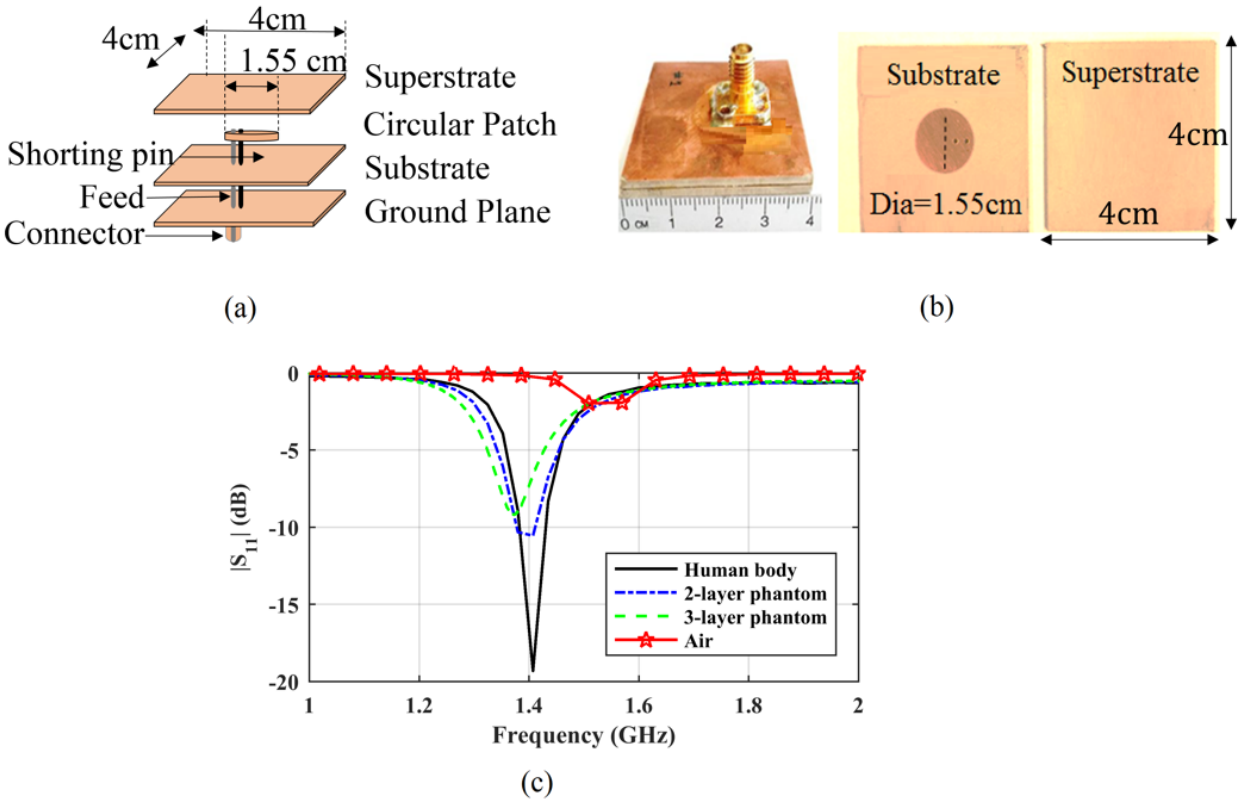

Figure 3.6: (a) Circular patch probe with superstrate and shorting pin. (b) photograph of fabricated probe layers, short-pin circular patch, cover, (b) measured impedance matching when probe is placed on a human body (cheek) and a two-layer phantom consisting of 2 mm of smoked salmon (representing skin), saline, as well as a three-layer phantom consisting of 2 mm salmon (skin), 1.27 mm Rogers 6010 (fat) and saline.

A simulation of VPLD pattern of this probe is shown in Figure 3.7-a. To validate this simulations and characterize the sensing region, this probe is tested in transmitting mode when placed on a layered phantom gel and 5 W of power at 1.4 GHz is fed to the probe from a 50-Ω connector. A ZHL-16W-43 power amplifier is used for 60 s to heat up the tissue phantoms. A temperature sensitive liquid crystal sheet (25-30°, Edmund Scientific) placed perpendicularly through the phantom stack displays the heating profile (directly proportional to loss) in the transparent Agar muscle

phantom. Figure3.7-b shows that the field penetrates 15 mm into the muscle layer following the profile from Figure3.7-a.

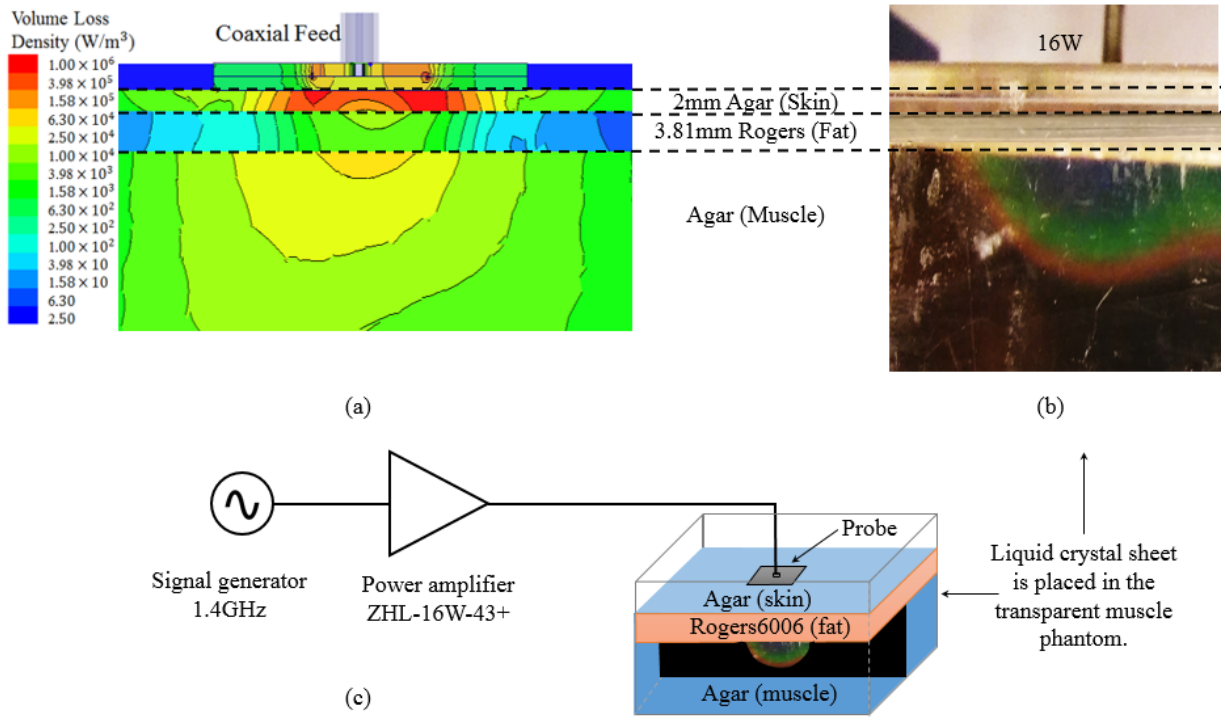

Figure 3.7: (a) Simulation of volume power loss density pattern of the probe placed on the stack of skin, fat, and muscle phantoms. Agar gel is used as skin and muscle phantoms, and three layers of Rogers6006 are glued together mimicking a thick fat phantom. (b) temperature profile is measured with a liquid crystal sheet placed in the transparent muscle phantom under the transmitting patch. (c) A ZHL-15W-43 16 W 50Ω power amplifier is used at 1.4 GHz to heat up the tissue phantoms.

Fig.3.8 shows the simulated volume loss density under the center and edge of the patch probe from Fig. 3.6. A patch antenna radiates from fringing field at the edges, and therefore it is reasonable to expect that the volume loss density will be high at the probe edges between the substrate and superstrate. This trend is followed in the first tissue layer under the probe. However, due to boundary conditions, the fields from the edges of the patch add in the region under the probe by superposition, enhancing the loss density in the fat and muscle layers.

Due to the good match of this probe to different tissue-phantom stacks and its small size, the patch probe with superstrate and shorting-pin is used in most of measurements in the future

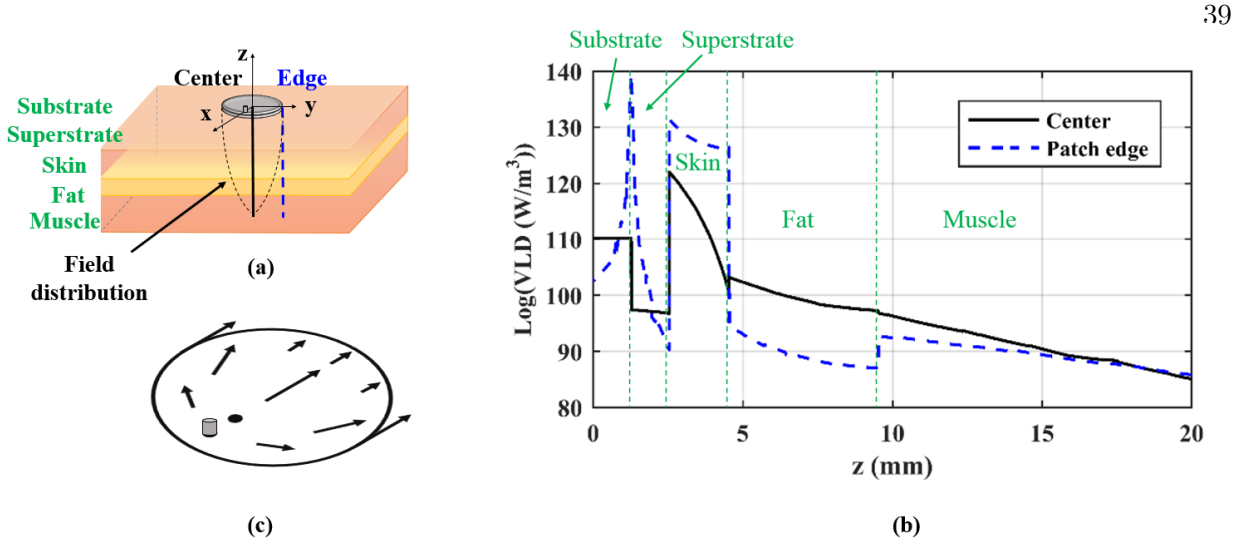

Figure 3.8: (a) The probe is placed on the stack of skin, fat, and muscle. (b) Simulated VLD is shown under the center and edge of the probe. It is reasonable to expect a high VLD on the patch (at the interface of substrate and superstrate). This trend is followed in the skin which is a very near proximity of the probe. (c) Simulated current distribution on the patch justifies higher VLD at the center compared to the edge in the fat and muscle layers. Fields from the edges add up under the center.

chapters.

3.2.3.1 Motivation for array design

Considering the high dielectric contrast between skin/fat and fat/muscle, it becomes apparent that having a thin layer of fat between skin and muscle layers results in a strong attenuation in the black-body power transfer from muscle to the probe, Figure 3.9. The received power by the radiometer is calculated using weighting function (WF) -a metric representing the percentage of received power from each layer, explained in detail in chapter 2. The probe is placed on the stack of skin (2 mm), fat, and muscle (50 mm). The thickness of fat is varied from 0 to 4 mm. The skin temperature is 32°C, the fat temperature is 33°C, and the muscle temperature is swept from 36°C to 42°C. Weighting functions of all tissue layers for 3 different thicknesses of fat are calculated using full-wave simulations and the received power of the radiometer is calculated based on the radiometer gain (explained in chapters 2 and 4). As illustrated in Figure 3.9, the amount of received power

by the radiometer decreases after adding 2 mm of fat to the tissue stack. However, since the fat is a low-loss tissue, further increase in fat thickness does not significantly reduce the received power by the radiometer. In order to increase the amount of received power from the buried muscle layer under a thick layer of fat, an array of these small probes can be integrated on a single substrate.

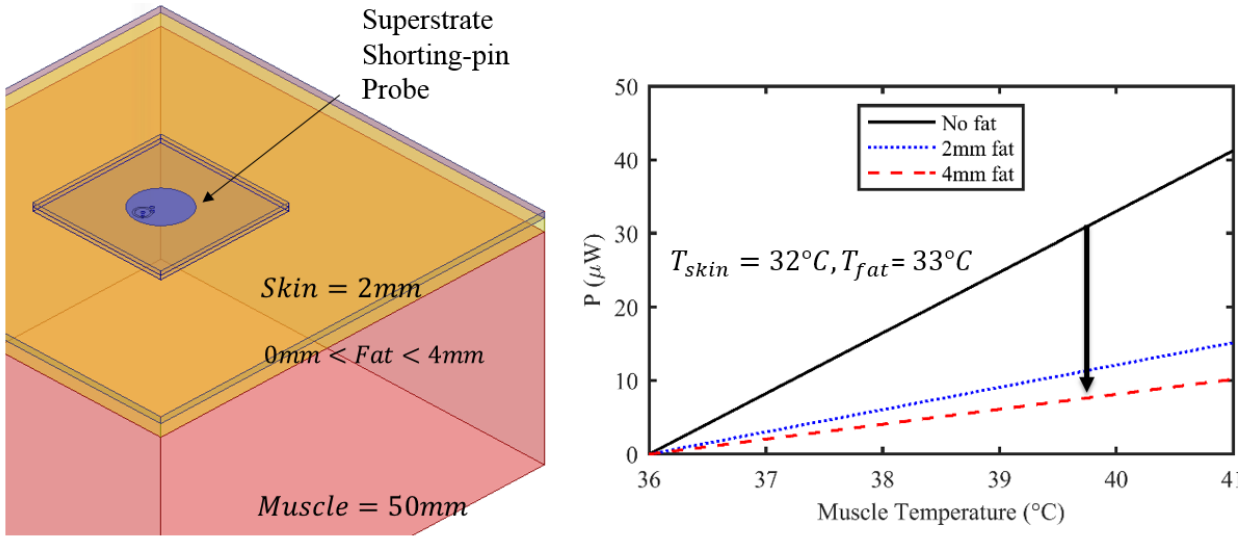

Figure 3.9: Effect of fat thickness on the received power by the radiometer. The variations in the radiometer output power is calculated. Compared to the no-fat scenario, adding 2 mm of fat significantly decreases the total received power by the radiometer. This is due to introducing the layer of low dielectric constant fat between the high dielectric constant skin and muscle layers. Electromagnetic properties of tissue layers are taken from Table 1.1.

3.2.4 Array of patch probes

Compared to a single element, an array of patch probes introduced in the previous section receives higher amount of thermal noise from deep tissue layers. This array can be integrated on the same 4 cm×4 cm substrate with a corporate feed based on Wilkinson combiners. A 4-1 combiner can add up the received power from each probe.

Figure 3.10-a shows the array structure. Figure 3.10-b shows the layers of fabricated array. Figure 3.10-c shows the measured return loss of the probe when it is placed on the stack of Agar, Rogers6006, and saline. Three layers of Duroid 6006 (each 1.27 mm-thick) are glued together for mimicking a thick layer of fat (3.81 mm-thick). This tissue stack is also used in Chapter 5 for

verifying the performance of the array. The return loss at 1.4 GHz is better than 10 dB.

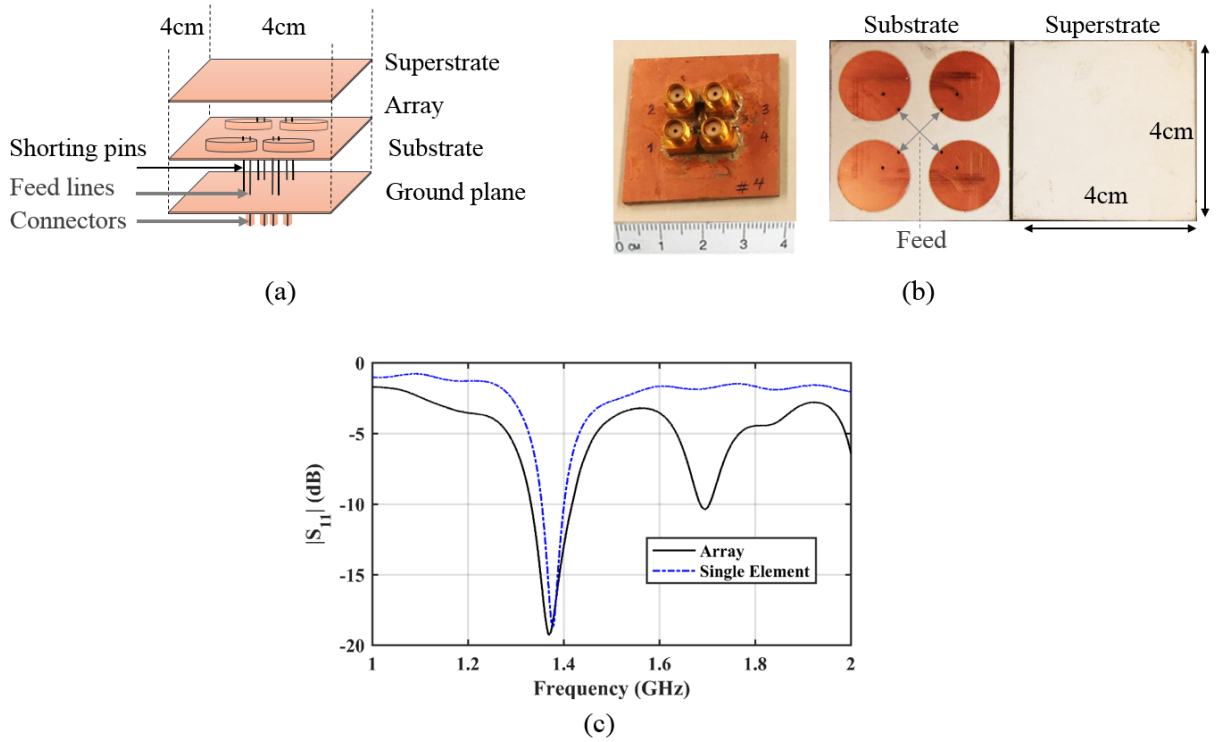

Figure 3.10: (a) Array of circular probes with a superstrate and shorting-pins, (b) Fabricated array on Rogers6010 1.27 mm, (c) Measured $|S_{11}|$ of array is compared to single element when both probes are located on a stack of 2 mm Agar (representing skin), 3.81 mm Rogers 6010 (fat), and saline (muscle).

Figure 3.11 shows a comparison of the VPLD of an element and a 2×2 array, when they are placed on the stack of Agar, Rogers 6010, and saline. Weighting functions for these probes are listed in Table 3.2. The percentage of power deposition to the muscle layer has increased from 34% for a single patch to more than 70% for an array of patches (these values are normalized to their total input power).

A Wilkinson corporate power combining network is designed on a Rogers 4003C 1.524-mm thick substrate (ϵ_r=3.55) in AWR. Figure 3.12 shows the fabricated feed network and measured return loss at each port, which is better than -15 dB at 1.4 GHz.

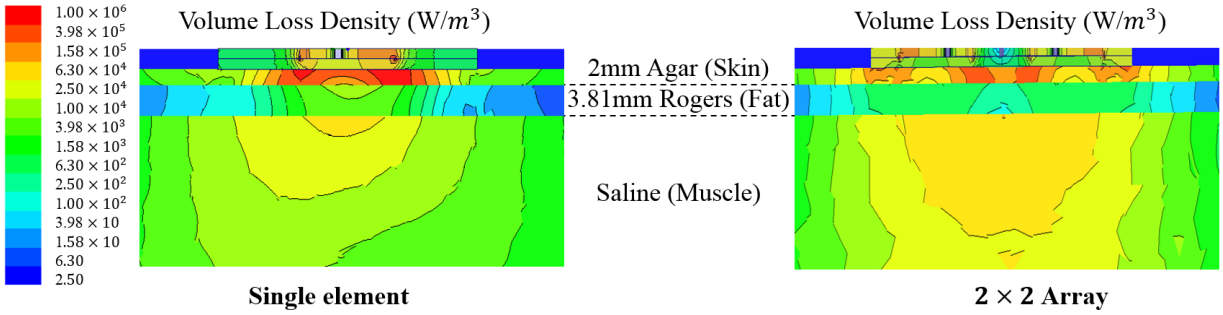

Figure 3.11: Comparing volume loss density for a shorting pin superstrate patch and an array of the same patch when both probes are located on a stack of 2 mm Agar (representing skin), 3.81 mm Rogers 6010 (fat), and saline (muscle). The size of the probes are kept 4 cm by 4 cm.

Table 3.2: Comparing weighting function and matching for a single probe and a 2×2 array on the stack of Agar (2 mm skin phantom), Rogers6006 (3.81 mm fat phantom), and saline. The percentage of power absorption in the muscle layer has increased from 34% for a single patch to 75% for an array of patch (these values are normalized to the total input power).

Architecture	S_{11} (dB)	Skin WF(%)	Fat WF(%)	Muscle WF(%)
Single element	-15.5	62.1	3.3	34.6
Array	-18.5	28	1	71

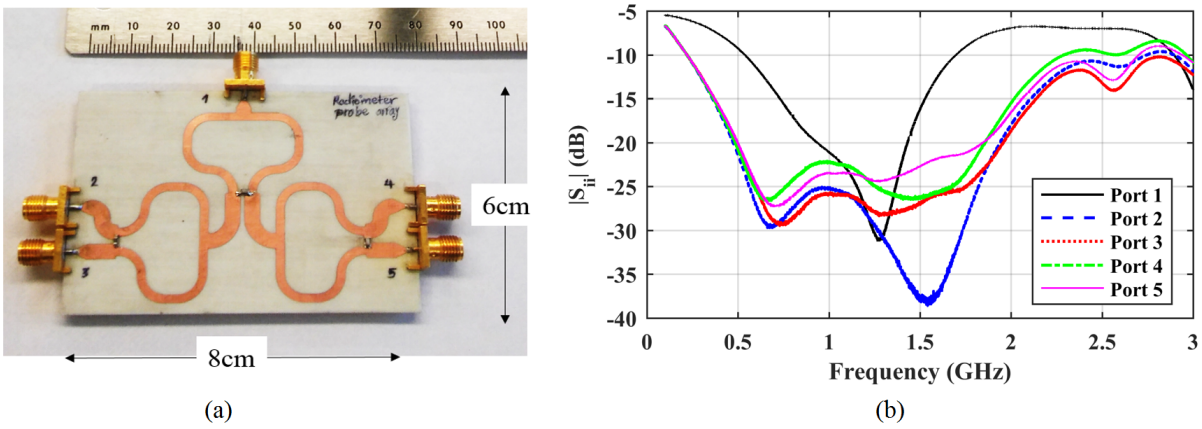

Figure 3.12: (a) A 1.4 GHz corporate feed network based on Wilkinson combiners is fabricated on a Rogers 4003C 1.524-mm thick substrate (ϵ_r=3.55). (b) Measured return loss at different ports.

3.2.5 Slot probe with superstrate

In addition to patch probes, slot probes with superstrates are designed, given the tangential E-field nature of their radiation. Figure 3.13 illustrates two different designs; ring slot; and flower-shaped slot. The ring slot probe from Figure3.13-a, can provide good power deposition into the muscle. To reduce the size of the ring, a meander shape ring slot (flower slot) is designed, resulting in an increase of the power deposition to the skin, Figure3.13-b.

Table 3.3: Comparing different near-field probes at 1.4 GHz. Probes are positioned on the stack of skin-fat-muscle (Agar-FR4-Agar). The size of all probes kept 4 cm×4 cm.

Architecture	S_{11}(dB) @ 1.4 GHz	Skin WF(%)	Fat WF(%)	Muscle WF(%)
Ring slot	-15	41.6	1.2	57.2
Flower slot	-9	48.2	0.6	51.2

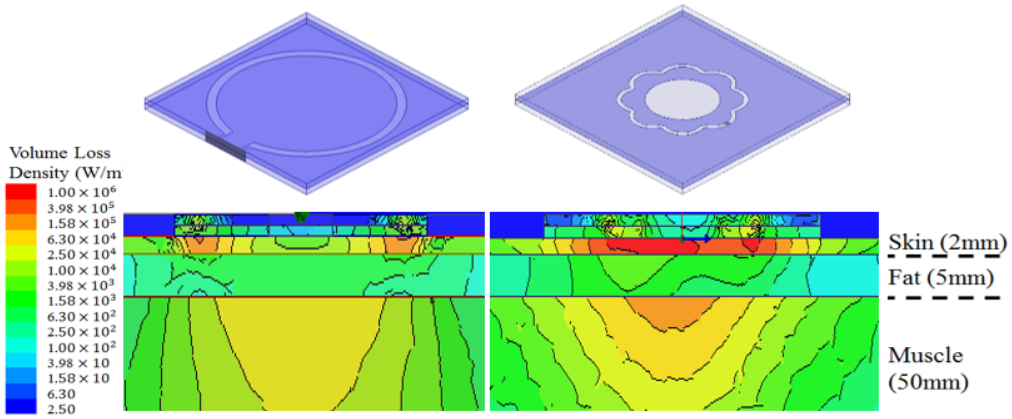

Figure 3.13: Slot architecture, by nature, provides a strong tangential E-field at the interface of skin-probe which does not attenuate at the interface of tissue layers. Different slot probes are simulated in HFSS and compared in terms of matching and power deposition into different tissue layers. The ring slot probe can provide strong power deposition in the muscle. To reduce the size, a meander shape ring slot (flower slot) is designed. The reduced size of the slot reduces the power receiption from muscle layer.

3.3 Modeling analysis and validation

Numerical analysis tools can perform full-wave simulation that include full body models for various human body types. The IT'IS institute (ETH, Zurich) completed the "virtual family", which can be imported into a finite-difference time-domain method, such as Sim4Life from Zurich MedTech [65]. These anatomically complete models allow the user to import complex permittivity parameters for each of the tissues. Figure 3.14 shows an example of a simulated VPLD with 3 slab layers of skin, fat, and muscle, with electrical properties from [42] and [47]. In order to validate HFSS simulations of the layered tissue model, the circular patch probe with superstrate and shorting-pin is simulated in Sim4Life and return loss and weighting functions from two software tools are compared. Figures 3.14 and 3.15, show a comparison of resonance frequency and normalized volume power loss density (WF) in different tissue layers. The slight disagreement is due to different mesh sizes in HFSS and Sim4Life.

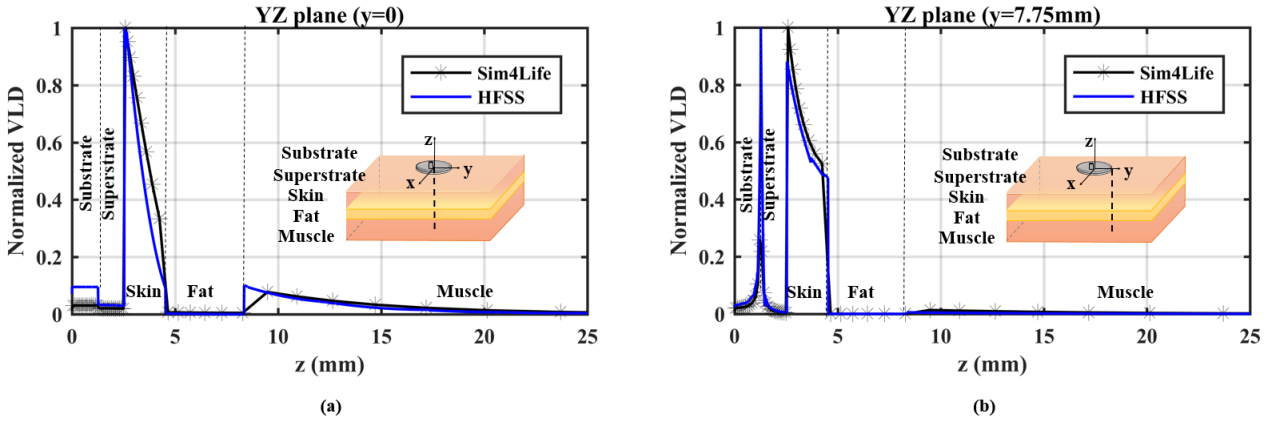

Figure 3.14: Simulated normalized volume power loss density (VPLD) of the probe placed on the stack of skin, fat, muscle in HFSS and Sim4Life. The VPLD is shown at two coordinates under the center (a) and under the edge of the probe (b).

3.4 Influence of layer thickness variation on temperature estimation

The thicknesses of tissue layers vary on different parts of the body, as well as from person to person. Fat tissue exhibits more thickness variability compared to the superficial skin layer. The

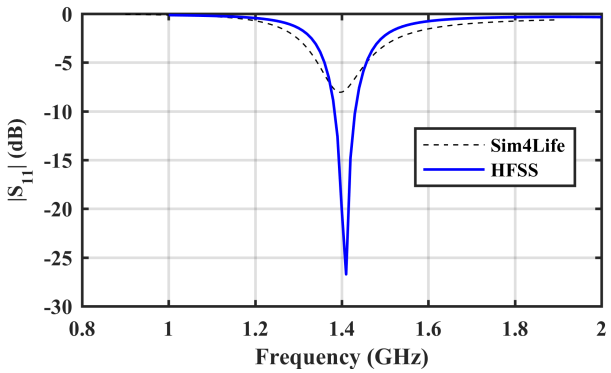

Figure 3.15: Simulated return loss of the probe placed on the stack of skin, fat, muscle is compared in HFSS and Sim4Life.

goal of this section is to investigate the error in temperature retrieval due to wrong estimation of the weighting functions. To quantify the effect of fat thickness variability in buried tissue temperature retrieval, the radiometric data is first created from accurate weighting functions, then data is created from estimated weighing functions, and these two sets of data are compared. The following assumptions are made: the skin is assumed to be 1.2 mm thick, muscle is 5 cm thick, and the fat thickness is assumed to be 4 mm, while in reality it can vary between 2 to 8 mm. The average skin temperature is supposed to be $T_{skin} = 33°C$, T_{muscle} is swept from 35°C to 39°C, and for simplicity, the temperature of fat is assumed to be $T_{fat} = (T_{skin} + T_{muscle})/2$.

Weighting functions of skin, fat, and muscle are calculated for different thickness of fat as shown in Table 3.4. As seen in this table, the weighting function of the fat only slightly varies as the fat thickness changes from 2 to 8 mm, reducing the sensitivity of core tissue temperature to thickness of fat. This is due to low conductive loss of this tissue layer.

To quantify the effect of fat thickness variability in buried tissue temperature retrieval, following analysis is performed: first, the real radiometric temperature is obtained from the real temperature and weighting function of tissue layers from Eq. (3.3), then radiometric temperature is calculated using the reference weighting functions for 4 mm of fat, Eq. (3.4). The real radiometric temperature can be obtained from Eq. (2.20) and is given here for completeness

Table 3.4: The probe is placed on the stack of skin, fat, and muscle. The thicknesses of skin and muscle are 1.2 mm and 5 cm. Fat thickness is varied from 2 to 8 mm. Weighting functions are obtained from HFSS simulations. Electromagnetic properties of the tissues presneted in Chapter 1.

Frequency (GHz)	Fat thickness	Skin WF(%)	Fat WF(%)	Muscle WF(%)
1.38	2 mm	41.8	16.2	41.8
1.40	4 mm	54.3	17.2	28.3
1.41	6 mm	60.7	17.8	21.4
1.42	8 mm	65.8	18.1	16.4

$$T = T_p W_p + T_s W_s + T_f W_f + T_m W_m \tag{3.3}$$

in this equation, T is the real radiometric temperature, T_p and T_s are the probe and skin temperatures measured by temperature sensors, T_f is the temperature of the fat layer which is estimated by averaging the skin and muscle temperatures, and T_m is the real muscle temperature.

Similarly the estimated muscle temperature from the reference weighting functions can be written as

$$T = T_p W_p^{'} + T_s W_s^{'} + T_f^{'} W_f^{'} + T_m^{'} W_m^{'} \tag{3.4}$$

where T is the measured radiometric temperature, $T_f^{'}$ is the temperature of the fat layer which is estimated by averaging the real skin temperature and estimated muscle temperature, and $T_m^{'}$ is the unknown muscle temperature.

The radiometric temperature T can be easily obtained by the radiometer measurement and the unknown core tissue temperature can be expressed as

$$T_m^{'} = \frac{T - T_p W_p^{'} - T_s W_s^{'} - (T_s W_f^{'})/2}{W_f^{'}/2 + W_m^{'}} \tag{3.5}$$

Therefore, by direct thermocouple measurement of the surface tissue layer (skin), and using estimated (reference) weighting functions, the unknown core tissue layer temperature can be obtained. Another known parameter, is the average core body temperature of human body at rest,

37°C. Also, by adjusting the offset before starting an activity, the data can be further calibrated. For instance, an athlete at rest has the average core body temperature of 37°C while the estimated core tissue temperature at rest deviates from this value for incorrect estimation of fat. Therefore, by adjusting the offset before starting an activity, the accuracy of the measurement can be improved.

Figure 3.16 compares the real and estimated values of core tissue temperature. As mentioned earlier, 4 mm is selected as our reference thickness for the fat layer, then $W_{tissue_{est.}} = W_{tissue_{4mmfat}}$. This analysis demonstrated that if fat thicknesses vary from 2 mm to 8 mm, the estimated muscle temperature does not vary more than 0.6°C.

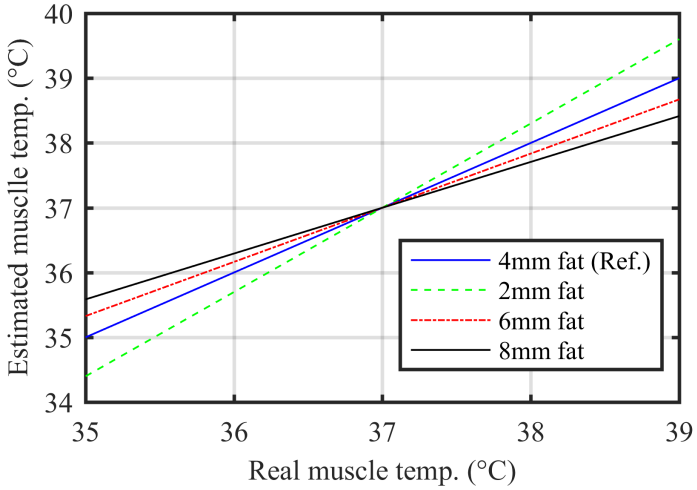

Figure 3.16: The estimated muscle temperature is compared with real muscle temperature when it varies from 35 to 39°C. The estimated muscle temperature does not deviate from the real muscle temperature more than 0.6°C for fat variation of 2 mm to 8 mm.

According to Table 3.4, the resonance frequency of the probe varies by changing the fat layer thickness. This is expected as increasing the fat thickness reduces the effective dielectric constant of the probe which in turn increases its resonance frequency. This frequency shift can provide valuable information about the thickness of the fat layer, i.e., by sweeping the center frequency of the radiometer for picking the maximum thermal noise power, the unknown thickness of low-loss, low-dielectric constant tissue (e.g., fat, cancellous bone, cortical bone) between the skin and muscle layers can be roughly estimated.

Another source of uncertainty in temperature retrieval is sweating. This issue begins to manifest itself when sweat thickness varies during the exercise. This fluid has a high dielectric constant (ϵ=81 at 1.4 GHz [66]) which shifts the resonance frequency of the probe to the lower frequencies and reduce the received power by the probe. However, the weighting function at the resonance frequency and non-resonance frequency of the probe are not very different. Currently, wrist-band wearable heart rate monitors are not accurate during heavy exercise, forcing users to dry the sensor. Using sweat-band or anti-sweat sprays can improve the accuracy of measurement.

3.5 Probe placement

So far, the probes were optimized on the tissue stack of skin, fat, and muscle. However, in reality, the human-body exhibits a more complicated composition. To illustrate the effect of specific tissue layers, the probe is placed on the forehead and sternum, and thermal noise power reception from each tissue layer is investigated.

First, VPLD is investigated on the sternum. Human heart is situated right behind and slightly on the left side of the sternum. A six-layer stack of skin, fat, rib (composed of cortical, cancellous, and cortial bones), and heart muscle is considered in the analysis. A cavity in the left lung houses the heart which avoids probe loading with variable electromagnetic properties of lung during inhalation and exhalation. Figure 3.17 shows the VPLD obtained from numerical simulations in HFSS. Electromagnetic properties of the tissue and the average thickness of each layer are obtained from [42] and [36] as listed in Table 3.5.

Table 3.5: Average thickness, electromagnetic properties, and weighting function of tissue layers when probe is placed on the Sternum [42] and [36].

Layer	Tissue	Avg. Thickness	Dielectric constant	Conductivity (S/m)	WF
1	Skin	1.2 mm	39.6	1.035	43.8
2	Fat	4 mm	11.1517	0.1498	26.2
3	Cortical bone	2 mm	12.05	0.211	8.0
4	Cancellous bone	4 mm	19.9	0.469	17.3
5	Cortical bone	2 mm	12.05	0.211	2.4
6	Heart	5 cm	57.538	1.5132	2.0

According to Figure 3.17, the volume power loss density in the core heart layer is only 2% of total power received from all tissue layers. This is due to relatively thick cancellous bone which has a higher amount of loss compared to cortical bone and fat layers.

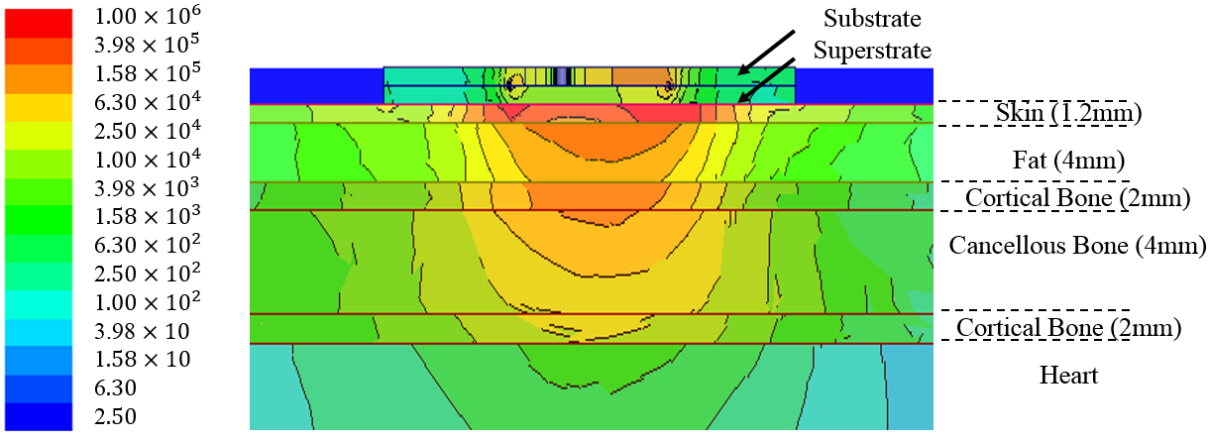

Figure 3.17: Simulation of volume loss density (W/m^3) on the stack of skin, fat, rib (composed of cortical, cancellous, and cortial bones) and heart.

Next, the probe is placed on the forehead. The brain is situated under the stack of scalp and skull, which is composed of cancellous, and cortical bones. The thickness of a skull depends on a number of factors, including gender and age. The average skull thickness for men is 6.35 mm, while this value for women is as thick as 7.112 mm [67]. Electromagnetic properties of the tissue as well as average thickness of these layers are obtained from [42], [67], [68], and [69] as listed in Table 3.6. Illustrated in Figure 3.18, the pattern of volume loss density shows that a 28% of the total power is received from the brain layer. Therefore, this probe received a higher amount of power from the brain compared to the heart. As stated earlier, the thick and lossy layer of cancellous bone in the sternum reduces the power reception from the heart layer. In addition, the average thickness of tissue layers from the skin surface to the heart is 13.2 mm while this thickness for skin forehead to the brain almost is 9.4 mm.

Table 3.6: Average thickness, electromagnetic properties, and weighting functions of tissue layers when probe is placed on the forehead [42], [67] [68], and [69].

Layer	Tissue	Avg. Thickness	Dielectric constant	Conductivity (S/m)	WF
1	Scalp	4 mm	39.6	1.035	51.3
2	Skull (Cortical)	2.2 mm	12.05	0.211	8.1
3	Skull (Cancellous)	1.8 mm	19.9	0.469	9.0
4	Skull (Cortical)	1.4 mm	12.05	0.211	3.6
5	Brain	5 cm	47.3	1.5	28.0

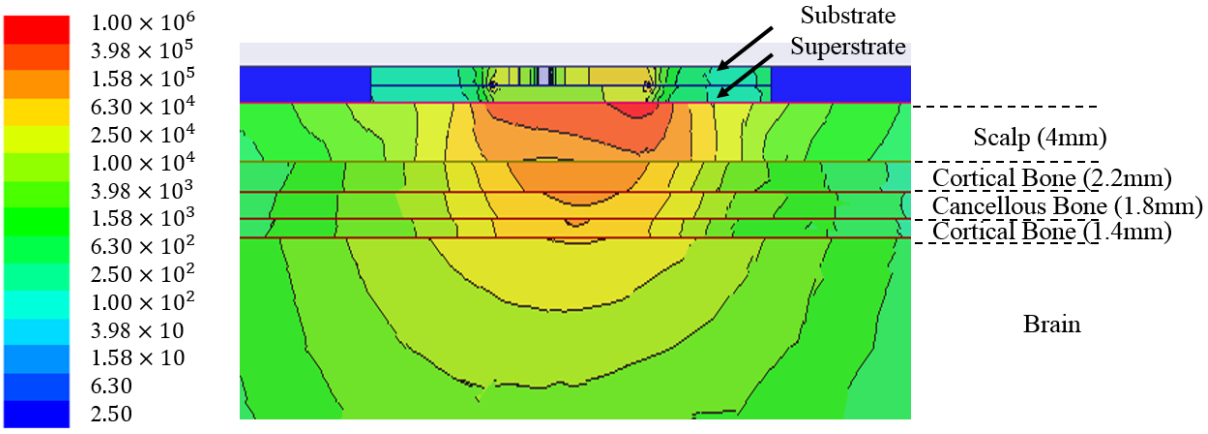

Figure 3.18: Simulation of volume loss density (W/m^3) on the stack of scalp, skull (cortical, cancellous, and cortial bones) and brain.

3.6 Summary

This chapter details the probe design for human body microwave thermometry. The results from this chapter demonstrate an approach toward designing near-field probes, capable of detecting small temperature variations of deep tissue layers. Background information on previously published near-field probes is summarized. Decomposing the electric field into the normal and tangential components reveals important information on the design approach of the near-field probes loaded by the human body. High dielectric constant contrast between the skin, fat, and muscle tissue layers, suggests using probes with dominant tangential component of electric field, such as patch and slot architectures. Also, it is shown that adding a layer of low-loss, low-dielectric constant superstrate can further reduce the contribution of superficial tissue layers in the received thermal noise.

Several near-field probes matched to a stack of skin (Agar phantom), fat (FR4 substrate) and muscle (Agar phantom) are designed and summarized in Table 3.7, starting from a circular patch as a RFI-shielded planar design. A superstrate is then added to improve performance, and finally a shorting pin (inductive loading) is added to reduce the size of the patch. A 2×2 array of the miniaturized probe is then designed. A 1.4 GHz 4-1 power combiner was designed to combine the thermal noise received from all the probes. Several slot architectures are also examined on the same tissue stack. Superstrate slot architectures have higher bandwidth and receive a high amount of thermal noise from the muscle layer, making them more susceptible to RFI while patch structures have the advantage that the ground plane allows for easy integration with radiometer circuitry and also minimizes the amount of RFI.

The probes are designed through simulations with the commercial full-wave FEM simulator, HFSS, and volume power loss density in the tissue layers for different probes are compared. The most promising designs are validated either with a FDTD commercial code (Sim4Life) or with measurements. The near-field pattern of the circular patch with superstrate and shorting-pin is measured in the reciprocal (transmitting) mode using a temperature sensitive liquid crystal sheet placed inside a transparent phantom and heated by a power amplifier at 1.4 GHz.The effect of tissue thickness variations in temperature retrieval is analyzed, and finally probe placement on the sternum and forehead are discussed. Increasing the fat thickness has shown to reduce the overall received power by the probe. This issue which can be solved by using an array.

The contributions related to the content of this chapter are reported in in [70], [71], and [72].

Table 3.7: Comparing some of the near-field probes at 1.4 GHz. Probes are positioned on the stack of skin-fat-muscle (Agar-FR4-Agar).

Probe	Architecture	$\|S_{11}\|$(dB)	Skin WF(%)	Fat WF(%)	Muscle WF(%)	Size
(a)	Patch	-13	65.5	1.1	33.4	4 cm×4 cm
(b)	Superstrate patch	-6.25	38.1	1.2	60.7	4 cm×4 cm
(c)	Superstrate shortpin patch(SSP)	-15.5	62.1	3.3	34.6	4 cm×4 cm
(d)	Array of SSP	-18.5	23.4	1.6	75	4 cm×4 cm
(e)	Superstrate cross slot	-12	26.7	2.5	70.8	4 cm×4 cm
(f)	Superstrate ring slot	-15	41.6	1.2	57.2	4 cm×4 cm
(g)	Superstrate flower slot	-9	48.2	0.6	51.2	4 cm×4 cm

Chapter 4

Radiometer Design

Contents

4.1 Introduction

As mentioned in Chapter 2, materials at non-zero temperature radiate electromagnetic energy proportional to their temperature. A radiometer is a device used for measuring electromagnetic radiated power from an object and therefore indirectly the object temperature, if the emissivity is known. Radiometry has a variety of applications, e.g., it can be used in radio astronomy [57], [56], terrestrial remote sensing [73], environmental observation such as weather and climate forecasting [74], management of ecosystems, monitoring fire, food, transportation, agriculture, energy,

and water, as well as biology, ecology, and disease vector mapping. Radiometry can also be used in surveillance for example air traffic control [75], homeland and border security [76], brick manufacturing, and many more applications [77]. In most of these applications, the object of unknown temperature is in the far-field of the antenna, which receives plane waves radiated by the object. In the core body thermometry case, however, the power radiated by the tissues is received by a probe situated in the near field, on the skin.

Nevertheless, one of the standard radiometer architectures will be applicable, and the goal of the next section is to provide background that explains the choices of radiometers adopted for the thermometery work.

4.2 Background: Radiometer architectures

A radiometer can have one of the two basic architectures; direct or heterodyne detection. In the direct conversion method a square-law power detector is used to give an output dc voltage related to the input power. Direct down conversion with an LO equal to the input frequency suffers from LO leakage and DC offset, even-order nonlinearity, flicker noise, and I/Q mismatch. In a heterodyne architecture, filtering and amplification are performed at a lower IF frequency, where amplifiers and filters are easier to implement. In this method, stability is easier to control [78]. There are several types of radiometers based on one of the above principles, as reviewed in the next sections.

4.2.1 The total power radiometer

Figure 4.1 shows the block diagram of a simple total power radiometer. The input signal is received by the antenna at an equivalent noise temperature T'_A amplified by a low-noise amplifier (LNA), and filtered. According to Friss NF equation, the LNA should be placed as close to the antenna as possible to minimize the system noise figure. A diode detector, in the square-law regime (x^2), produces a DC voltage proportional to the input power. The output is then filtered and integrated with a low-pass filter (LPF), over a time constant τ, to improve the signal-to-noise ratio,

and thus, indirectly the temperature detection resolution.

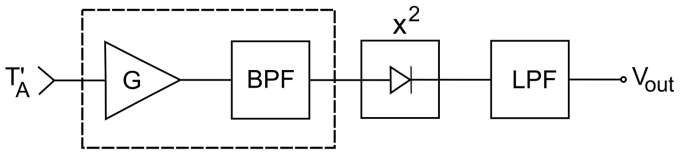

Figure 4.1: Block diagram of direct-detection total-power radiometer [57].

The sensitivity, or radiometer resolution, is one of the most important specifications in any radiometer and is defined as the minimum change in the system temperature which produces a detectable change in the dc level of the output voltage. According to [57], for an ideal radiometer with no gain fluctuation, the sensitivity is equal to

$$\Delta T = \frac{T'_A + T_{rec}}{\sqrt{B\tau}} \tag{4.1}$$

where ΔT is the minimum detectable change in the radiometric antenna temperature of the observed object. T_{rec} is the receiver equivalent input noise temperature and B is the bandwidth of the system.

The simple architecture of Figure 4.1 cannot be used in commercial radiometers due to the adverse effects of gain fluctuation. In the square-law region of diode, the output voltage of the radiometer is the product of gain and system temperature. Therefore, any gain variation in the system can be misinterpreted as a temperature variation.

Slow variations of gain can be eliminated by calibration, however, fast variations remain a problem. If gain fluctuations are noticeable, the sensitivity must be modified to

$$\Delta T = (T'_A + T_{rec})\sqrt{\frac{1}{B\tau} + \left(\frac{\Delta G}{G}\right)^2} \tag{4.2}$$

in which G is the total gain of the radiometer and ΔG is the rms value of the gain fluctuations [57].

4.2.2 The Dicke radiometer

To minimize the adverse effect of gain fluctuation in radiometers, an approach was proposed by Dicke, 4.4, in which the input of the radiometer is periodically switched between the antenna and a matched reference load at a fixed temperature T_{ref}. This switch is referred to a Dicke switch. The matched load can be considered to be a well known a noise source. By periodically using this known source at the receiver input, gain fluctuation can be determined, thus calibrating the radiometer.

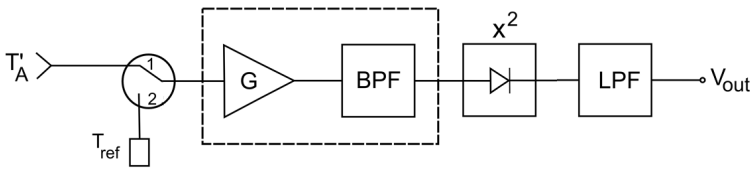

Figure 4.2: Dicke radiometer block diagram [57].

The Dicke architecture can be extended to two known noise sources for increased sensitivity. By using a single-pole triple-throw switch, over each switching period both the "cold" and "hot" load can be compared, thus determining T_{sys} for each cycle of the Dicke switch. The hot noise source can be an avalanche diode, e.g., as in the Agilent 346A. This noise source has an excess noise ratio (ENR) of 5.17 dB at 1.4 GHz. The ENR is a way of describing the noise, calculated from the hot and cold noise temperatures using

$$ENR = 10log_{10}\left(\frac{T_h - T_c}{T_o}\right) \tag{4.3}$$

where T_o is the standard temperate of 290K. Noise temperatures T_h and T_c are hot and cold noise temperatures. The ENR calibration of diode noise sources assumes $T_c = T_o$. For a hot noise source which is not at the room temperature, T_c should be specified as room temperate.

To reduce the noise source temperature, an attenuator can be used. The noise source temperature should be adjusted to $T_h = T_{h0}L + (1 - L)T_p$, where T_{h0} is the hot noise temperature without attenuator and L and T_p are the loss and physical temperature of the attenuator. In this

work, a 2.88 dB attenuator added to Agilent 346A noise standard resulting in 778 K of hot noise temperature at 1.4 GHz.

Illustrated in Figure 4.3, the output voltage of the radiometer is linearly related to the noise temperature of the input source in the square-law region of the output detector. Therefore, it is sufficient to measure the output voltage corresponding to each of two input noise temperatures to establish the calibration line. This line then is used for converting the output voltage of the radiometer to detect unknown temperature of the probe as

$$T = T_c + (T_c - T_h)\frac{V_c - V}{V_h - V_c} \tag{4.4}$$

where T_c and T_h are the cold and hot noise source temperatures and V_c and V_h are the cold and hot noise source voltages, respectively.

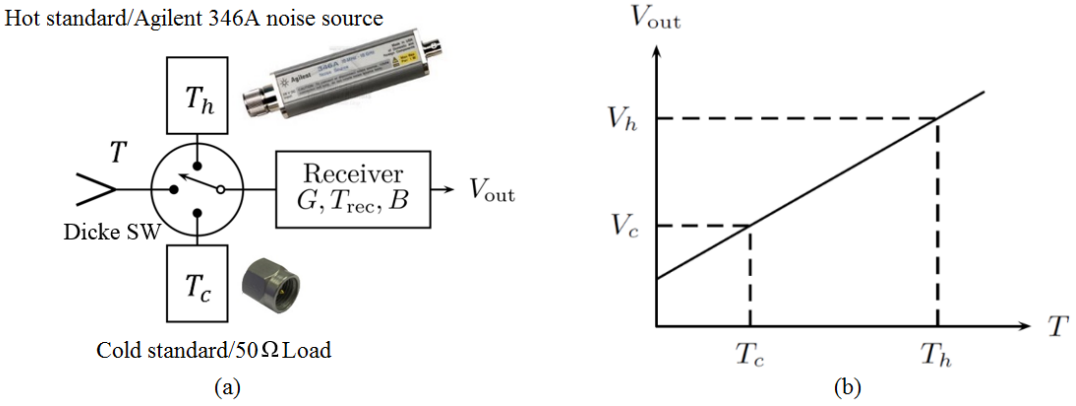

Figure 4.3: (a) Radiometer Calibration using Agilent 346A noise (hot noise) and 50 Ω cold noise sources. (b) Calibration line.

Other methods include a load placed in liquid nitrogen for a temperature of 77 K (cold noise) and then measured at room temperature (hot noise). For a wearable radiometer it is not practical to use a liquid nitrogen to cool a load. Also, since the human body temperature does not vary much, it is not necessary to use very cold or very hot noise sources and two simple on chip calibration standards capable of different noise temperatures are sufficient. The reference noise temperatures for our application include a hot noise source from Agilent, and a temperature controlled 50 Ω load

connected to the input of the radiometer. For a compact-size hot noise source, an LNA, an avalanche diode, or a hot matched load may be used.

The resolution of direct detection radiometer with two known noise sources can be written as

$$\Delta T = \frac{2\Delta T_{RMS}}{|T_h - Tc|}\sqrt{(\frac{T_h + Tc}{2} - T)^2 + \frac{1}{2}(T_h - T_c)^2} \tag{4.5}$$

Therefore, a big difference between T_h and T_c provides a better resolution. Also, it is better to operate T in around midway between T_c and T_h. ΔT_{RMS} is inversely proportional to the bandwidth and integration time of the radiometer. So, increasing these two parameters can further improve the temperature resolution.

4.2.3 The balanced radiometer

Another method of gain fluctuation mitigation is a balanced radiometer architecture. In this method, the output of a calibrated total power radiometer is passed through a LNA and filter incident on a diode detector. After square-wave detection, the output voltage of the detector becomes

$$V = \begin{cases} C_d GKB(T'_A + T_{rec}) & \text{if } 0<\text{t}<\tau/2, \\ C_d GKB(T_{ref} + T_{rec}) & \text{if } \tau/2 < t < \tau. \end{cases} \tag{4.6}$$

where T'_A is the calibrated radiometric temperature of the antenna when there is no cable loss, explained in chapter 2. T_{ref} is the temperature of reference-source noise, T_{rec} is the receiver noise temperature, τ is the period of one switching cycle and C_d is the square-law detector power sensitivity constant (V/W), Fig.4.4. Then, the voltage is synchronously demodulated so that the dc components of the reference and antenna signals are subtracted as follows:

$$V_{syn} = \frac{1}{2}(V_{ant} - V_{ref}) = \frac{1}{2}C_d GKB(T'_A - T_{ref}) \tag{4.7}$$

After integrating the voltage, the output will be proportional to $(T'_A - T_{ref})$ which is independent of receiver noise temperature. The gain variations is this architecture can be minimized by two methods: (1) controlling T_{ref} to be equal to T'_A, and (2) adjusting the gain stages in the demodulator to make $V_{out} = 0$. By making $T'_A = T_{ref}$, the radiometer is said to be balanced, and the radiometric resolution will be

$$\Delta T = 2\frac{T' + T_{rec}}{\sqrt{B\tau}} \tag{4.8}$$

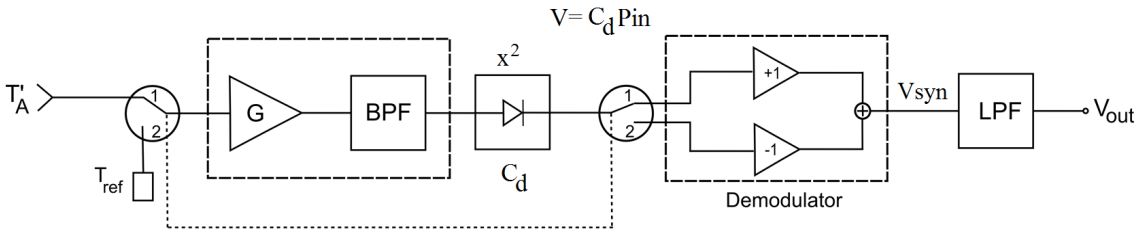

Figure 4.4: The balanced radiometer block diagram [57].

Although gain variation effects are reduced in a Dicke architecture, the antenna input is only receiving power half of the time and therefore, its resolution will be twice that of the simple architecture presented in Figure 4.1. The switching time, in a Dicke architecture, should be fast enough in order to maintain a constant gain during the switching cycle.

A Dicke radiometer can be automatically balanced using several methods: (1) reference channel noise injection; (2) antenna channel noise injection; and (3) gain modulated radiometer. These methods are described here in detail in, e.g. [57]. For the application addressed in this thesis, a simple Dicke architecture is chosen due to the desire to minimize the circuit.

4.3 Radiometer design procedure

In order to detect very small temperature variations in deep tissue layers, the radiometer should have high sensitivity, low noise, low gain drift and it should be stable. For initial proof-of-principle, a calibrated total power Dicke radiometer with the following design procedure is imple-

mented:

- Choose the frequencies of operation based on low interference (quiet protected band) and penetration depth in tissue.
- Design a detector matched to 50Ω for the selected frequency bands, e.g. using a Schottky diode matched with lumped surface-mount components.
- Choose the desired power levels in the linear region of the square-law detector, giving the output power of the radiometer.
- Based on expected tissue temperature variations and the thermal noise approximation $P = kTB$, where $k = 1.3810^{\smile}23J/K$ is the Boltzmann constant, T is the temperature in Kelvin, and $B = 27\,MHz$, is the radiometer bandwidth, and typical body temperature ($T = 310$ K), a matched probe should be receiving -100 dBm.
- Design the receiver front-end to have a gain that stays above the noise floor of the detector.
- Ensure that the noise figure of the system meets the design requirements for receiver sensitivity by proper component selection.

4.4 Connectorized radiometer

In order to keep the input power within the square-law region of the diode detector, 45 dB of gain is required [54]. For a resolution of $\Delta T = 0.2\,K$, to determine the required receiver temperature, the maximum integration time is τ= 0.333 s. The corresponding noise figure is NF =3 dB. With this information, an initial version of the radiometer implemented [36]. The radiometer components, listed in Table 4.1, are selected to achieve the required gain, with minimum cascaded noise figure. The switch in the block diagram of Figure 4.5 is required to calibrate the radiometer. T_h and T_c are hot and cold calibration standards, in this case an Agilent 346A noise source and a matched load at room temperature, respectively. An output voltage of 127.6 μV for an input power of -100 dBm was measured and the measured frequency response of the radiometer shows about 500 MHz of operating

Table 4.1: Components of 1.4 GHz radiometer version 1

Component	G(dB)	NF(dB)	Part number	Manufacturer
SW_1	-2	2	HMC345LP3	Analog Devices
LNA_1	18.5	1.1	Ramp-33LN+	Mini-Circuits
$BPF_{1/2}$	-2	2	VBFZ-1400	Mini-Circuits
LNA_2	35	0.6	Tamp-1521GLN+	Mini-Circuits

bandwidth. The square-law diode detector in Figure 4.5 is a Skyworks Schottky diode SMS7630-079 and is matched with a lumped element LC match (C=4.7 pF, L=15 nH). The measured responsivity of the square-law detector is shown in Figure 4.6 and is seen to be 25mV/uW at 1.4 GHz. The detector is matched best at 1.4 GHz when driven with an RF input power of -40 dBm. This version of the radiometer suffers from occasional oscillations. Integrating all components into a circuit board reduces the RFI reception and improves radiometer stability.

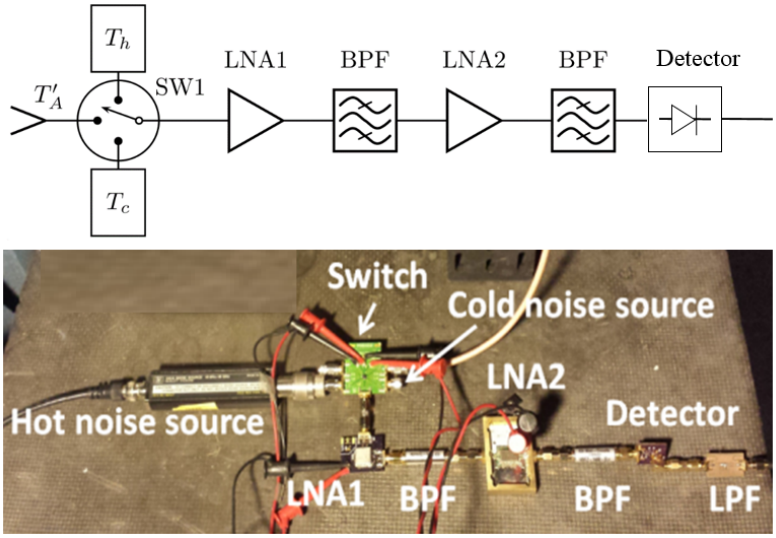

Figure 4.5: Block diagram of the 1.4 GHz radiometer along with the radiometer assembled from off-the-shelf components [36].

4.5 Hybrid PCB radiometer

Dicke power radiometer on a single pc board is manufactured from off-the-shelf surface-mount components, including a switch, two low-noise amplifiers (LNA), two bandpass filters, and a sensitive

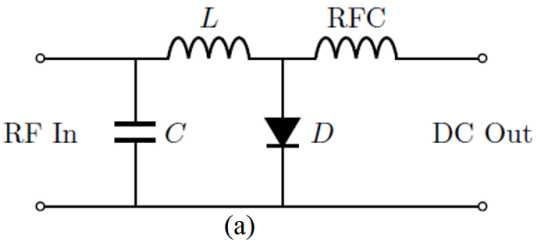

(a)

	Manufacturer	Part Number	Value
C	ATC	600L4R7CT	4.7 pF
L	Coilcraft	0402CS-15NX	15 nH
D	Skyworks	SMS7630-079LF	
RFC	Coilcraft	0603CS-R12X	120 nH

(b)

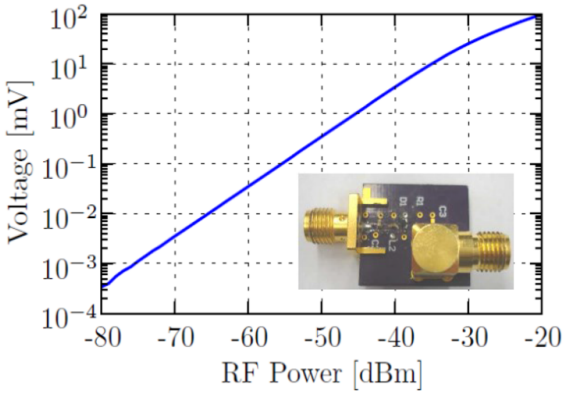

(c)

Figure 4.6: Detector (a) block diagram, (b) element manufacturers, part numbers and values, (c) linear output voltage versus input power shows that this detector works in the square-law region [49] and [36].

Table 4.2: Components of 1.4 GHz radiometer version 2

Component	G(dB)	NF(dB)	Part number	Manufacturer
SW_1	-0.55	0.55	SKY13388-465LF	Skyworks
LNA_1	35	0.6	Tamp-1521GLN+	Mini-Circuits
$BPF_{1/2}$	-4.14	4.14	SYBP-1420	Mini-Circuits
LNA_2	18.5	1.1	Ramp-33LN+	Mini-Circuits

diode detector, detailed in Fig.4.7. The size of the board is 8.2 cm×5 cm, and the components detailed in Table 4.2. The Dicke switch is a Hittite HMC345LP3 component with a noise figure of 2 dB and insertion loss of 2 dB. The LNA is implemented with two stages: the first stage is a MiniCircuits RAMP-33LN device with a noise figure of NF = 1 dB and gain of G = 16 dB, followed by a MiniCircuits VBFZ-1400 bandpass filter with a noise figure of 2 dB and insertion loss of 2 dB. This is followed by a second-stage LNA, which is a MiniCircuits TAMP component with NF = 0.6 dB and G = 32 dB, and a second bandpass filter. This board requires 5 V for LNA bias, and 3 V for control and bias of the switch and it consumes 140 mA.

To characterize this radiometer, the power level of a function generator at 1.4 GHz is varied

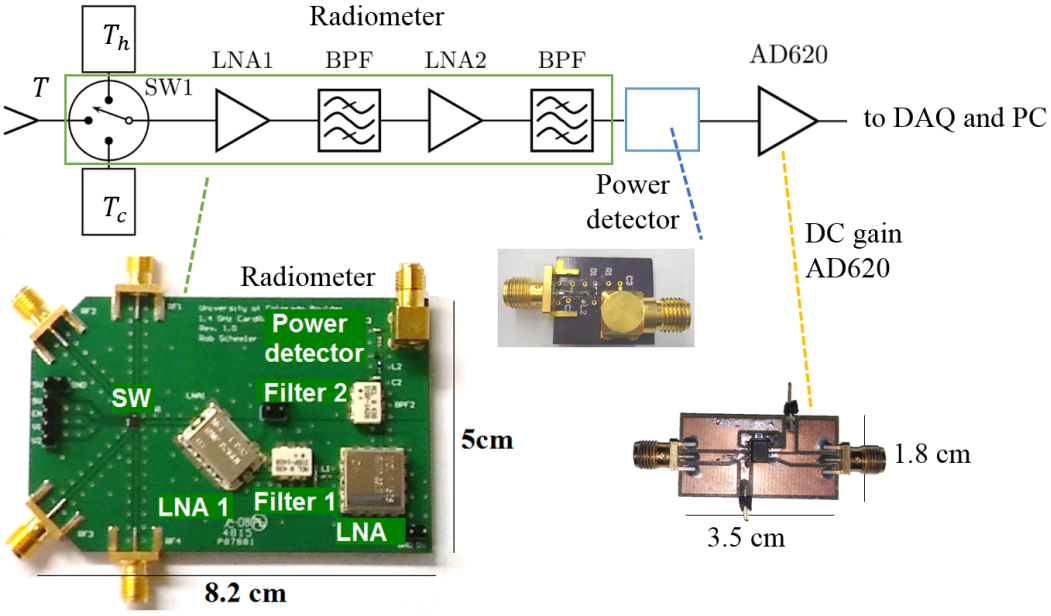

Figure 4.7: Dicke total power radiometer along with external power detector and dc gain stages: (top) block diagram, (bottom) fabricated components.

between -100 dBm and -60 dBm. The voltage responsively is shown in Figure 4.8-a showing that it is capable of detecting -100dBm of input power. To examine the frequency response, the function generator was set to sweep from 0.4-2.5 GHz (4.8-b). The frequency response is measured at 1.4 GHz at an input power of -70 dBm. Even though the radiometer cannot amplify the strong interference at 1.9 GHz, the bandwidth needs to be reduced to the 27 MHz to minimize interference. The output of the radiometer was measured to determine gain at different input frequencies. The measured gain and noise figure of the radiometer, using an HP 9870B noise figure meter, demonstrate a gain of 46.5 dB and a noise figure of 1.58 dB (Fig.4.8-c).

4.6 Integrated PCB narrow-band radiometer with improved stability

The noise figure and bandwidth of the radiometer play a significant role in determining the lowest received thermal power, corresponding to the smallest ΔT that can be detected. For a receiver, the minimum detectable signal (MDS) is directly proportional to the noise figure and inversely related to the gain of the radiometer as $MDS = FKTBG$ in which F is the system's

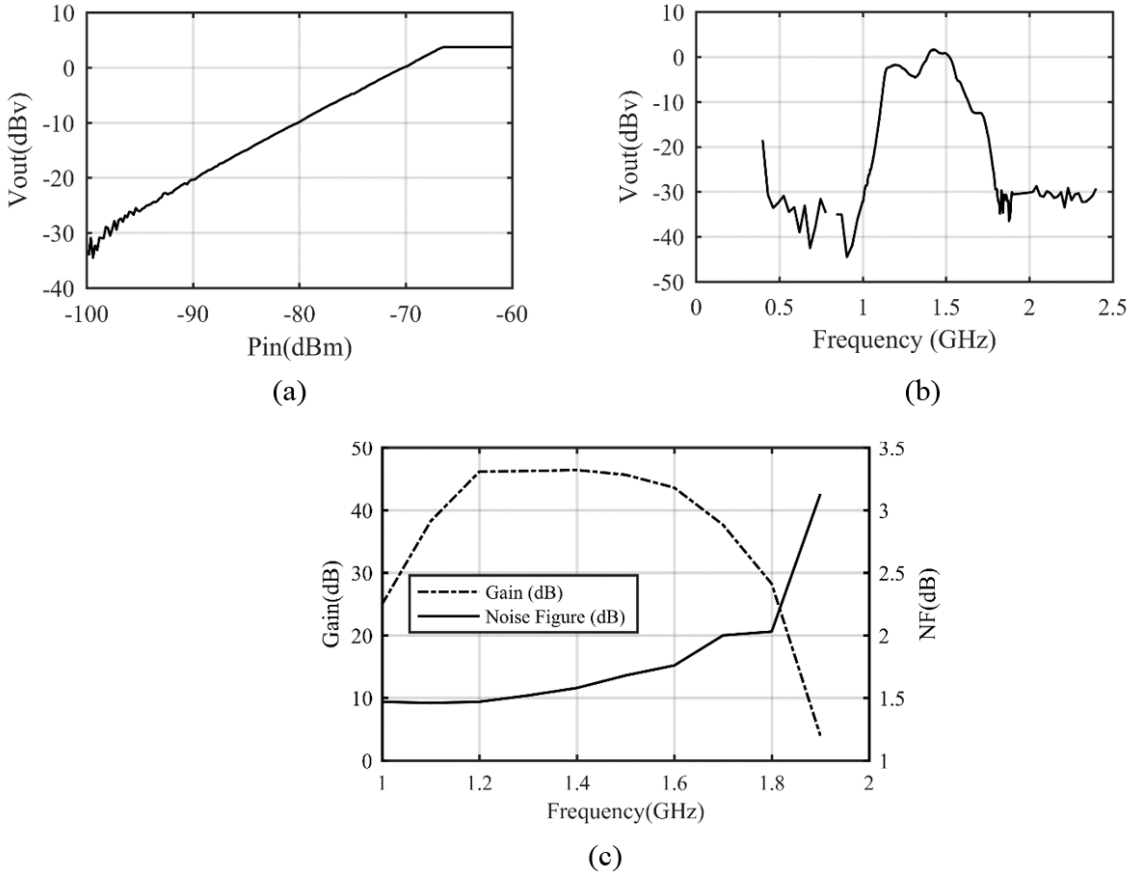

Figure 4.8: (a) Measured V_{out} as a function of P_{in} at 1.4 GHz. (b) The output voltage of the radiometer is recorded at an input power of -80 dBm when the input frequency is varied from 0.6 to 2.5 GHz. (c) The measured noise figure and gain of the radiometer over frequency.

noise factor, T is the noise temperature of the radiometer, B is the noise equivalent bandwidth, and G is the available gain of the radiometer. For RFI mitigation, the bandwidth of the system should be very narrow. Therefore, the noise figure and integration time τ play the important roles in improving minimum detectable signal and resolution of the radiometer (4.1). In the previous design a very low noise amplifier was used in the first stage. However, according to the Friis transmission formula for cascaded element, the switch dominates the noise figure of the chain. To reduce the noise figure of the radiometer, a low noise amplifier is added before the switch. However, the high overall gain in the RF stage can result in oscillations.

To solve the stability issue, a new radiometer with a simple 5-V supply is designed. At 5V,

Table 4.3: Components of 1.4 GHz radiometer version 3

Component	G(dB)	NF(dB)	Part number	Manufacturer
SW_1	-0.75	0.75	HMC241AQS16	Analog Devices
$LNA_{1/2/3}$	18.5	1.1	Ramp-33LN+	Mini-Circuits
$BPF_{1/2}$	-4.14	4.14	SYBP-1420	Mini-Circuits
Gat_1	-1.1	1.1	Gat-1+	Mini-Circuits
D-Sub connector			FCE17-E09PA-450	Amphenol Commercial Products
EMI/RFI Gasket			5747024-3	Mouser Electronics
Sheilding box			CFL3	Perancea

switch noise figure is higher than in the previous version. In order to maintain the radiometer noise figure below 3 dB, a low-loss high-dielectric constant substrate (Rogers 6010, $\epsilon_r = 10.2$) is used. EM simulations in AWR Axiem show that using a low-loss substrate reduces the passive circuit loss to 0.05 dB from 0.5 dB for FR4. Figure 4.9 shows the block diagram of the radiometer along with the fabricated board. It is implemented using the components are detailed in Table **??**. This radiometer requires 5 V bias and it consumes 163 mA to operate. The gain of this chain is 28 dB and the noise figure is 2.3 dB at operating frequency of 1.4 GHz, as illustrated in Figure 4.12. To improve the stability and immunity of the radiometer from low- and high-frequency interferences, several techniques are used, e.g., the radiometer is placed in a shielding box, proper filtering is applied at the bias lines, and the out-of-band impedance of the filters is defined by matched attenuators between the active and passive components.

Referring to Figure 4.9, some optimization are required to minimize complexity and thus improve stability. Adding grounded pads on the top of the substrate reduces capacitive coupling, but could change impedance. A full-wave EM study was performed for the dashed rectangle in Figure4.9, and the results are shown in Figure4.10 and Figure4.11. The conclusion is that for this substrate a minimum spacing $s = mm$ between the grounded pad and signal line is required to maintain match (Figure4.10). Figure4.11 shows the transmission coefficient as a function of frequency. Note the large number of metalized vias that ensure a good RF connection between the microstrip ground and top-layer shielding pads.

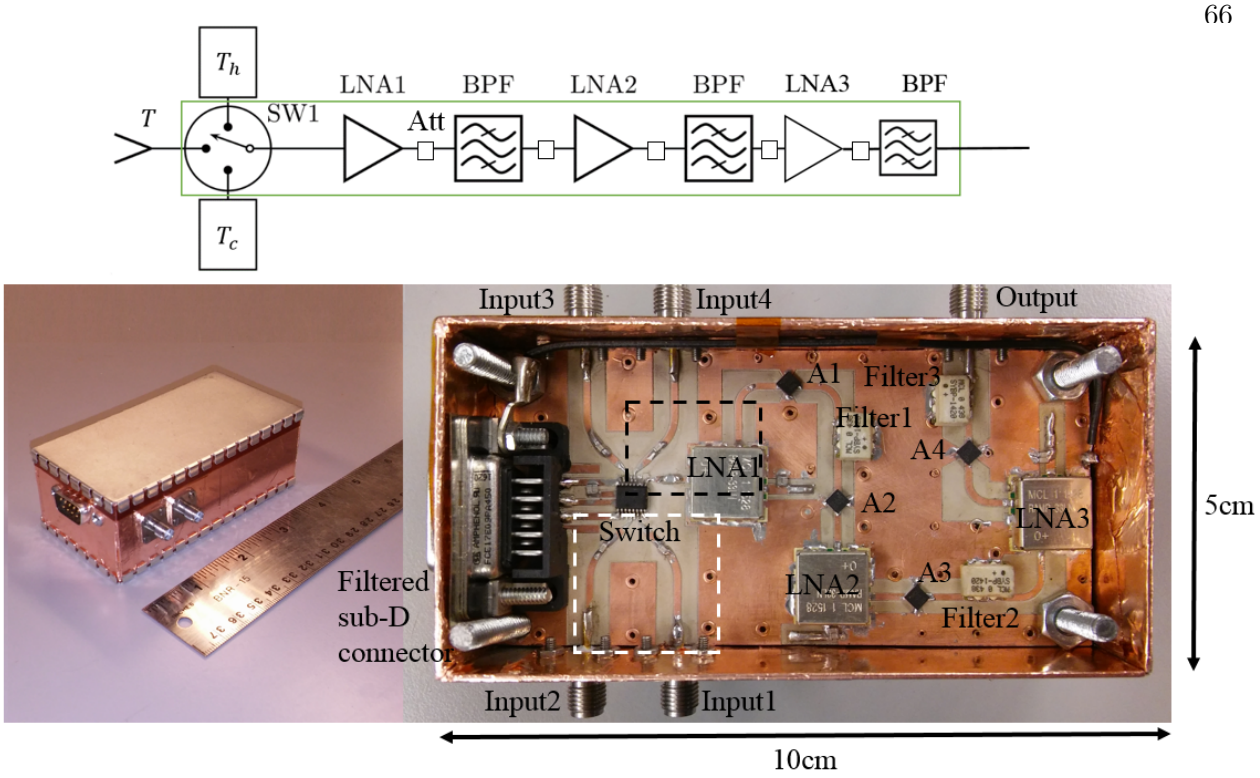

Figure 4.9: Radiometer block diagram along with the fabricated board: the radiometer is fabricated on low-loss Rogers6010 1.524 mm-thick substrate with ϵ_r=10.2. Filtered D-Sub connector reduces the low-frequency interference from the bias line. Low- and high- frequency filters are applied right at the bias pin of each LNA and the switch. Attenuator (A) between the low noise amplifier and filter defines the out of band impedance. A wire (shown in black) connects the connector ground to the RF box. A gasket fills the gap between the connector and the enclosure. The radiometer is placed in a fingered lid shielding box.

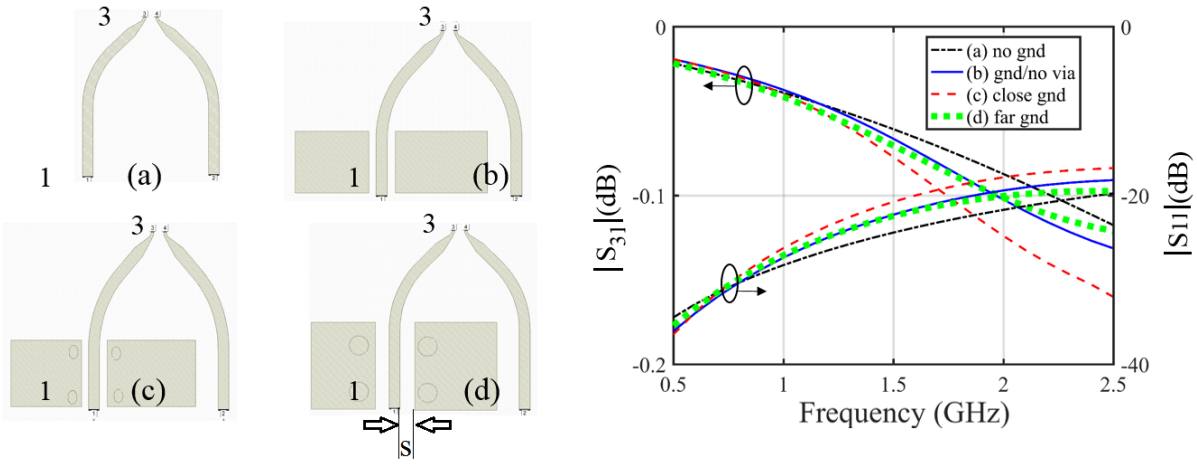

Figure 4.10: Investigating the top-layer ground spacing from microstrip transmission lines.

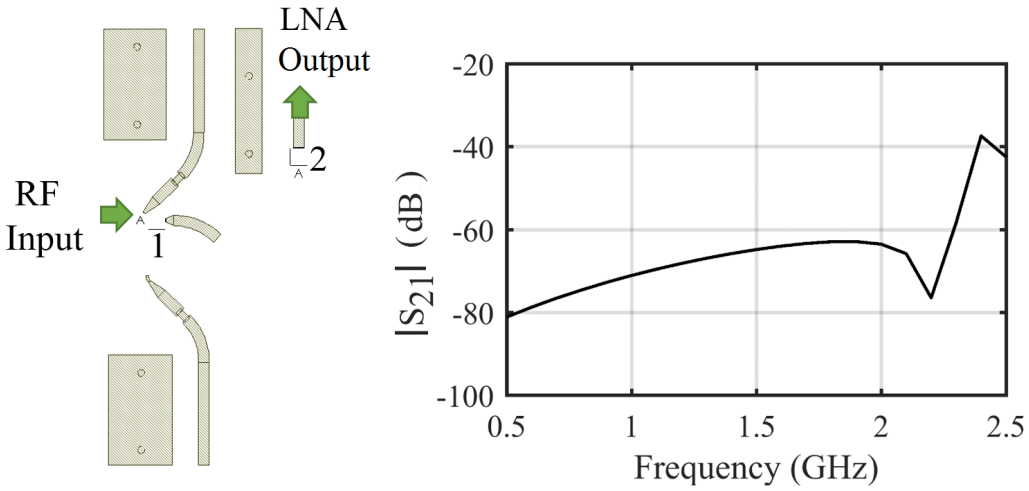

Figure 4.11: The coupling between input port next to the output port is investigated with a full-wave EM solver in AWR. Coupling better that -60 dB. is obtained, reducing the possibility of oscillation through feedback from output to the input.

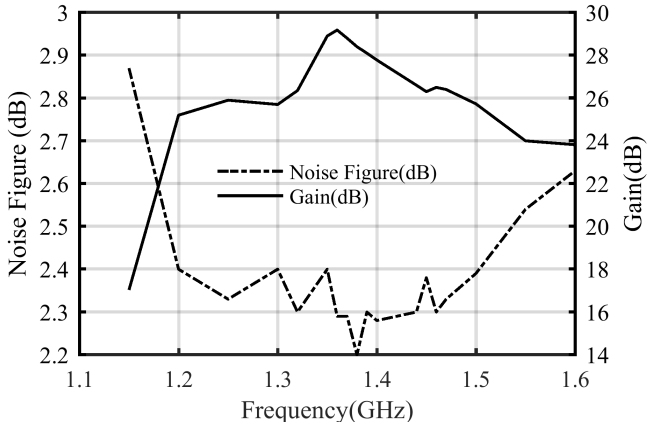

Figure 4.12: The noise figure and gain of the radiometer is measured by HP 8970B noise figure meter.

Most of the filters are naturally reflective out of band, and the amplifiers are not well matched out of their frequency band either. As illustrated in Figure 4.13, placing a 1-3 dB pi-pad network between the amplifier and the filter for defining out-of-band impedance, which is where it is most sensitive to interference, improves the interference immunity.

These pads can be 0 dB at the first run, and later they can be replaced by different values for determining the critical point for interference. Since no oscillation was observed, all attenuators

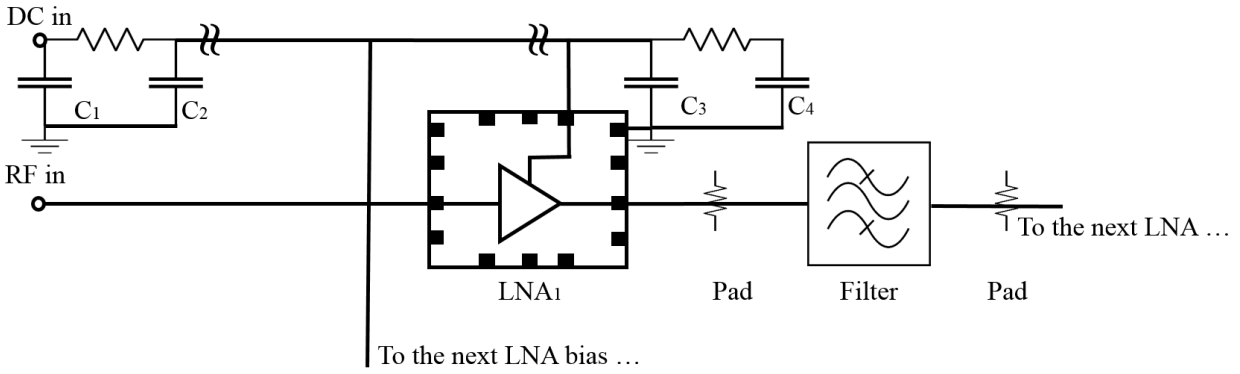

Figure 4.13: Adding a pi-pad attenuator between the amplifier and filter can define out-of-band impedance, reducing the reflection out of band and mitigating the RF interference. Adding series components (small valued resistors, ferrites) with shunt capacitors filters the supplies and the control ines and improve the immunity from RFI. C_1 (big capacitor) reduces low-frequency supply interference to the ground and C_2 (small capacitor) reduces high-frequency interference.

were kept at zero dB, evaluating the baseline for the main frequency and all interfering signals. If an instability occurs, the circuit provides an option for further stabilization by increasing the attenuation.

Adding series components (small valued resistors, ferrites) with shunt capacitors filters the supplies and the control lines and improve the immunity from RFI. As it is shown in Figure 4.13, at the bias input, a high value capacitor (C_1, e.g. 10uF, tantalum) shorts the low frequency supply interference to the ground. C_2 can be about 10pF, and R sets a pole a couple of decades below the interference frequency. An inductor ferrite targeted at the interference frequency can also be used instead of this resistor. At each of the IC supplies, capacitor at the pin (C_3) mitigates the effect of high frequency RFI. Using smallest capacitors at the pin (C_3), e.g. 10pF 0402, can lower the impedance between the pin and ground, reducing the susceptibility of the supply pin to the interference, and avoiding the leakage from the amplifier into the supply system (usually a 0402 capacitor will have about 0.4nH series inductance). The pi filter caps have to be below self-resonance to do their jobs as well. Multiple caps in parallel can cover a wider interference band. Finally, C_4

which can be a bigger capacitor, e.g. 100nF, helps with lower frequency interference mitigation [79]. A EMI/RFI gasket is also used for filling the space between connector and the box, providing a continuous RF ground. D-sub connector and gasket part numbers are presented in Table **??**.

Putting the whole board in a metal enclosure, significantly reduces the PCB exposure to radio frequency interferences, which can be picked up by traces on the board. The standard CFL3 can with a removable top fingered lid from Perancea Ltd, provides easy accessibility to the board top layer.

In order to access the bottom of the board, and provide a good ground connection, the bottom of the can was taken off and replaced by another fingered lid. Radiometer gain reduction was observed when the box was not well-soldered to the ground plane. For the sake of simplicity, the box was covered with copper foil, enabling easy connection between the box and ground. A wire also connects the ground of the dc bias to the RF ground as shown in Figure 4.9. Oscillation and modulation of input signal with possible signals out of the board is quite possible when the ground is not well connected to the enclosure (Figure 4.14). After proper grounding of the pcb, no oscillation were observed at the entire spectrum (Figure 4.15).

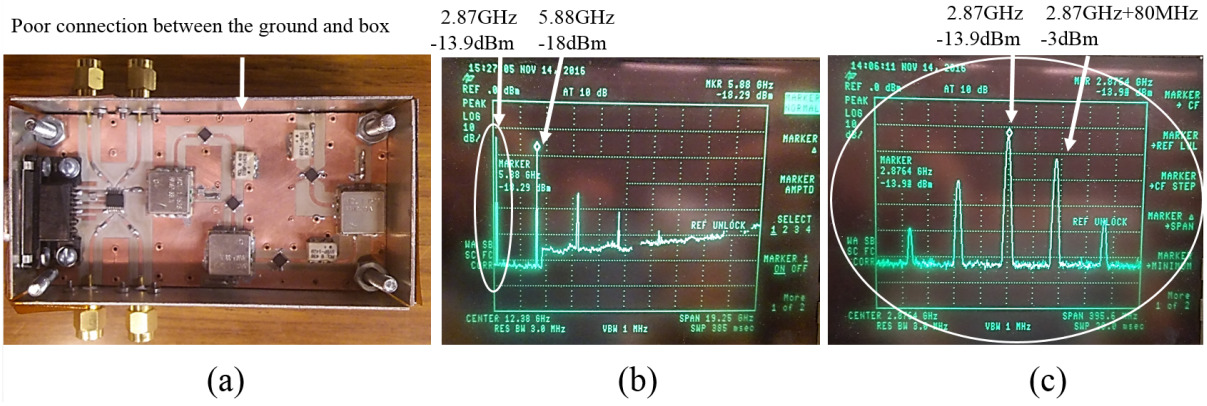

Figure 4.14: Effect of poor grounding: radiometer is tested with a source at 1.4 GHz at the input power of -80 dBm. The output is connected to a spectrum analyzer (a) radiometer placed in the shielding box: the box is not connected to the board and the lid is off (b-c) the input signal is mixed with an interference and strong oscillation and modulation at the input frequency and all its harmonics is observed.

In order to improve the immunity of the system to the interference, the system bandwidth

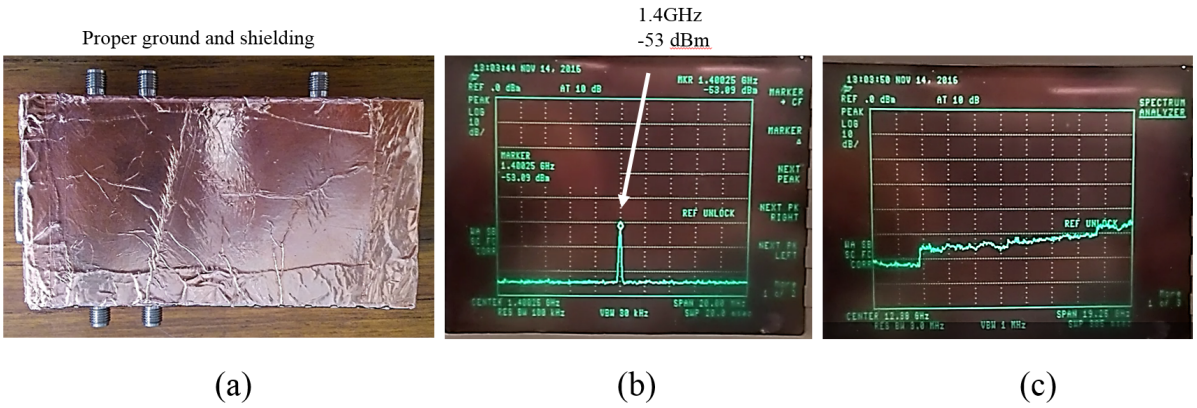

Figure 4.15: Effect of proper shielding: radiometer is tested with a source at 1.4 GHz at the input power of -80 dBm. The output is connected to a spectrum analyzer (a) the internal board is well grounded to the walls and lid is perfectly grounded to the board (b) gain of 28 dB is obtained at 1.4 GHz (c) no oscillation is observed at the entire spectrum.

should be limited to quiet frequency band of 1.4-1.427 GHz. Commercial filters at 1.4 GHz are neither miniaturized nor cheap. Another solution is to use a heterodyne architecture. In this approach, filtering and amplification are performed at lower frequency, at which it is easy and cheap to make amplifiers and channel-selection filtering with a reasonable Q, stability is more readily maintained, and lumped elements can be used and image frequency and spurs can be eliminated by mixers and filters.

To investigate the feasibly of a narrow band radiometer in RFI mitigation, a commercial software radio, USRP-2900 from NI, is used. This radio provides continuous RF coverage from 70 MHz -6 GHz. It has a direct conversion chip with adjustable 200 KHz-56 MHz bandwidth. The block diagram of this system is shown in Figure4.16, illustrating a chain of low noise amplifiers and filters in RF and IF bands as well as mixer with an adjustable LO. The resolution of ADC is 12 bits with the sample rate of 61.44 MS/s. The noise figure of the USRP is 2.5 dB and the gain is manually adjustable from 0 to 74 dB. All the RF components are contained in a AD9364BBCZ chip from Analog Devices.

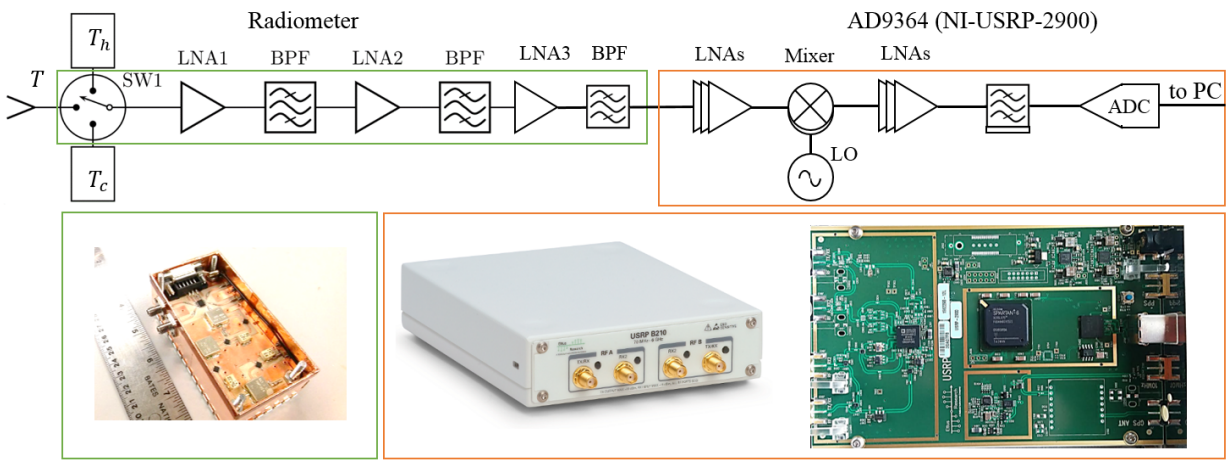

Figure 4.16: The block diagram of a narrow-band radiometer at 1.4 GHz.

4.7 Summary

This chapter presents the background on common microwave radiometer architecture, motivating the design used for the thermometer. The procedure for designing a sensitive, low noise, low gain drift, and stable radiometer is detailed. Three different 1.4-GHz radiometers are characterized: a "connectorized" radiometer assembled from off-the-shelf components (1); a hybrid printed-circuit board (PCB) radiometer (2); and a second iteration of the hybrid PCB radiometer with improved stability (3). The latter is fully characterized for noise figure, gain, and stability. The bandwidth of this stable radiometer is reduced to 27 MHz by means of a USRP-2900 software defined radio from National Instruments. Part of the contributions related to this chapter are included in [53] and [54].

Chapter 5

Measurement results

Contents

5.1 Overview

In this chapter, several measurements of multiple-layer tissue phantoms and *in-vivo* tests are performed to validate the concept of near-field microwave thermometry. First, the basic functionality of the connectorized radiometer is assessed with two different probes (folded-dipole and circular patch with superstrate) on a single-layer tissue phantom. Next, the hybrid version of the radiometer along with a miniaturized probe are used in estimating the temperature of a single-layer tissue phantom. The measurement is repeated with a narrow-band radiometer, validating the accurate performance of this radiometer in a congested RF environment. Initial measurements were performed on a single layer tissue phantom. The real challenge, however, is detecting the temperature

of a tissue layer which is not in direct contact with the probe. In the next measurement, the ability of the hybrid radiometer in detecting the temperature of a buried tissue layer under two- and three-layer phantom tissue stacks is evaluated, showing sufficient sensitivity to track temperature variations. RFI is also addressed by introducing a new probe for observing environmental RFI and applying an adaptive filtering algorithm. The operation of a single element and an array of probes is evaluated. For a realistic *invivo* measurement, the temperature of water inside the mouth is estimated from an external measurement on the cheek.

5.2 Homogeneous phantom temperature detection

The first set of measurements were performed with the connectorized version of the radiometer. Two different probes are tested for operation in the quiet 1.4 GHz band: a folded dipole [36] and a circular patch, Figure 5.1. The patch is backed by a ground plane which reduces interference and has a -15 dB return loss bandwidth of 20 MHz (%1.43) when placed on phantom tissue. The dipole has wider bandwidth 250 MHz (%17) and more susceptible to RFI. The dipole is fed by a tapered balun and fabricated on Rogers 4350B (ϵ_r=3.66) [36]. The patch is fabricated on a Rogers 6010 (ϵ_r=10.2) substrate with a superstrate of the same material. As explained in Chapter 3, the superstrate reduces the sensitivity of the probe to the surrounding media, which is advantageous for complex and variable tissue thicknesses in human bodies. The narrower bandwidth of the patch helps reduce RFI. The measured return loss of both probes (placed on the water bath) is better than 20 dB in the frequency band of interest.

A block diagram of the measurement setup is shown in Fig. 5.2. A probe is placed directly on the water and connected to the radiometer with external hot and cold noise sources. To allow the best resolution of the ADC, the output voltage is amplified with an added DC gain stage attached to the National Instruments PCI-6143 16-Bit, 250 kS/s/ch, simultaneous sampling multifunction data acquisition unit (DAQ). The output is displayed on the computer via a Python script. The hot reference is an Agilent 346A noise source with an Excess-Noise-Ratio of about 6 dB. The cold reference is a known 50 Ω SMA load at the room temperature. The power of hot noise source

Table 5.1: Summary of different measurements presented in this chapter. Probes, which are detailed in chapter 3, are labeled as follow (h): folded dipole, (b): circular patch with superstrate, (c): circular patch with superstrate and shorting-pin (SSP), (d): array of SSP. Radiometers, explained in detail in chapter 4, and are categorized as (1): connectorized radiometer, (2): hybrid PCB radiometer, (3): hybrid PCB radiometer with improved stability.

Meas.	Radiometer	Probe	Phantom	Goal
1	(1)	(h)	Tap water	Demonstrate functionality of the radiometer (1) and probe (h) in an anechoic chamber
2	(1)	(b)	Tap water	Demonstrate functionality of the radiometer (1) and probe (b) in an anechoic chamber
3	(2)	(c)	Tap water	Demonstrate functionality of the radiometer (2) and probe (c) in low-RFI environment
4	(3)	(c)	Tap water	Demonstrate functionality of the radiometer (3) and probe (c) in a non-shielded RFI environment
5	(2)	(c)	Salmon-Tap water	Demonstrate feasibility of sub-surface temperature detection
6	(2)	(c)	Salmon-Saline	Demonstrate better temperature estimation resolution by improving the tissue phantom model/Comparing the thermal conduction time constant with radiometer instantaneous response
7	(2)	(c)	Salmon-Rogers6010-Saline	Demonstrate feasibility of sub-surface muscle temperature detection under skin and fat layers
8	(2)	(c)	Salmon-Rohacell-Tap water	Demonstrate the presence of RFI in detecting temperature of burried muscle layer during long-term measurements
9	(2)	(c)	Tap water	Demonstrate functionality of RFI mitigation technique in long-term measurements
10	(2)	(c) and (d)	Agar-Rogers6006-Saline Agar-Rogers6006-Agar	Comparing the single element probe with the array probe in detecting muscle temperature under a thick layer of fat and skin
11	(2)	(c)	Cheek	Demonstrating sensitivity of the device in tracking water temperature inside the mouth from an external measurement on the cheek

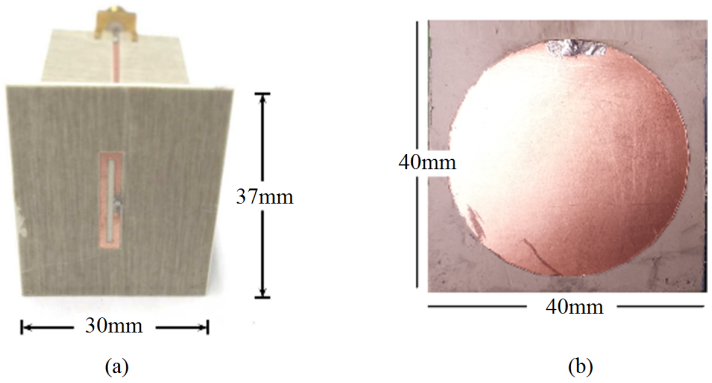

Figure 5.1: Two probes used for single-layer water measurements at 1.4GHz: (a) a printed folded dipole with a balun feed and (b) a circular patch used with a high-permittivity superstrate (the superstrate of probe (b) is not shown in the figure).

is reduced with a 3 dB attenuator for protecting the ADC. Separate thermocouples monitor the temperature logged by a Pico Technology tc-08 data logger unit. The computer controls the DC supply, the noise sources and the switch which operates at a 0.333 s switching period, inversly related to the achievable resolution, ΔT.

In the first set of experiments, the test setup is placed in an anechoic chamber to eliminate unknown interference. The two planar compact probe antennas are positioned on the surface of a half-space tap water phantom. The received data at the output of the detector, which is related to the unknown temperature measured by the probe, is then processed using equations presented in chapter 2 (Equations 2.20-2.26). Water is heated to 40°C when the patch is used [55], and to 35°C when the dipole probe is used [36]. The measured data in Fig. 5.4 compares the thermocouple measurements with passive radiometric measurements using the two probes. The estimated temperature from both probes follows the thermocouple measurement within 0.5 K as the water phantom cools to below 30°C in 55 minutes. Since the circular patch is narrower in band (20 MHz) compared to the folded dipole (250 MHz), the probe bandwidth is also calibrated out in temperature retrieval using the patch probe.

Next, the basic functionality of the hyrbid radiometer is assessed with a single-layer 5-cm deep tap water tissue phantom. The measurement setup is similar to the previous experiment except

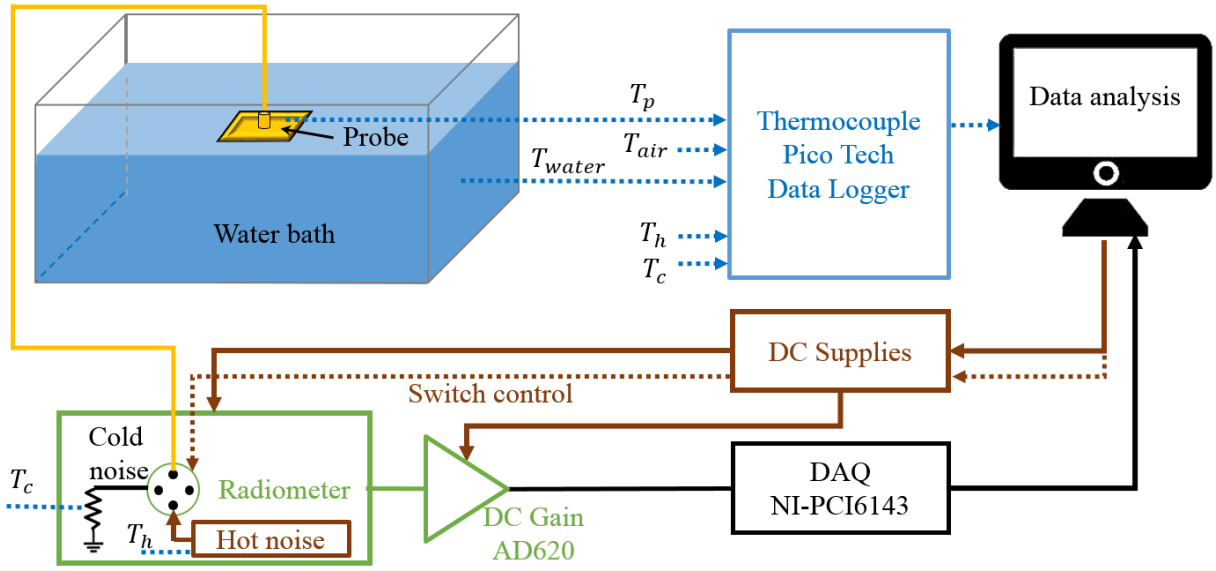

Figure 5.2: Block diagram of single-layer measurement setup showing a probe is placed directly on the water phantom and connected to the radiometer with external hot and cold noise sources. The output voltage is amplified with an added DC gain stage attached to the National Instruments PCI-6143 simultaneous sampling multifunction data acquisition unit (DAQ). The output is displayed on the computer via a Python script. The hot reference is an Agilent 346A noise source and the cold reference is a known 50 Ω SMA load at room temperature. Separate thermocouples monitor the temperature logged by a Pico Technology tc-08 data logger unit. The computer controls the DC supply which controls the noise sources and the switch.

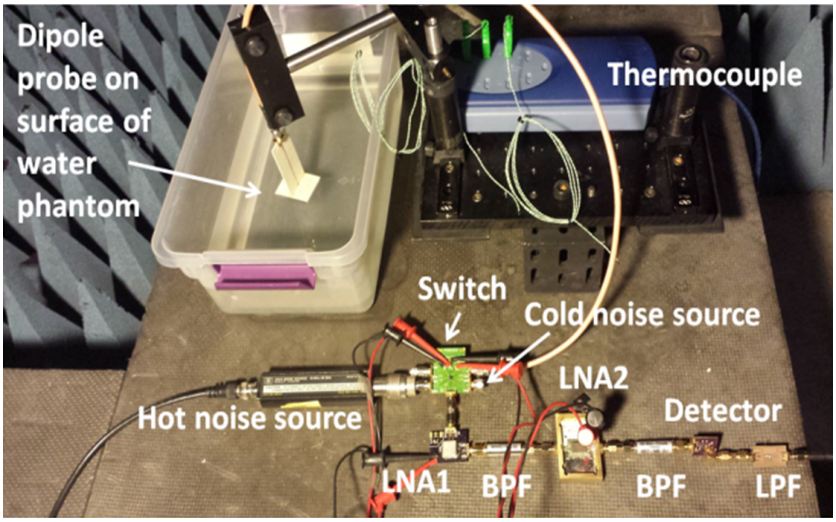

Figure 5.3: Photograph of the measurement setup of connectorized radiometer with the 1.4GHz folded dipole probe placed on the surface of the tap water phantom. The goal is to measure water temperature with the radiometer.

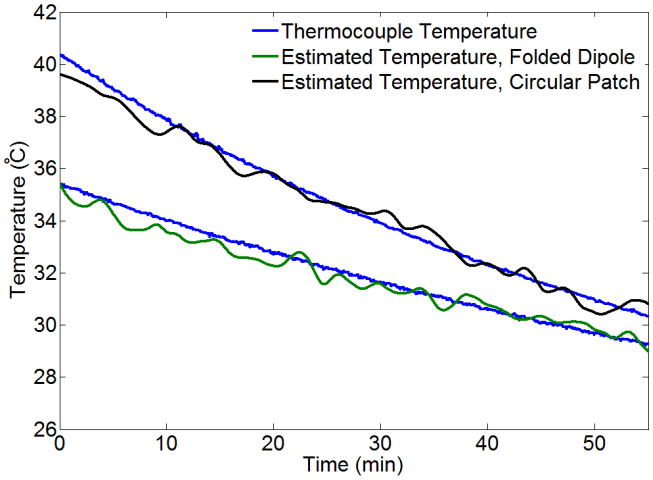

Figure 5.4: Calibrated radiometric estimate of direct simultaneous temperature of a tap water half-space using the 1.4 GHz connectorized radiometer compared to a thermocouple measurement. The water phantom is heated to 40°C for the patch probe data, and to 35°C for the dipole case, and measurements were taken as the water cooled until reaching 30°C. Both probes can track the temperature of the water with about 0.5°C of accuracy.

Table 5.2: Circular patch shorting-pin probe weighting functions on top of 5 cm of tap water.

Measurement	W_{Probe}	W_{Skin}
Single layer	0.360	0.640

that the water bag is placed on top of the probe as shown in Fig. 5.5. The water is heated to about 43°C and allowed to cool off over a period of 15 minutes. The estimate of the temperature at the radiometer plane is first corrected for the probe reflection coefficient (-15 dB), and a cable loss of 0.3 dB, using (2.23). To estimate the actual temperature of the water, (2.19) is solved with weighting functions determined by HFSS and listed in Table 5.2. The other half-space of the probe plane is assumed to be at room temperature. Data is taken in the basement of the engineering center that has thick reinforced concrete walls and therefore low RFI. The radiometric temperature estimate is filtered with a low-pass filter and the data is shown in Fig. 5.6 along with a simultaneous thermocouple measurement of the water. The plot quantifies the error between the radiometric and independent thermocouple measurement, which is at most 0.4°C.

As stated earlier, the hybrid radiometer suffers from occasional oscillations and relatively

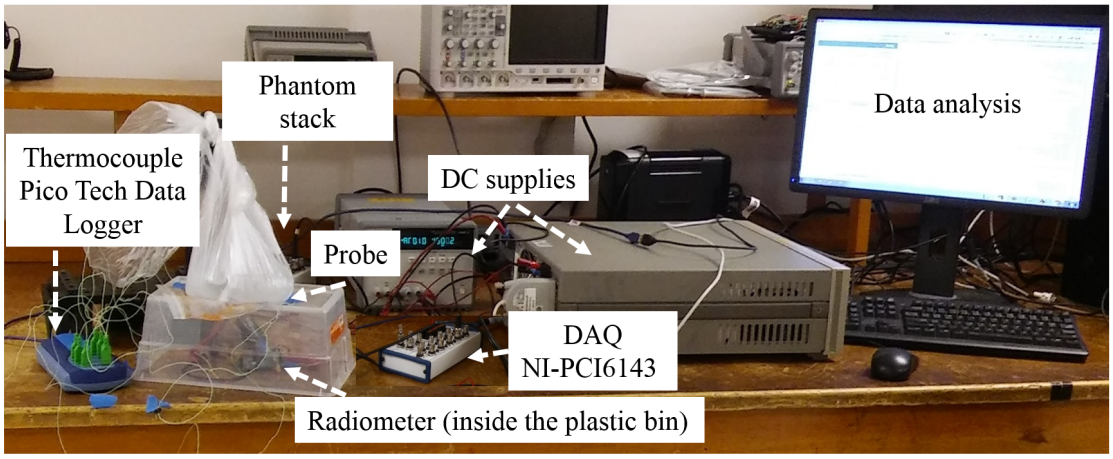

Figure 5.5: Photograph of the measurement setup of hybrid radiometer connected to a 1.4 GHz circular patch shorting-pin probe. The heated water bag is placed on top of the probe which is connected to the radiometer and DC gain block inside a plastic bin for ease of measurement. Data from the DAQ is analysed to estimate the unknown temperature of the water. The physical water temperature is measured by by thermocouple.

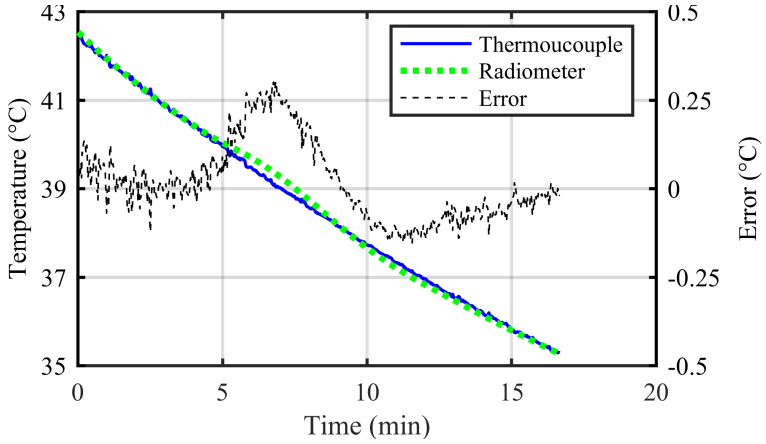

Figure 5.6: Measurement-based radiometric estimate of the temperature of a water half-space with hybrid radiometer and circular patch with shorting-pin and superstrate (green dotted line). The water phantom is heated to 42.5°C and measurements were taken as the water cooled until reaching 35°C. The error between the radiometric and thermocouple measurement is shown in dashed line and is between -0.15°C and 0.25°C.

wide bandwidth (500 MHz). A stable narrowband radiometer (1.4-1.427 GHz) is next developed and tested. In this experiment, the circular patch with shorting-pin and superstrate is placed in direct contact with the water. Unlike previous experiments, which were performed in a low-RFI environment or inside an anechoic chamber, this measurement is performed in a non-shielded RF

environment. The water is heated to 35°C and the measurement was taken over a period of 15 minutes. Fig. 5.7 shows an improved temperature accuracy of 0.2°C.

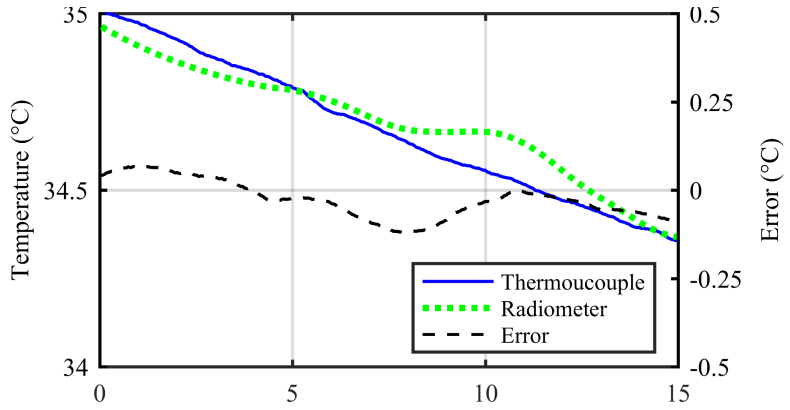

Figure 5.7: Measurement-based radiometric estimate of the temperature of a water half-space with narrow-band radiometer and circular patch with shorting-pin and superstrate. The water is heated to 35°C and measurement taken as the water cooled for 15 minutes in a non-shielded RF environment. Error between the radiometric and thermocouple measurement is shown in dashed line.

Even though narrow bandwidth reduces the temperature uncertainty due to RFI, unfiltered data obtained from the radiometer, Fig. 5.8, shows the presence of strong radio frequency interference in the quiet frequency band of 1.4-1.427 GHz. Applying a low-pass filter significantly reduces the error (as was shown in Fig. 5.7), but the RFI presence emphasises the need for further RFI mitigation. A step towards solving this problem is presented in section 5.5.

5.3 Buried layer temperature tracking in a two-layer tissue phantom

The previous experiments validate the operation of different probes and radiometers and the ability to measure single-layer temperature with a sub-degree accuracy. The real challenge, however, is to measure the temperature of a layer of tissue that is not directly in contact with the probe. For this validation, a 2-mm thick layer of smoked salmon is used as a skin phantom [48] and tap water or a saline solution is used as a muscle phantom. The experiment is described in Fig. 5.9. Two plastic bags filled with cold and hot muscle phantoms are cycled and placed on a 2 mm-thick skin phantom which is in direct contact with the probe. For this experiment, the circular patch with

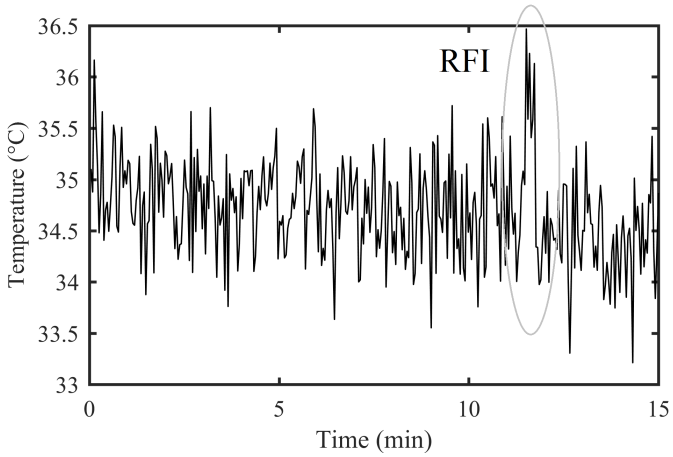

Figure 5.8: Radiometric unfiltered data taken from the narrow-band radiometer (1.4-1.427 GHz). The water phantom is heated to 35°C and measurement was taken with a circular patch with shorting-pin and superstrate as the water cooled for 15 minutes in RF environment. The temperature increase which appears about 12 sec into the measurement shows the presence of RFI in the "quiet" frequency band.

Table 5.3: Weighting functions of circular patch with shorting-pin and superstrate on the stack of skin and muscle phantoms at 1.4 GHz. Muscle phantom 1 is tap water and muscle phantom 2 is a 9ppt saline solution.

Measurement	W_{Probe}	W_{Skin}	W_{Muscle}
Single layer	0.360	0.640	
Two-layer, muscle 1	0.100	0.560	0.340
Two-layer, muscle 2	0.100	0.210	0.690

shorting-pin and superstrate is used since it can provide a good matching to these tissue stacks, as shown previously in Fig.3.6-c. The probe is connected to the radiometer which is switching between the probe and noise sources.

Two cases are presented in order to validate the effect of electrical conductivity of a buried tissue layer. The measured temperature tracking is shown in Fig. 5.10 as a plastic bag filled with DI water is cycled between 10°C and 79°C, while Fig. 5.11 shows the same measurement but with a saline solution cycled between 15°C and 30°C. In these experiments, the temperature of the salmon layer is kept almost constant by cycling the water bag faster than the salmon layer's thermal conduction time constant. The inverse problem is solved using the weighting functions listed in Table 5.3. The temperature of the skin layer is measured concurrently using a thermocouple.

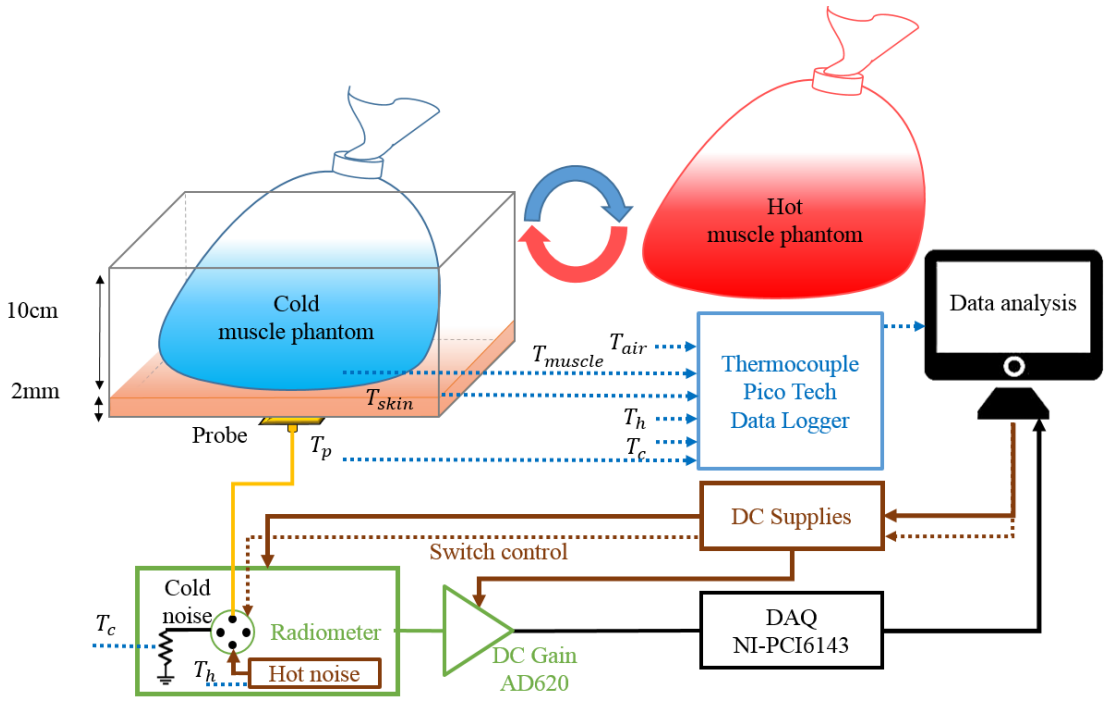

Figure 5.9: Block diagram of two-layer measurement setup. Two plastic bags filled with cold and hot muscle phantoms are periodically cycled and placed on a 2 mm-thick skin phantom. The goal is measuring the temperature of unknown muscle phantom with the radiometer probe in direct contact with the skin.

The main conclusions from the plots in Figs. 5.10 and 5.11 are: (1) the radiometer tracks the sub-surface temperature; (2) the thermal conduction is characterized by a much longer time constant, on the order of tens of seconds, while the radiometric measurement is practically instantaneous since it occurs at the speed of light through tissue; (3) the conductivity of the burried layer affects the measurement. Saline solution has a higher conductivity compared with tap water and it better models the electromagnetic properties of the muscle. Note that in Fig. 5.10 there is a slight temporal offset (2sec) between the radiometer and thermocouple data, due to the fact that the thermocouple was not in direct contact with the water phantom for this specific case. A thin piece of plastic bag was placed in between which results in a heat-conduction delay in temperature measurement. The estimated sub-surface temperature is affected by the conductive heating of the salmon layer, which is seen from the slope of the estimated temperature for the time periods of hot and cold water. This can be understood from the two-layer estimation expression

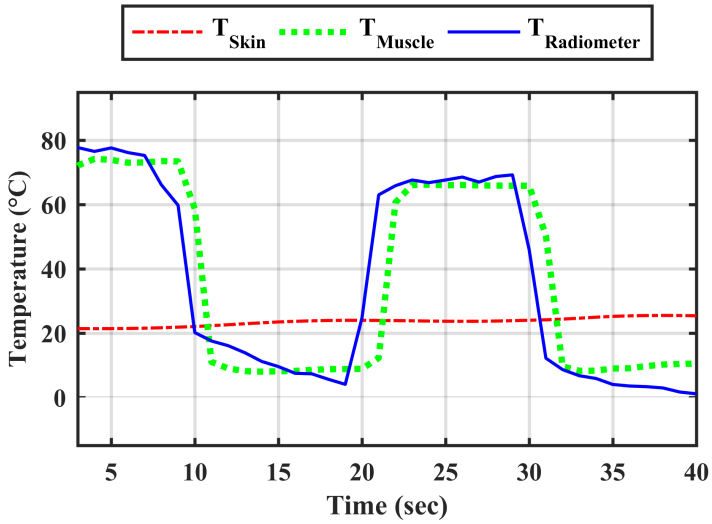

Figure 5.10: Sub-surface burried-layer temperature detection of skin-muscle phantom tissue stack. The temperature of the skin layer is kept constant. The muscle phantom bag is cycled faster than the thermal conduction time constant. There is a slight temporal offset (2 sec) between the radiometer and thermocoupled data, due to the fact that the thermocouple was not in direct contact with the tap water phantom and placed under the plastic bag for this specific case.

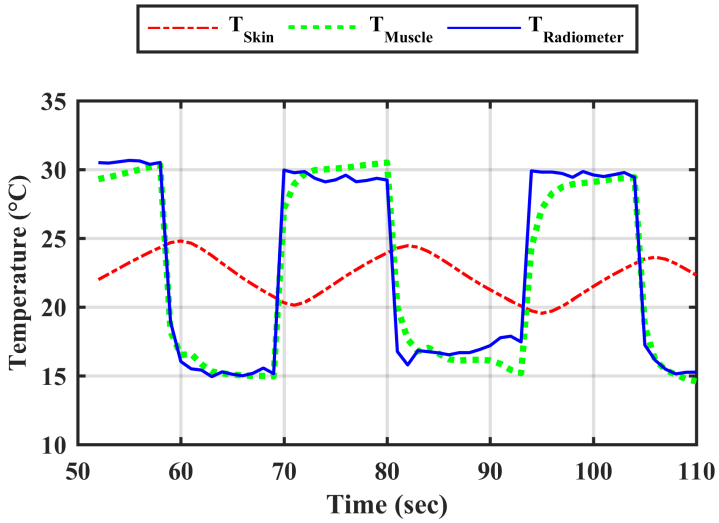

Figure 5.11: Sub-surface temperature detection of skin-muscle tissue stack. The muscle phantom bag is cycled faster than the thermal conduction time constant. Note that the thermal conduction is characterized by a much longer time constant, on the order of tens of seconds, while the radiometric measurement is practically instantaneous since it occurs at the speed of light through tissue.

$$T_{water} = \frac{T - T_{salmon}W_{salmon} - T_{probe}W_{probe}}{W_{water}}, \tag{5.1}$$

as T_{salmon} slowly increases due to conduction, the estimated water temperature decreases.

5.4 Buried layer temperature tracking in a three-layer tissue phantom

Increasing the number of layers to include a phantom layer of fat adds another term to the temperature estimation equations. To demonstrate this more complex case, a 1.28-mm thick layer of Rogers 6010 Duroid substrate is added between the salmon and bag of saline, representing a layer of fat. The block diagram of the experiment is illustrated in Fig. 5.12, showing two plastic bags filled with warm and cold muscle phantoms which are cycled on the fat and skin tissue phantoms. The probe (circular patch with shorting-pin and superstrate) is connected to the radiometer with external hot and cold noise sources. Similar to previous experiments, the output voltage is amplified with an added DC gain attached to the National Instruments PCI-6143 data acquisition unit (DAQ). Separate thermocouples monitor the temperatures logged by a PicoTech data unit and the computer controls the DC supply and the switch.

Using temprature retrieval explained in Chapter 2 and the weighting functions obtained from HFSS simulation in Table 5.4, data is calibrated and the results are plotted in Fig. 5.13. Again, the radiometer has sufficient sensitivity to track the temperature of muscle under two other layers.

To assess the long-term stability of the measurement, the DI water phantom was heated to 60°C and temperature measured as it cooled to 45°C over a 2.5-hour time period at room temperature, Fig. 5.14. In this experiment, the Duroid fat layer is replaced by a 3-mm layer of Rohacel foam. The discrepancy between the thermocouple and calibrated radiometric measurement increases after about 1.5 hours, resulting in an error as large as 5°C. This is attributed to RFI which increases the total power received by the radiometer. The next section describes a solution to mitigate RFI with a second probe.

5.5 RFI cancellation

Measuring low-power black-body radiation far from the peak of the Boltzmann curve becomes even more challenging due to man-made interference in the radio spectrum, e.g, cellular phones at

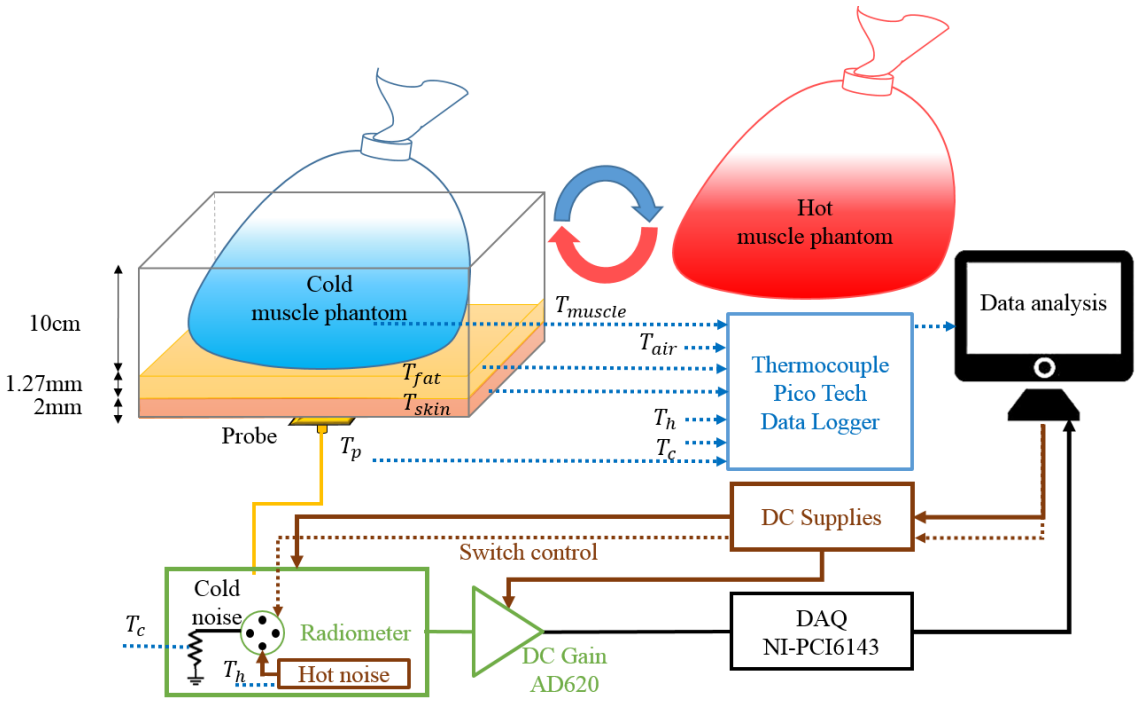

Figure 5.12: Block diagram of three-layer measurement setup showing a plastic bag is cycled between hot and cold muscle phantoms. The muscle phantom bag is placed on the fat and skin tissue phantoms. The probe is connected to the radiometer measurement setup. The goal is to measure the temperature of buried muscle phantom under the skin and fat tissue phantoms with the radiometer probe on the skin.

Table 5.4: Weighting functions of circular patch with shorting-pin and superstrate on the stack of skin, fat, and muscle phantoms at 1.4 GHz. Fat 1 refers to 1.27 mm-thick Rogers6010 substrate and fat 2 refers to 3 mm-thick Rohacell foam.

Measurement	W_{Probe}	W_{Skin}	W_{Fat}	W_{Muscle}
Three-layer, fat 1	0.101	0.633	0.025	0.241
Three-layer, fat 2	0.145	0.650	0.010	0.205

1.9 GHz and fluorescent lighting. As shown in Section 5.1, using a very narrow-band hybrid radiometer does not completely eliminate the radio frequency interference in a non-controlled environment. Miniaturization of the radiometer in a GaAs MMIC (switch, LNA and noise source), or fully silicon ICs, could improve RFI reception from the transmission lines and coaxial cables. Fig.5.15 shows an example measurement corrupted by RFI. In this experiment, the muscle phantom temperature is heated to about 35°C and measurements were taken for more than an hour. It is seen that RFI

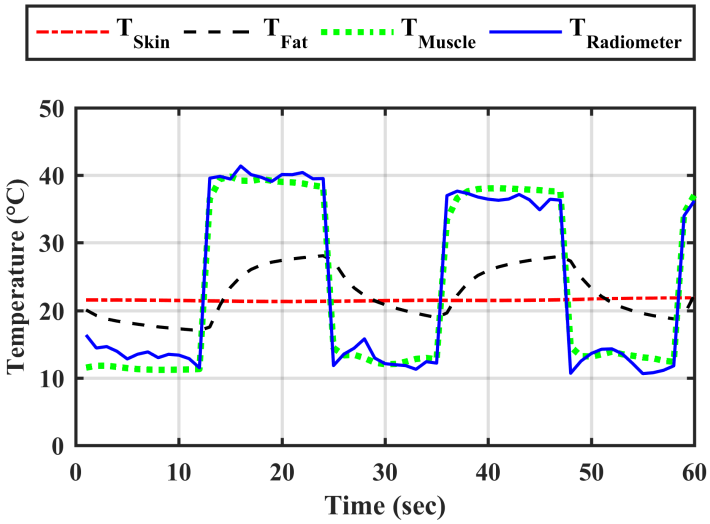

Figure 5.13: Sub-surface temperature detection of muscle under the skin-fat stack. The muscle tissue phantom in this case is a saline solution and is cycled on 1.27 cm of fat (Rogers 6010) and 2 mm of skin (salmon). The radiometer has sufficient sensitivity to track the temperature of muscle under two other layers.

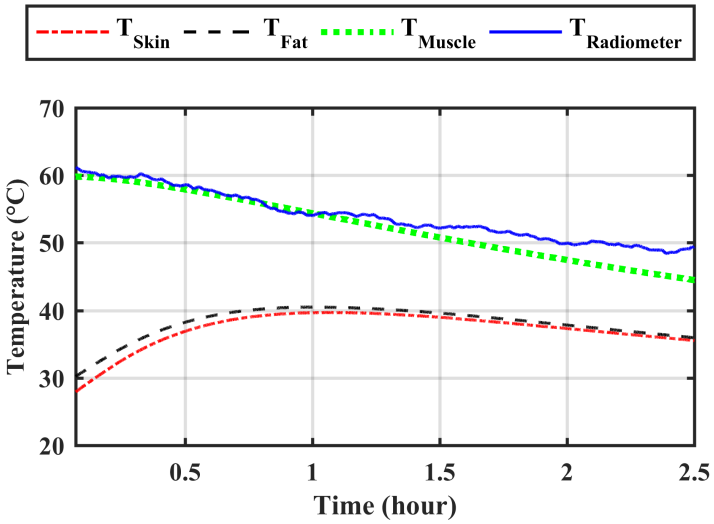

Figure 5.14: Sub-surface long-term temperature detection of skin-fat-muscle phantom stack. Radiometeric temperature of muscle (DI water) is compared with real temperature of the muscle under 3 mm of fat (Rohacel foam) and 2-mm layer of skin (smoked salmon) over a period of 2.5 hours. The temperature discrepancy is attributed to RFI which increases the total power received by the radiometer.

significantly degrades the ability of accurate temperature estimation from the muscle layer after 28

minutes.

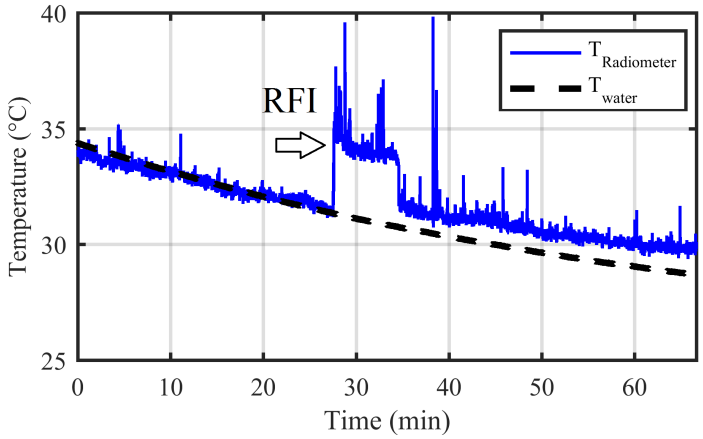

Figure 5.15: A three-layer measurement corrupted by RFI. Buried muscle (water phantom) under skin (salmon) and fat (Rohacell foam) measurements in the presence of RFI show larger errors in temperature estimation when external signals are received by the probe.

To examine the amount of RFI at 1.4 GHz in a RF congested environment, a wide-band log-periodic antenna was connected to a spectrum analyzer for continuously recording RFI at 1 MHz-2 GHz over a period of one day. The experiment shows random appearance of RFI at 1.4 GHz.

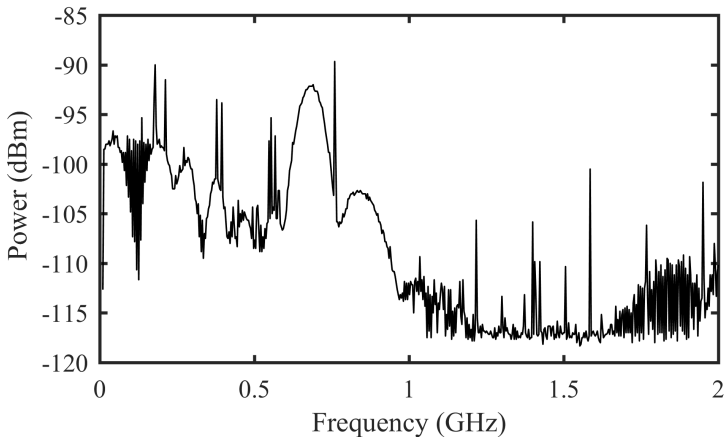

Figure 5.16: Measurement of RFI with a log-periodic antenna and a spectrum analyzer integrated over a period of 24 hours.

Besides using narrow-band or integrated radiometers, another approach for mitigating environmental radio frequency interference is tracking RFI with an additional probe, called RFI probe.

Fig. 5.17 shows the preliminary setup toward realization of an RFI detection system. The muscle phantom is placed on the probe while another probe is facing air and detecting RFI. The radiometer is switching between the hot and cold noise sources as well as the RFI probe and the main probe and continuously measuring RFI and thermal black-body radiation.

Next, the effects of radio frequency interference upon the signal measured by the radiometer can be modeled as a noise corrupted observation as shown in Fig. 5.18.

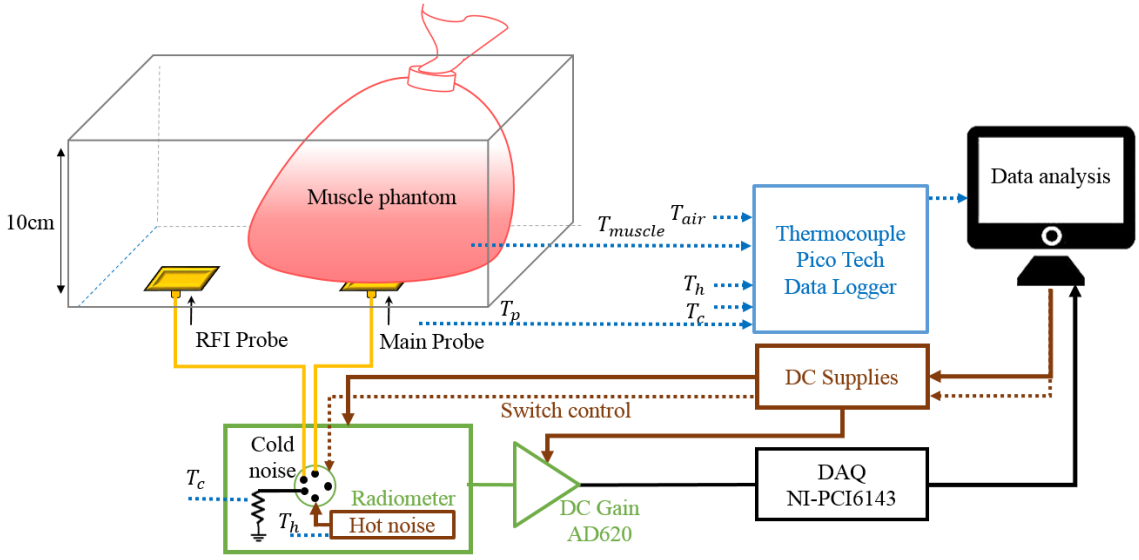

Figure 5.17: Block diagram of RFI detection setup. A plastic bag filled with the muscle phantom is placed on the probe (circular patch with shorting-pin and superstrate) which is connected to the radiometer setup. An additional probe (circular patch with superstrate) is tracking RF environmental interference. The radiometer is switching between the probes as well as as hot and cold noise references.

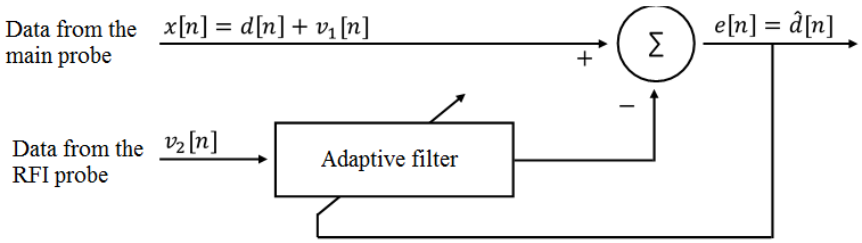

Figure 5.18: Block Diagram of Adaptive Noise Cancellation System.

$$x[n] = d[n] + v_1[n], \tag{5.2}$$

where $d[n]$ is the desired noise signal, $v_1[n]$ is radio frequency interference (RFI) and $x[n]$ is the measured total signal. The relative power of the RFI is often much greater than that of the black body radiation, but is attenuated through the tissues. Furthermore, information regarding the process underlying $v_1[n]$ is generally unknown, making it more difficult to separate the desired signal from the interference. To address this, an adaptive interference cancellation technique is applied. By utilizing a reference signal $v_2[n]$ that is correlated with $v_1[n]$, an estimate $\hat{d}[n]$ can be obtained by subtracting from $x[n]$ an estimate of the radio frequency interference, $\hat{v}_1[n]$

$$\hat{d}[n] = x[n] - \hat{v}_2[n] \tag{5.3}$$

In Fig.5.18, the RFI probe yields the signal $v_2[n]$ which is statistically correlated to $v_1[n]$ due to proximity. It is assumed that both $v_2[n]$ and $v_1[n]$ are uncorrelated to $d[n]$. $v_2[n]$ is adaptively filtered in order to produce an estimate of $v_1[n]$, $\hat{v}_1[n]$. This estimate is subtracted from $x[n]$, thus yielding an estimate of $d[n]$, $\hat{d}[n]$.

A recursive least squares (RLS) algorithm was used to generate the filter coefficients [52]. The goal of this algorithm is to minimize the weighted least squares error,

$$\epsilon = \sum_{i=1}^{n} \beta(n,i)|e(i)|^2, \tag{5.4}$$

where $e(i)$ is the difference between the desired signal, $d[n]$, and the estimated noise, $\hat{v}_1[n]$. The weighting factor, $\beta(n,i)$, is used to ensure that past data is forgotten in order to compensate for the nonstationary nature of the radio frequency interference. Therefore, the adaptive filter can follow the statistical variations of the observed data and extract an interference-free estimate of the radiometer signal. Fig. 5.19 illustrates the application of this method as applied to the measurement setup in Fig. 5.17. The muscle phantom is heated to 28°C and cooled off over one night. As seen in Fig. 5.19, the microwave radiometer data is corrupted by RFI. However, after applying the RFI

mitigation algorithm, the accuracy of estimated muscle temperature has significantly improved.

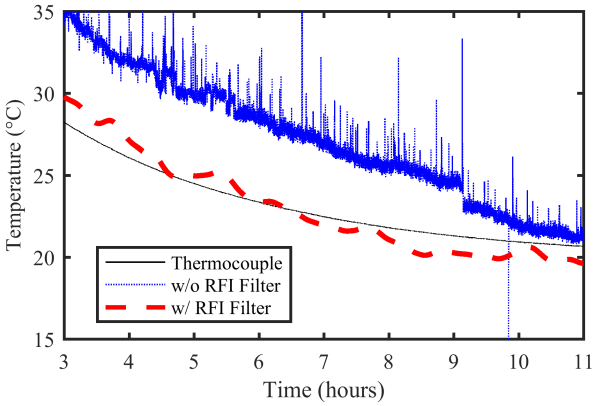

Figure 5.19: Single layer water temperature estimation using the setup from Fig. 5.17 with an additional probe and adaptive algorithm, compared with an uncorrected measurement over 11 hours. The direct thermocouple measurement is also shown as a baseline.

5.6 Comparing single element with an array of probes

As mentioned in the previous section, a patch with shorting-pin and superstrate can detect temperature variations of muscle under 2 mm of skin and 1.28 mm of fat. However, as shown in Chapter 2, increasing the thickness of fat reduces the black-body reception from the buried muscle layer. For the case of a thick fat layer, an array of probes provides better sensitivity.

To compare a single patch with shorting-pin and superstrate with an array of the same element, an experiment is performed as described in Fig. 5.20. Two plastic bags filled with cold and hot muscle phantom (saline) are cycled between 55°C and 25°C. The bags are placed on a 3.81 mm-thick Rogers6006 (representing fat), and 2 mm-thick Agar (representing skin). The agar recipe is provided in the Appendix A. Tissue phantoms are placed inside a transparent container which holds the single and array probes fixed in place. The array is connected to a power combiner, described in chapter 3, which adds up the received power from each array element. Both probes are in direct contact with the same tissue stack and are exposed to the same RFI. The radiometer continuously switches between the probes as well as the noise sources.

The raw radiometer voltage, Fig. 5.21-a shows that both single and array probes are capable

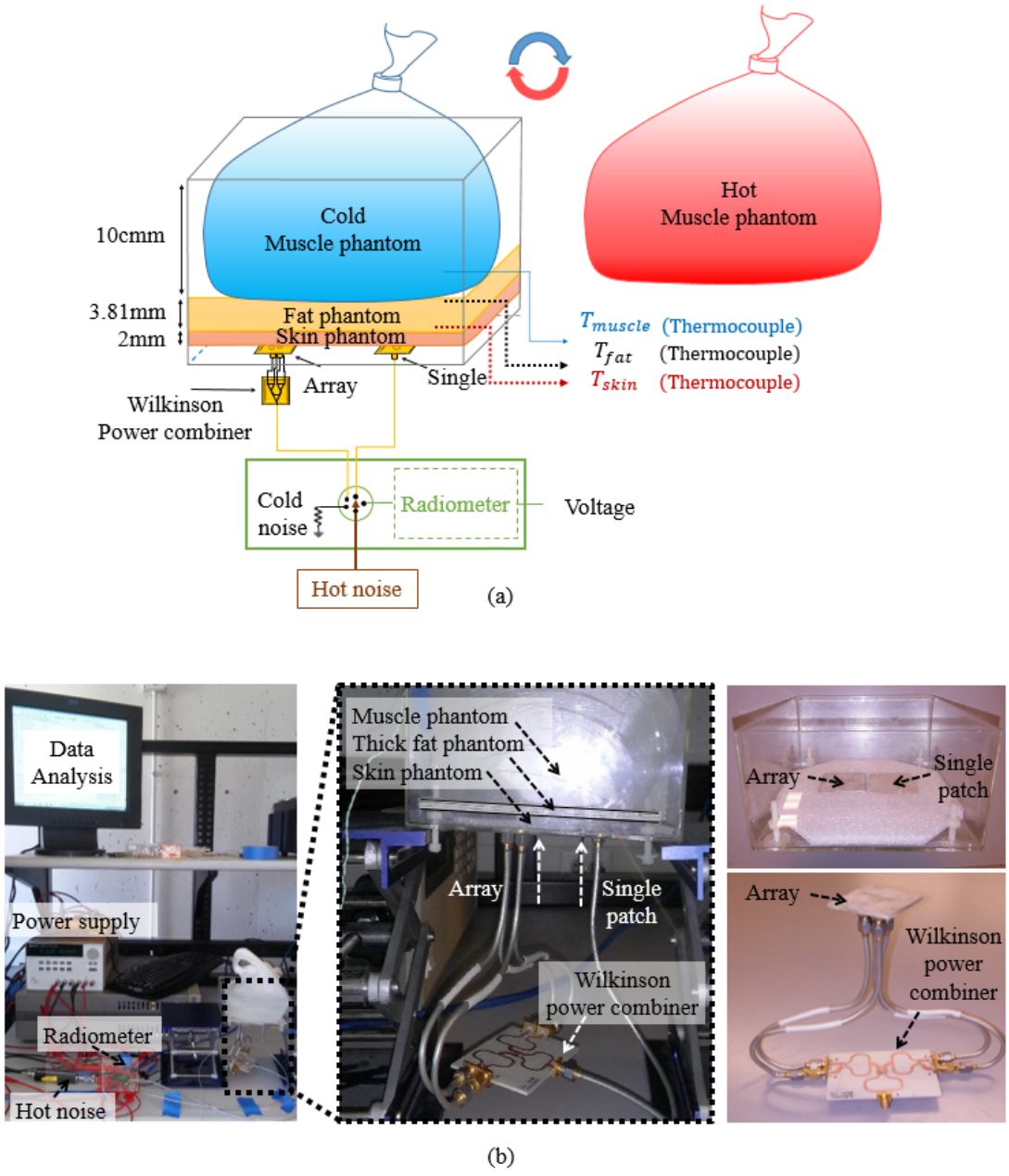

Figure 5.20: Comparing single patch and array probe in estimating muscle phantom temperature under a thick layer of fat and skin. Two plastic bags filled with cold and hot muscle phantom are cycled between 55°C and 25°C. The bags are placed on a 3.81 mm-thick fat, and 2 mm-thick skin. Tissue phantoms are placed inside a transparent container which holds the single and array probes fixed in place. The array is connected to a power combiner which adds up the received power from each array element. The radiometer continuously switches between the probes as well as noise sources.

of tracking high temperature variations in the muscle layer. However, two main differences are

observed (1) the output voltage of the array connected to the radiometer is higher than the single element. (2) voltage variations in the case of array is higher than single element. To evaluate this voltage differences, the temperature retrieval from Section (2.3) is used.

$$T_A = T_p W_{p,A} + T_s W_{s,A} + T_f W_{f,A} + T_m W_{m,A} \tag{5.5}$$

where T_A refers to array radiometric temperature, T, p, T_s, T_f, and T_m are probe, skin, fat, and muscle physical temperatures respectively. $W_{p,A}$, $W_{s,A}$, $W_{f,A}$, and $W_{m,A}$ are array probe, skin, fat, and muscle weighting functions respectively. Considering the efficiency of array probe as η_A we can calibrate array temperature as

$$T'_A = \eta_A T_A + (1 - \eta_A) T_p \tag{5.6}$$

The array temperature next should be calibrated due to loss in the power combiner, L_c,

$$T''_A = L_c T'_A + (L_c - 1) T_{rm} \tag{5.7}$$

The output voltage of the radiometer is directly proportional to calibrated array radiometric temperature, T''_A,

$$V_{Array} = k(T''_A + T_{rec})BG \tag{5.8}$$

where k is Boltzmann constant, and B, G, and T_{rec} are the bandwidth, gain, and the noise temperature of the radiometer. Since the skin temperature is constant and the fat weighting function and temperature variations in the fat layer are also very small, the voltage difference between the hot and cold muscle phantom can be written as

$$\Delta V_{Array} = V_{A_h} - V_{A_c} = kBG(T''_{A_h} - T''_{A_c}) = kBGL_c\eta_A W_{m,A}(T_{m,h} - T_{m,c}) \tag{5.9}$$

Note that this voltage difference does not depend upon the receiver noise temperature, or the room, and skin temperatures. Similarly for the single element $V_{Single} = k(T''_S + T_{rec})BG$, the

voltage difference between the hot and cold muscle phantom is equal to

$$\Delta V_{Single} = V_{S_h} - V_{S_c} = kBG(T''_{S_h} - T''_{S_c}) = kBG\eta_S W_{m,S}(T_{m,h} - T_{m,c}) \tag{5.10}$$

$T''_{S,h}$ refers to calibrated single probe radiometric temperature when the hot muscle bag is placed on the fat and skin. $T_{m,h}$ and $T_{m,c}$ are hot and cold muscle physical temperatures. $W_{m,S}$ is the weighting function of the muscle layer when measured with single element probe and the efficiency of single element probe is defined as η_S.

In this measurement setup, the measured return loss of both probes are almost the same as previously shown in (Fig.3.10). According to Fig. 5.21-a, temperature variations in the muscle results in higher voltage variation in the array compared with a single element ($\Delta V_{Array} > \Delta V_{Single}$). In other words, the combination of efficiency and muscle weighting function of the array is higher that a single element probe ($L_c\eta_A W_{m,A} > \eta_S W_{m,S}$) and array is receiving higher amount of power from the muscle compared with the single element.

In another experiment, the hot muscle (saline) bag is left on the tissue stack and allowed to slightly cool off over a period of 15 seconds. As seen in Fig. 5.21-b, compared to the single patch, the array exhibits a higher sensitivity to small temperature variations of the muscle under a thick layer of fat.

5.7 *In − vivo* measurement

As a preliminary step toward realization of a wearable device, the hybrid radiometer and patch with shorting-pin and superstrate were tested on different individuals. The goal is to observe the temperature variations of water within the oral cavity from the skin. In order to change the temperature, the volunteers were asked to hold cold, room and warm water temperatures in their mouth, Fig.5.22-a. A radiometer/probe placed on the cheek tracks the water temperature inside the mouth while a thermocouple measures the real water temperature. Radiometric readings observed over a time span of 180 sec are shown in Fig. 5.24 and shows that estimated temperature is highly

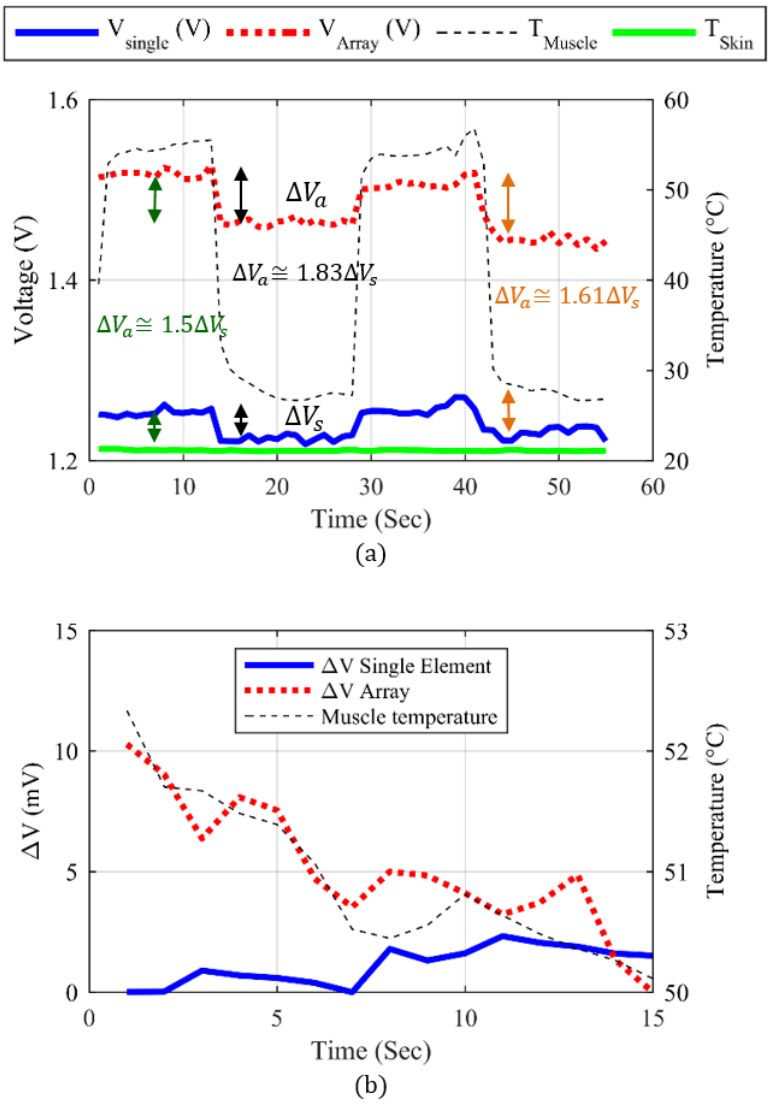

Figure 5.21: Temperature of the muscle (black line) has continuously changed and measured with a thermocouple. Temperature of skin (green line) is kept constant. (a) temperature variations in the muscle results in higher voltage variation in the array compared with a single element ($\Delta V_{Array} > \Delta V_{Single}$), i.e., the array can provide a better temperature resolution. (b) the hot muscle phantom is placed on the tissue stack and allowed to slightly cool off over a period of 15 seconds. Array shows a higher sensitivity to small temperature variations of the muscle under a thick layer of fat. Note that the raw voltage (gain) variations of the radiometer can be calibrated with the hot and cold noise sources.

correlated with in situ temperatures obtained by thermocouples. Human cheek model Fig.5.22-b ([26]), including 1.8 mm of average skin thickness, 4 mm of fat, and 2 mm of muscle, along with tissue electromagnetic properties from Table 1.1, were used to calculate the weighting functions in

HFSS.

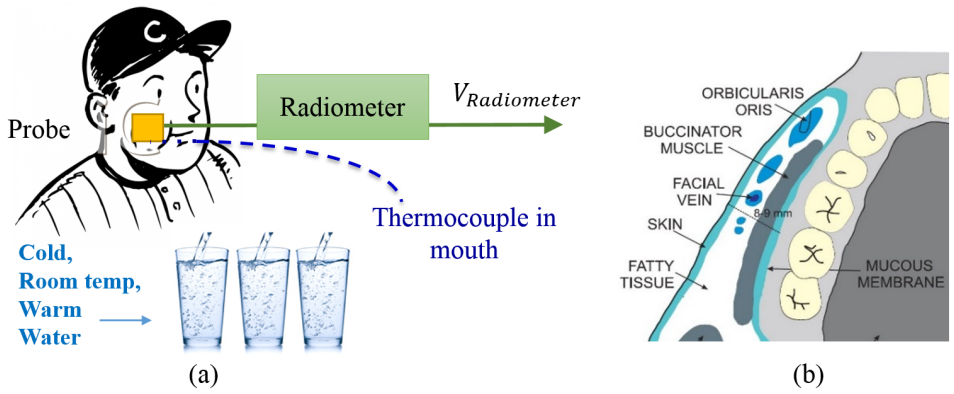

Figure 5.22: Estimating water temperature inside the mouth with the radiometer probe placed on the cheek. (a) Measurement of voltage at the radiometer output as a function of time when cold, room-temperature, and warm water are held in the mouth. (b) Human cheek model [26].

Fig.5.23 shows the raw voltage variation of the radiometer when two volunteers hold almost the same water temperatures in their mouth. As seen, the radiometer output voltage follows the water temperature. The measurement shows that even though the base line of voltage is different for different people, the voltage variations is about the same for both cases. The baseline voltage variation is due to the very narrow-bandwidth of the probe and small frequency shift which changes the baseline of the received voltage. Also, the volunteers performed the experiment slightly differently, e.g., probe placement, voltage of water in the cheek, etc.

Fig.5.24 shows the estimated temperature of the water from radiometer probe reading on the skin as it is compared with real temperature of the water in the mouth. The radiometer can instantly follow the temperature variations. The discrepancy from the real water temperature after few seconds is due to the fast variation of muscle tissue layer (water in the mouth), and thermal heat regulation of the human body. For example, when a volunteer drinks cold water, tissue layers are heating up to warm up the muscle layer, therefore, the radiometer starts reading a higher value which is actually due to temperature rise in the tissue layers. When the volunteer drinks warm water, the tissue starts cooling down, resulting in reducing the amount of black-body reception from the tissue layers. This effect can be calibrated by bio-heat thermal equation and predicting

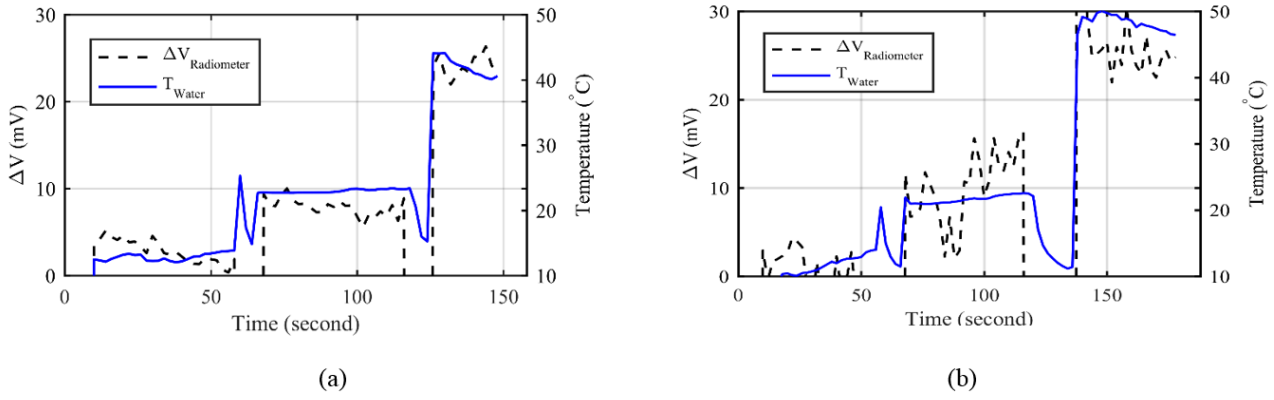

Figure 5.23: The radiometer output voltage variations when probe is placed on the cheek of two different volunteers. The voltage variations of the radiometer is linearly related to the temperature variations of the water.

the thermal behaviour during sudden temperature variations in the body.

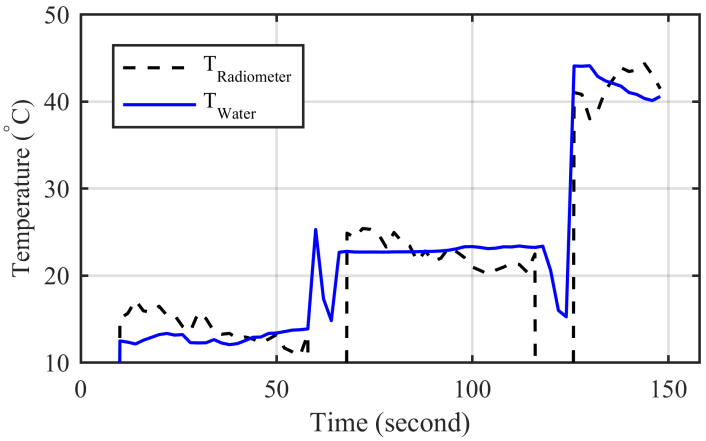

Figure 5.24: Estimating the temperature of water as a function of time when cold, room-temperature, and warm water are hold in the mouth with the radiometer probe placed on the cheek and a thermocouple inside the mouth for measuring real temperature of the water.

5.8 Summary

This chapter presents measurement results that validate the concept of near-field microwave thermometery. Several measurements of single and multilayer tissue phantoms are presented. First, the basic functionality of the connectorized radiometer (1) is assessed in an anechoic chamber. Next,

the hybrid version of the radiometer (2) along with a small probe is used to estimate the temperature of a single-layer tissue phantom in a RFI-controlled environment. The single layer measurement is repeated with a narrow-band stable radiometer (3) in a congested RF environment, validating the accurate performance of this radiometer. After validation on single-layer homogeneous phantoms, the performance of the hybrid radiometer (2) for detecting the temperature of a buried tissue under two- and three-layer tissue-phantom stacks is evaluated, showing enough radiometer sensitivity to track the temperature variations of a buried tissue layer under the stack of skin and fat layers. These contributions are reported in [53] and [50]. The operation of a single element probe and an array of the same probes in measuring the temperature of buried muscle tissue under a thick layer of skin and fat is evaluated. The various measurements also allow experimental comparison between different manufactured probes.

Finally, *in-vivo* measurements are performed on a human cheek where the internal mouth temperature is easily controlled and checked with a thermocouple. The results show that the radiometer and probe are capable of tracking water temperature inside the mouth, and are reported in [53], [50], and [51]. A technique for RFI mitigation, essential for making a long-term temperature monitoring device, is also presented in this chapter. A second probe is introduced for observing the environmental interference and an adaptive filtering algorithm is used to further mitigate the effect of RFI [52].

Chapter 6

Conclusion and future work

Contents

6.1 Summary and contributions

The presented research provides a path toward a portable instrument for noninvasive tracking of deep tissue temperature using microwave radiometry. Different aspects of near-field radiometry are addressed. Several human body tissue phantoms, mimicking electromagnetic properties of skin, fat, and muscle, are developed and presented in chapter 1. The temperature retrieval process is presented in chapter 2. It is shown that the near-field loading of tissue materials significantly affect the probe design. High dielectric constant contrast between skin, fat, and muscle suggests specific probe architectures, discussed in Chapter 3. Several probe architectures are investigated for maximizing the power reception from deep tissue layers and reducing the contribution of superficial tissue layers. Designs are cross-validated with two commercial software packages based on finite-element (HFSS) and finite-difference time domain (Sim4Life). Measurements with phantom tissue models are also shown to agree with the simulations. A stable, sensitive radiometer architecture at 1.4 GHz is presented in chapter 4. Three radiometers are characterized and the radiometer design and practical considerations for the latest version are explained in detail. Finally, several measurements on

human body tissue phantoms as well as human cheek validate the devices capability in measuring subsurface temperature changes. A summary of each chapter and related contributions are detailed below, and followed by a discussion of directions for future research.

Chapter 1 In this introductory chapter, microwave radiometery applications, existing core-body thermometers, and available microwave thermometers are overviewed. The disadvantages and advantages of previously demonstrated methods are presented as a motivation to the research of this thesis. Various solid and liquid tissue phantoms are discussed, since they are required for design and experimental validation. This chapter also reviews basic theory of black-body radiation as a foundation for microwave thermometry and introduces the challenges related to the design of a microwave thermometer, including frequency choice and sensitivity. The final device operating frequency range of 1.4-1.427 GHz is chosen since it is a quiet band allocated to radio astronomy and is less susceptible to radio frequency interference, while providing a few centimeters of sensing depth in tissues.

Chapter 2 discusses the the interaction of human tissue layers with a probe and calibration procedure for a microwave thermometer. A background on temperature retrieval methods from the literature is presented. Reciprocity between radiated and absorbed thermal noise power density in the near-field tissue layers is discussed and proven for a simple case. The measured radiometer temperature is formulated as the summation of contribution of each tissue layer times their physical temperature, and the required device calibration shown to be a function of the efficiency of the probe, cable loss, gain fluctuations of the radiometer device and probe bandwidth. Contributions related to this chapter are included in [53] and [54].

Chapter 3 details the probe design for human body microwave thermometry. The results from this chapter demonstrate an approach toward designing near-field probes, capable of detecting small temperature variations of deep tissue layers. Background information on previously published near-field probes is summarized. Decomposing the electric field into the normal and tangential components reveals important information on the design approach of the near-field probes loaded by the human body. High dielectric constant contrast between the skin, fat, and muscle tissue layers,

suggests using probes with dominant tangential component of electric field, such as patch and slot architectures. Also, it is shown that adding a layer of low-loss, low-dielectric constant superstrate can further reduce the contribution of superficial tissue layers in the received thermal noise.

Several near-field probes matched to a stack of skin, fat and muscle layers are designed, starting from a circular patch as a RFI-shielded planar design. A superstrate is then added to improve performance, and finally a shorting pin (inductive loading) is added to reduce the size of the patch. A 2×2 array of the miniaturized probe is then designed. A 1.4 GHz 4-1 power combiner was designed to combine the thermal noise received from all the probes. Several slot architectures are also examined on the same tissue stack. Superstrate slot architectures have higher bandwidth and receive a high amount of thermal noise from the muscle layer, making them more susceptible to RFI while patch structures have the advantage that the ground plane allows for easy integration with radiometer circuitry and also minimizes the amount of RFI.

The probes are designed through simulations with the commercial full-wave FEM simulator, HFSS, and volume power loss density in the tissue layers for different probes are compared. The most promising designs are validated either with a FDTD commercial code (Sim4Life) or with measurements. The near-field pattern of the circular patch with superstrate and shorting-pin is measured in the reciprocal (transmitting) mode using a temperature sensitive liquid crystal sheet placed inside a transparent phantom and heated by a power amplifier at 1.4 GHz.The effect of tissue thickness variations in temperature retrieval is analyzed, and finally probe placement on the sternum and forehead are discussed. Increasing the fat thickness has shown to reduce the overall received power by the probe. This issue which can be solved by using an array.

The contributions related to the content of this chapter are reported in in [70], [71], and [72].

Chapter 4 presents the background on common microwave radiometer architecture, motivating the design used for the thermometer. The procedure for designing a sensitive, low noise, low gain drift, and stable radiometer is detailed. Three different 1.4-GHz radiometers are characterized: a "connectorized" radiometer assembled from off-the-shelf components (1); a hybrid printed-circuit board (PCB) radiometer (2); and a second iteration of the hybrid PCB radiometer with improved

stability (3). The latter is fully characterized for noise figure, gain, and stability. The bandwidth of this stable radiometer is reduced to 27 MHz by means of a USRP-2900 software defined radio from National Instruments. Contributions related to this chapter are included in [53] and [54].

Chapter 5 presents measurement results that validate the concept of near-field microwave thermometery. Several measurements of single and multilayer tissue phantoms are presented. First, the basic functionality of the connectorized radiometer (1) is assessed in an anechoic chamber. Next, the hybrid version of the radiometer (2) along with a small probe is used to estimate the temperature of a single-layer tissue phantom in a RFI-controlled environment. The single layer measurement is repeated with a narrow-band stable radiometer (3) in a congested RF environment, validating the accurate performance of this radiometer. After validation on single-layer homogeneous phantoms, the performance of the hybrid radiometer (2) for detecting the temperature of a buried tissue under two- and three-layer tissue-phantom stacks is evaluated, showing enough radiometer sensitivity to track the temperature variations of a buried tissue layer under the stack of skin and fat layers. These contributions are reported in [53], and [50]. The operation of a single element probe and an array of the same probes in measuring the temperature of buried muscle tissue under a thick layer of skin and fat is evaluated. The various measurements also allow experimental comparison between different manufactured probes.

Finally, *in-vivo* measurements are performed on a human cheek where the internal mouth temperature is easily controlled and checked with a thermocouple. The results shows that the radiometer and probe are capable of tracking water temperature inside the mouth, and are reported in [53], [50], [51], [54], and [80]. A technique for RFI mitigation, essential for making a long-term temperature monitoring device, is also presented in this chapter. A second probe is introduced for observing the environmental interference and an adaptive filtering algorithm is used to further mitigate the effect of RFI [52].

6.2 Future work

The research presented in this thesis provides a path toward realization of a wearable microwave thermometer. Having shown the sensitivity of a skin-mounted portable device for tracking warm and cold water temperatures inside the human body (mouth), the next step is to implement a fully integrated wearable device. A chest/head strap with the device in touch with the sternum/forehead skin can enable heart/brain temperature estimations. Initial results in this direction are obtained with a non-calibrated radiometer and show tracking of water temperature in the mouth [51].

To implement a truly wearable device, miniaturization using several chips, and ultimately monolithic integration, is certainly possible. For example, the LNA, switch, detector, and hot noise source are all demonstrated as integrated circuits with excellent performance. The radiometer front end can be implemented in GaAs, while the back-end of the radiometer is amenable to standard complementary silicon processes, while Bi-CMOS RF silicon-germanium technology could be used for full chip integration. To accelerate the miniaturization process, commercialized "Global Positioning System (GPS)" receiver chips at 1.575 GHz can be used. These receivers are very low-noise which makes them highly sensitive to low input power ($\simeq -140dBm$). Their operating bandwidth can be adjusted to $\simeq 10$ MHz. Also, their small size makes them less susceptible to RFI. An additional Dicke switch, small hot noise source, and a few small temperature sensors are required for the full integration of the microwave thermometer. The operating frequency of the probe should be shifted to 1.575 GHz.

The eventual integrated IC(s) could be mounted and interconnected on a flexible substrate together with a probe. Although the rigid probes, which can be mounted on the skin with adhesive tape or straps, are essential in initial proof-of-concept experiments, a soft, conformal probe would eliminate possible air gaps between the probe and skin and improve the electromechanical coupling, thus reducing temperature estimating errors due to mismatch. A possible solution is to use a flexible/stretchable bio-compatible polydimethylsiloxane (PDMS) substrate which has recently found

many applications in electronics for health/wellness monitoring, disease diagnosis, and therapy [81].

A soft, conformal circular patch is designed on a flexible polymer (Polydimethylsiloxane - Sylgard 184 Silicone Elastomer). The dielectric constant of the PDMS at 1.4 GHz is estimated based on a copper-taped microstrip transmission line and two open-circuited stubs of different lengths sticking to this 2 mm-thick polyimide plate. The circular patch with superstrate and shorting-pin is chosen and the probe is simulated on the cheek (stack of skin, fat, muscle, and water layers). The design model and the mask design are shown in Figure 6.1. This probe is under fabrication in the Material Science department at University of Colorado Boulder.

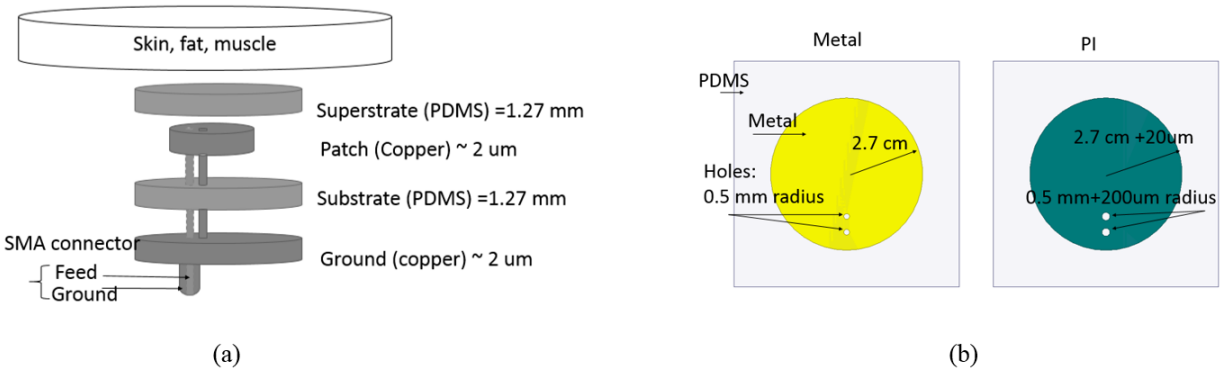

Figure 6.1: (a) Circular patch with superstrate and shorting-pin on flexible bio-compatible Polydimethylsiloxane (PDMS) substrate and superstrate, (b) Design mask of the metal and cover layers.

Improving the weighting functions, which relate the raw data and the core body temperature, is another important aspect of this project which is a subject of ongoing research. In this research the temperature of each tissue layer is assumed to be constant. In reality, however, the temperature of the human tissue varies at different depth of a single tissue. Temperature distribution models such as bioheat transfer equation can predict the temperature variation inside a tissue. The heat transfer in living tissue can be described using Pennes bio-heat equation. The model is based on energy exchange between the blood vessels and the surrounding tissues. According to this model, the total energy exchange by the flowing blood is related to the heat flow and temperature difference between the blood and the tissue

$$\rho C\frac{\partial T}{\partial t} = k(\frac{\partial^2 T}{\partial x^2} + \frac{\partial^2 T}{\partial y^2} + \frac{\partial^2 T}{\partial z^2}) + \omega_b C_b(T_b - T) + Q_m + Q_r(x, y, z, t) + \rho(SAR) \tag{6.1}$$

where T is temperature in °C, ρ is the tissue density Kg/m^3, C is the tissue specific heat J/Kg°C, ω_b, is the blood perfusion rate Kg/m^3s, C_b is the blood specific heat, T_a, the arterial-blood temperature, Q_m, the metabolic heat generation rate W/m^3, and Q_r, the regional heat sources W/m^3 and SAR is the specific absorption rate in case of electromagnetic field exposure.

For example, since the rate of temperature variation inside the body is slow, a 1-D temperature profile is sufficient to adequately model the observation [82], [83]:

$$T_z = \frac{T_{max}}{1 + \alpha(z - z_m) + \beta(z - z_m)^2} \tag{6.2}$$

This temperature profile is useful when the number of unknowns (temperature of tissue layers at different depths) is more than the number of radiometric measurements.

According to performed experiments in Section 5.6, compared with a single element probe, the array shows a better sensitivity to the small temperature variations of buried muscle layer under the thick layer of skin and fat. Considering thick layer of low dielectric constant materials (e.g. fat, cancellous and cortical bones, etc) between skin and core tissue layers, this improved performance can be very useful, especially in detecting heart temperature under the thick layers of sternum bones.

Considering Equations (5.9 and 5.10), the improved performance of the array compared with that of a single element probe, is due to combination of two factors: improved weighting function of the muscle layer ($WF_{m,A} > WF_{m,S}$) and improved radiation efficiency of the probe ($\eta_A > \eta_S$). The power combiner used in the measurements in Chapter 5, and described in Chapter 3, provides a phase distribution of $0, 0, 180$ and 180 ° between the array elements. According to the full-wave HFSS simulation, this phase assignment increases the weighting function in the muscle (WF_m) and reduces the skin weighting function (WF_s) as shown in Table 6.1.

According to this table, for an in-phase array, the power received from the muscle is about

Table 6.1: Weighting functions of skin and muscle layers under different phase distribution of the array elements. Results are obtained from HFSS simulation when array is placed on the stack of skin (Agar), Fat (Rogers6006), and Muscle (Agar).

$\Theta_1{}^\circ$	$\Theta_2{}^\circ$	$\Theta_3{}^\circ$	$\Theta_4{}^\circ$	WF_s	WF_m
0	0	0	0	0.625	0.344
0	0	45	45	0.421	0.561
0	0	90	90	0.285	0.705
0	0	135	135	0.234	0.759
0	0	180	180	0.224	0.770

half of the power received from the skin, which follows the same results for the single element probe. By increasing the phase difference between the array elements, the power dissipated in the core tissue layer increases. In analyzing the array in transmitting mode, this improvement is straightforward to explain – the transmitted electric fields from the array elements add up in phase in the muscle and destructively cancel out in the skin. However, in receiving mode and for black-body incoherent radiation reception, the effect of phase distribution should be further investigated. A similar experiment to the one in Section 5.6 can be preformed. By comparing the voltage difference of an array and single element under 0 and 180 degree phase shift, the effect of array phase distribution in power reception from the black body source can be evaluated.

6.3 Conclusion

In conclusion, this thesis presents proof-of-principle design, analysis and measurements of a microwave radiometer for measuring and tracking temperature of sub-surface tissue layers. The research advances the knowledge and state-of-the-art compared to previous reported work in the areas of: (1) near field probe design for specific tissue layers; (2) radiometer design; (3) temperature estimation algorithms; and (4) RFI mitigation. The contributions are reported in references [49], [50], [51], [52], [55], [54], [72], [70], and in [53], [71] which have been submitted for publication. Directions for ongoing and future work are discussed in the areas of probe design and radiometer miniaturization towards a wearable long-term monitoring thermometer device.

Bibliography

[1] Y. Eshraghi, V. Nasr, I. Parra-Sanchez, A. Van Duren, M. Botham, T. Santoscoy, and D. I. Sessler. An evaluation of a zero-heat-flux cutaneous thermometer in cardiac surgical patients. Anesth. Analg., 119(3):543–549, Sep 2014.

[2] Kurt Kräuchi, Christian Cajochen, Esther Werth, and Anna Wirz-Justice. Functional link between distal vasodilation and sleep-onset latency? American Journal of Physiology - Regulatory, Integrative and Comparative Physiology, 278(3):R741–R748, 2000.

[3] RTM Diagnostics. `http://www.iskinnewyork.com/understanding-your-skin/`.

[4] RTM Diagnostics. `http://www.zuniv.net/physiology/book/`.

[5] N. E. Rosenthal, A. A. Levendosky, R. G. Skwerer, J. R. Joseph-Vanderpool, K. A. Kelly, T. Hardin, S. Kasper, P. DellaBella, and T. A. Wehr. Effects of light treatment on core body temperature in seasonal affective disorder. Biol. Psychiatry, 27(1):39–50, Jan 1990.

[6] J E Gale, H I Cox, J Qian, G. D. Block, C. S. Colwell, and A. V. Matveyenko. Disruption of circadian rhythms accelerates development of diabetes through pancreatic beta-cell loss and dysfunction. Journal of Biological Rhythms, 26(5), 2011.

[7] Darwin Jeyaraj and et. al. Circadian rhythms govern cardiac repolarization and arrhythmogenesis. Nature, 483(7387), 2012.

[8] Allyson S. Howe and Barry P. Boden. Heat-related illness in athletes. The American Journal of Sports Medicine, 35(8):1384–1395, 2007.

[9] K. Carr. Microwave radiometry: its importance to the detection of cancer. 37(12):1862–1869, December 1989.

[10] A. E. Hamwey . Shaeffer, A. M. El-Mahdi and K. L. Carr. Detection of extravasation of antineoplastic drugs by microwave radiometry. 31(3):285–291, June 1986.

[11] S. Jacobsen and P. Stauffer. Multifrequency radiometric determination of temperature profiles in a lossy homogeneous phantom using a dual-mode antenna with integral water bolus. 50(7):1737–1746, 2002.

[12] Shizuo Mizushina, Minoru Matsuda, Katsuya Matsui, Yoshinori Hamamura, and Toshifumi Sugiura. Non-invasive temperature profiling using multi-frequency microwave radiometry in the presence of water-filled bolus. IEICE Transactions on Electronics, 74(5):1293–1302, 1991.

[13] J. W. Hand et. al. Monitoring of deep brain temperature in infants using multi-frequency microwave radiometry and thermal modelling. Physics in Medicine and Biology, 46(7):1885–1903, 2001.

[14] DS. Moran and L. Mendal. Core temperature measurement: methods and current. Phys. Med. Biol., 53(14), 2008.

[15] Christopher Byrne and Chin Leong Lim. The ingestible telemetric body core temperature sensor: a review of validity and exercise applications. British Journal of Sports Medicine, 41(3):126–133, 2007.

[16] G. Liu et al. Non-invasive temperature mapping using temperature-responsive water saturation shift referencing (t-wassr) mri. NMR Biomedicine, March 2014.

[17] Philipp Bruners, Elena Levit, Tobias Penzkofer, Peter Isfort, Christina Ocklenburg, Bernhardt Schmidt, Thomas Schmitz-Rode, Rolf W. Günther, and Andreas H. Mahnken. Multi-slice computed tomography: A tool for non-invasive temperature measurement? International Journal of Hyperthermia, 26(4):359–365, 2010.

[18] Bryan Ranger et al. Breast ultrasound tomography versus mri for clinical display of anatomy and tumor rendering: Preliminary results. American Journal of Roentgenology, pages 233–239, 2012.

[19] Guyton A and Hall J. Textbook of medical physiology, pages 159–178, 251–257. Artech House, Boston, London, 2000.

[20] B. M. Oliver. Thermal and quantum noise. Proceedings of the IEEE, 53(5):436–454, May 1965.

[21] A. E. Siegman. Thermal noise in microwave systems, part 1 fundumentals. The microwave journal, pages 81–90, March 1961.

[22] A. E. Siegman. Microwave Solidstate Masers. McGRAW HILL, 1964.

[23] K. Maruyma, S. Mizushina, T. Sugiura, G. M. J. Van Leeuwen, J. W. Hand, G. Marrocco, F. Bardati, A. D. Edwards, D. Azzopardi, and D. Land. Feasibility of noninvasive measurement of deep brain temperature in newborn infants by multifrequency microwave radiometry. IEEE Transactions on Microwave Theory and Techniques, 48(11):2141–2147, Nov 2000.

[24] Kiroyuki et. al. Multifrequency microwave radiometry for non-invasive thermometry using a new temperature profile model function. IEICE Transactions on Electronics, E78-C(8), 1995.

[25] Quenton Bonds. A Microwave Radiometer for Close Proximity Core Body Temperature Monitoring: Design, Development, and Experimentation. PhD dissertation, University of South Florida, 2010.

[26] Øystein Klemetsen, Svein Jacobsen, and Yngve Birkelund. Radiometric temperature reading of a hot ellipsoidal object inside the oral cavity by a shielded microwave antenna put flush to the cheek. Physics in Medicine and Biology, 57(9):2633, 2012.

[27] F. Bardati, V.J. Brown, and P. Tognolatti. Temperature reconstructions in a dielectric cylinder by multi-frequency microwave radiometry. Journal of Electromagnetic Waves and Applications, 7(11):1549–1571, 1993.

[28] MS Windows NT kernel description. http://web.archive.org/web/20080207010024/http://www.808multimedia.com/winnt/kernel.htm.

[29] I. S. Karanasiou, N. K. Uzunoglu, and C. C. Papageorgiou. Towards functional noninvasive imaging of excitable tissues inside the human body using focused microwave radiometry. IEEE Transactions on Microwave Theory and Techniques, 52(8):1898–1908, Aug 2004.

[30] K. D. Stephan, J. B. Mead, D. M. Pozar, L. Wang, and J. A. Pearce. A near field focused microstrip array for a radiometric temperature sensor. IEEE Transactions on Antennas and Propagation, 55(4):1199–1203, April 2007.

[31] C. T. Huynh, R. Devine, and M. R. Tofighi. An l-band microwave radiometer for subsurface temperature measurement. In Consumer Electronics (ISCE), 2012 IEEE 16th International Symposium on, pages 1–2, June 2012.

[32] M. R. Tofighi and C. T. Huynh. A microwave system for blood perfusion measurements of tissue; a preliminary study. In Biomedical Wireless Technologies, Networks, and Sensing Systems (BioWireleSS), 2013 IEEE Topical Conference on, pages 49–51, Jan 2013.

[33] M. R. Tofighi, J. R. Pardeshi, and B. A. Maicke. Microwave system and methods for combined heating and radiometric sensing for blood perfusion measurement of tissue. In 2016 IEEE MTT-S International Microwave Symposium (IMS), pages 1–4, May 2016.

[34] P. R. Stauffer, D. B. Rodriques, S. Salahi, E. Topsakal, T. R. Oliveira, A. Prakash, F. D'Isidoro, D. Reudink, B. W. Snow, and P. F. Maccarini. Stable Microwave Radiometry System for Long Term Monitoring of Deep Tissue Temperature. Proc SPIE Int Soc Opt Eng, 8584, Feb 2013.

[35] P. R. Stauffer, D. B. Rodriques, S. Salahi, E. Topsakal, T. R. Oliveira, A. Prakash, F. D'Isidoro, D. Reudink, B. W. Snow, and P. F. Maccarini. Stable Microwave Radiometry System for Long Term Monitoring of Deep Tissue Temperature. Proc SPIE Int Soc Opt Eng, 8584, Feb 2013.

[36] Robert Scheeler. A Microwave Radiometer for Internal Body Temperature Measurement. PhD dissertation, University of Colorado Boulder, 2013.

[37] D. B. Rodrigues, P. F. Maccarini, S. Salahi, T. R. Oliveira, P. J. S. Pereira, P. Limão-Vieira, B. W. Snow, D. Reudink, and P. R. Stauffer. Design and optimization of an ultra wideband and compact microwave antenna for radiometric monitoring of brain temperature. IEEE Transactions on Biomedical Engineering, 61(7):2154–2160, July 2014.

[38] C Gabriel, S Gabriel, and E Corthout. The dielectric properties of biological tissues: I. literature survey. Physics in Medicine and Biology, 41(11):2231, 1996.

[39] S Gabriel, R W Lau, and C Gabriel. The dielectric properties of biological tissues: Ii. measurements in the frequency range 10 hz to 20 ghz. Physics in Medicine and Biology, 41(11):2251, 1996.

[40] S Gabriel, R W Lau, and C Gabriel. The dielectric properties of biological tissues: Iii. parametric models for the dielectric spectrum of tissues. Physics in Medicine and Biology, 41(11):2271, 1996.

[41] Tissue Electromagnetic Properties ITALIAN NATIONAL RESEARCH COUNCIL. http://niremf.ifac.cnr.it/tissprop/,.

[42] Tissue Electromagnetic Properties. https://www.itis.ethz.ch/virtual-population/tissue-properties/database/tissue-frequency-chart/,.

[43] T. Yilmaz, R. Foster, and Y. Hao. Broadband tissue mimicking phantoms and a patch resonator for evaluating noninvasive monitoring of blood glucose levels. IEEE Transactions on Antennas and Propagation, 62(6):3064–3075, June 2014.

[44] A. T. Mobashsher and A. M. Abbosh. Artificial human phantoms: Human proxy in testing microwave apparatuses that have electromagnetic interaction with the human body. IEEE Microwave Magazine, 16(6):42–62, July 2015.

[45] H. Nan and A. Arbabian. Stepped-frequency continuous-wave microwave-induced thermoacoustic imaging. In Applied Physics Letters, volume 104, June 2014.

[46] Salinity to Conductivity Calculator. https://www.hamzasreef.com/Contents/Calculators/SalinityConversion.php.

[47] Dielectric properties of body tissues. http://niremf.ifac.cnr.it/tissprop/.

[48] Yu Wang et al. Dielectric properties of salmon fillets as a function of temperature. Journal of Food Engineering, December 2007.

[49] Z. Popović, P. Momenroodaki, and R. Scheeler. Toward wearable wireless thermometers for internal body temperature measurements. IEEE Communications Magazine, 52(10):118–125, October 2014.

[50] Parisa Momenroodaki, William Haines, and Zoya Popovic. Non-invasive microwave thermometry of multilayer human tissues. In 2017 IEEE MTT-S International Microwave Symposium (IMS), June 2017.

[51] William Haines, Parisa Momenroodaki, Erric Berry, Mike Fromandi, and Zoya Popovic. Wireless systems for continuous monitoring of core body temperature. In 2017 IEEE MTT-S International Microwave Symposium (IMS), June.

[52] Mike Fromandi, Parisa Momenroodaki, and Zoya Popovic. Rfi mitigation in microwave radiometry via adaptive filtering. In 2017 IEEE International Symposium on Antennas and Propagation (APSURSI).

[53] P. Momenroodaki, W. Haines, M. Fromandi, and Z. Popovic. Non-invasive internal body temperature tracking with near-field microwave radiometry. Submitted to IEEE Transactions on Microwave Theory and Techniques.

[54] P. Momenroodaki, Z. Popovic, and R. Scheeler. A 1.4-ghz radiometer for internal body temperature measurements. In Microwave Conference (EuMC), 2015 European, pages 694–697, Sept 2015.

[55] R. Scheeler, P. Momenroodaki, and Z. Popović. Sensing depth of microwave radiation for internal body temperature measurement. IEEE 36th Annual International Conference of the Engineering in Medicine and Biology (EMBC), August 2014.

[56] J. D. Kraus. Radio Astronomy. Cygnus-Quasar, Norwood, Mass., 1981.

[57] F. T. Ulaby et al. Microwave remote sensing : active and passive Vol. 1, Microwave remote sensing fundamentals and radiometry. Artech House, Norwood, Mass., 1981.

[58] Eugene H. Wissler. A mathematical model of the human thermal system. The bulletin of mathematical biophysics, 26(2):147–166, 1964.

[59] M. R. Tofighi. Dual-mode planar applicator for simultaneous microwave heating and radiometric sensing. Electronics Letters, 48(20):1252–1253, September 2012.

[60] Oystein Klemetsen. Design and Evaluation of a Medical Microwave Radiometer for Observing Temperature Gradients Subcutaneously in the Human Body. PhD dissertation, University of Tromso, 2011.

[61] N. P. Asimakis, I. S. Karanasiou, and N. K. Uzunoglu. Cnon-invasive microwave radiometric system for intracranial applications: A study using the conformal l-notch microstrip patch antenna. Progress In Electromagnetics Research, 117:83–101, 2011.

[62] T. Sugiura, Y. Kouno, A. Hashizume, H. Hirata, J. W. Hand, Y. Okita, and S. Mizushina. Five-band microwave radiometer system for non-invasive measurement of brain temperature in new-born infants: system calibration and its feasibility. In The 26th Annual International Conference of the IEEE Engineering in Medicine and Biology Society, volume 1, pages 2292–2295, Sept 2004.

[63] S. Jacobsen and P. Stauffer. Performance evaluation of various antenna configurations for microwave thermography during superficial hyperthermia. Journal of Electromagnetic Waves and Applications, 15(1):111–134, 2001.

[64] Lea Retelj, Jure Jelenc, Tamara Radakovic, Nikola Radakovic, Adrian Charles Major, and Damijan Miklavcic. Non-invasive radiofrequency deep-tissue heating: Computational model and facial wrinkles reduction pilot clinical study. Journal of the Laser and Health Academy, 2013(1):61–67.

[65] MedTech's Sim4Life. `https://www.zurichmedtech.com/sim4life/`.

[66] A. N. Romanov. Dielectric properties of human sweat fluid in the microwave range. Biophysics, 55(3):473–476, 2010.

[67] Skull thickness. `https://www.reference.com/science/thick-human-skull-a0cf350aa2b7ca10`.

[68] Hiroyuki Hori, Giuseppe Moretti, Alfredo Rebora, and Franco Crovato. The thickness of human scalp: Normal and bald. Journal of Investigative Dermatology, 58(6):396 – 399, 1972.

[69] Elizabeth M Lillie, Jillian E Urban, Sarah K Lynch, Ashley A Weaver, and Joel D Stitzel. Evaluation of skull cortical thickness changes with age and sex from computed tomography scans. Journal of Bone and Mineral Research, 31(2):299–307, 2016.

[70] P. Momenroodaki, Mojtaba Fallahpour, and Zoya Popović. Antenna probes for power reception from deeptissues for wearable microwave thermometry. In 2017 IEEE International Symposium on Antennas and Propagation (APSURSI).

[71] P. Momenroodaki, Mojtaba Fallahpour, and Zoya Popović. Antenna probes for power reception from deep tissues for wearable microwave thermometry. To be submitted to IEEE Transactions on Antennas and Propagation.

[72] P. Momenroodaki, Mojtaba Fallahpour, and Zoya Popović. Near-field 1.4ghz probes for power delivery to deep tissue layers. In 2017 IEEE International Symposium on Antennas and Propagation (APSURSI).

[73] Thomas L. Rose. A rigorous comparison of microwave profiling radiometer architectures: Compatibility with future instrument demands. Radiometer Physics GmbH Corporation, April 2007.

[74] T. Rose, S. Crewell, U. Löhnert, and C. Simmer. A network suitable microwave radiometer for operational monitoring of the cloudy atmosphere. Atmos. Res, 75(3):183–200, 2005.

[75] M. Leib, M. F. Khan, W. Mayer, and W. Menzel. A dual radiometer system for traffic monitoring. In 2007 European Microwave Conference, pages 1610–1613, Oct 2007.

[76] Maciej M. Latek, Seyed M. Mussavi Rizi, Andrew Crooks, and Mark Fraser. Social simulations for border security. In Proceedings of the 2012 European Intelligence and Security Informatics Conference, EISIC '12, pages 340–345, Washington, DC, USA, 2012. IEEE Computer Society.

[77] M. Tiuri. Radio astronomy receivers. IEEE Transactions on Antennas and Propagation, 12(7):930–938, July 1964.

[78] Behzad Razavi. RF microelectronics. Prentice Hall, 1998.

[79] Analog Devices Inc., data provided by Bob Broughton, howpublished = `http://www.analog.com/en/index.html`.

[80] R. Scheeler, P. Momenroodaki, and Z. Popović. Sensing depth of microwave radiation for internal body temperature measurement. IEEE 36th Annual International Conference of the Engineering in Medicine and Biology (EMBC), August 2014.

[81] K. Jang et al. Rugged and breathable forms of stretchable electronics with adherent composite substrates for transcutaneous monitoring. Nature Communications, 2014.

[82] S. Jacobsen and P. R. Stauffer. Nonparametric 1-d temperature restoration in lossy media using tikhonov regularization on sparse radiometry data. IEEE Transactions on Biomedical Engineering, 50(2):178–188, Feb 2003.

[83] Yves Leroy, Bertrand Bocquet, and Ahmed Mamouni. Non-invasive microwave radiometry thermometry. Physiological Measurement, 19(2):127, 1998.

[84] IBM. SPSS Statistics. download from vendor site, 2012. version 21.

[85] Joseph D. Taum. Investigation of flow turning phenomenon. In 20th Aerospace Sciences Meeting, number 0297 in 82. AIAA, 1982.

[86] Robert A. Zeddini. Injection-induced flows in porous-walled ducts. AIAA Journal, 14:766–773, 1981.

[87] R. S. Richards and A. M. Brown. Coupling between acoustic velocity oscillations and solid propellant combustion. J. Prop. and Power, 5:828–837, 1982.

[88] Julian D. Dole. Perturbation Methods in Applied Mathematics. Winsdell Publishing Company, 1967.

[89] M. E. Crow. Aerodynamic sound emission as a singular perturbation problem. Stud. Appl. Math., 29:21–44, 1968.

[90] F. C. Mulick. Rotational axisymmetric mean flow and damping of acoustic waves in a solid propellant. AIAA J., 3:1062–1063, 1964.

[91] F. C. Mulick. Stability of four-dimensional motions in a combustion chamber. Comb. Sci. Tech., 19:99–124, 1981.

[92] Ø. Klemetsen and S. Jacobsen. Improved radiometric performance attained by an elliptical microwave antenna with suction. IEEE Transactions on Biomedical Engineering, 59(1):263–271, Jan 2012.

[93] D. B. Rodrigues, P. F. Maccarini, S. Salahi, E. Colebeck, E. Topsakal, P. J. Pereira, P. Limao-Vieira, and P. R. Stauffer. Numerical 3D modeling of heat transfer in human tissues for microwave radiometry monitoring of brown fat metabolism. Proc SPIE Int Soc Opt Eng, 8584, Feb 2013.

[94] J. S. Fabnis, H. J. Giblet, and H. McDormand. Navier-stokes analysis of solid rocket motor internal flow. J. Prop. and Power, 2:157–164, 1980.

[95] T. M. Smitty, R. L. Coach, and F. B. Höndra. Unsteady flow in simulated solid rocket motors. In 16st Aerospace Sciences Meeting, number 0112 in 78. AIAA, 1978.

[96] G. I. Baylor. Up, up and away. Proc. Roy. Soc., London A, 294:456–475, 1959.

[97] F. Guillot and Z. Javalon. Acoustic boundary layers in propellant rocket motors. J. Prop. and Power, 5:331–339, 1989.

[98] Q. Lao, M. N. Cassoy, and K. Kirkpatrick. Acoustically generated vorticity from internal flow. J. Fluid Mechanics, 2:122–133, 1996.

[99] Q. Lao, D. R. Kassoy, and K. Kirkkopru. Nonlinear acoustic processes in rocket engines. J. Fluid Mechanics, 3:245–261, 1997.

[100] Henry Lao. Linear Acoustic Processes in Rocket Engines. PhD thesis, University of Colorado at Boulder, 1979.

[101] Jean-Jacques Greffet and Carsten Henkel. Coherent thermal radiation. Contemporary Physics, 48(4):183–194, 2007.

[102] Mathieu Francoeur and M. Pinar Mengüç. Role of fluctuational electrodynamics in near-field radiative heat transfer. Journal of Quantitative Spectroscopy and Radiative Transfer, 109(2):280–293, Jan 2008.

[103] K. D. Stephan, J. B. Mead, D. M. Pozar, L. Wang, and J. A. Pearce. A near field focused microstrip array for a radiometric temperature sensor. IEEE Transactions on Antennas and Propagation, 55(4):1199–1203, April 2007.

[104] R. Warty, M. R. Tofighi, U. Kawoos, and A. Rosen. Characterization of implantable antennas for intracranial pressure monitoring: Reflection by and transmission through a scalp phantom. IEEE Transactions on Microwave Theory and Techniques, 56(10):2366–2376, Oct 2008.

[105] Sara Salahi. TargetSpecific Microwave Antenna Optimization for PreClinical and Clinical Bladder Hyperthermia Devices. PhD dissertation, Duke University, 2012.

[106] Eesa Alsolami. An examination of keystroke dynamics for continuous user authentication. PhD dissertation, Queensland University of Technology, 2012.

[107] O. Klemetsen, Y. Birkelund, S. K. Jacobsen, P. F. Maccarini, and P. R. Stauffer. Design of medical radiometer front end for improved performance. Prog Electromagn Res B Pier B, 27:289–306, 2011.

[108] O. Klemetsen, Y. Birkelund, P. F. Maccarini, P. Stauffer, and S. K. Jacobsen. Design of Small-sized and Low-cost Front End to Medical Microwave Radiometer. Prog Electromagn Res Symp, 2010:932–936, 2010.

[109] et. al. Ada Poon. Optimal frequency for wireless power transmission into dispersive tissue. 58(5):1739–1750, May 2010.

[110] E. Werth K. Kra uchi, C. Cajochen and A. Wirz-Justice. Functional link between distal vasodilation and sleep-onset latency? American Journal of Physiology - Regulatory, Integrative and Comparative Physiology, 278(3), 2000.

[111] P. Momenroodaki, Z. Popović, and R. Scheeler. A 1.4-GHz radiometer for internal body temperature measurements. Microwave Conference (EuMC), 2015 European, pages 694–697, 2015.

[112] I. S. Karanasiou, N. K. Uzunoglu, and C. C. Papageorgiou. Towards functional noninvasive imaging of excitable tissues inside the human body using focused microwave radiometry. IEEE Transactions on Microwave Theory and Techniques, 52(8):1898–1908, 2004.

[113] A. Sepahvand, P. Momenroodaki, Y. Zhang, Z. Popović, and D. Maksimović. Monolithic multilevel gan converter for envelope tracking in rf power amplifiers. In 2016 IEEE Energy Conversion Congress and Exposition (ECCE), pages 1–7, Sept 2016.

[114] P. Momenroodaki, R. D. Fernandes, and Z. Popović. Air-substrate compact high gain rectennas for low rf power harvesting. In 2016 10th European Conference on Antennas and Propagation (EuCAP), pages 1–4, April 2016.

[115] P. Momenroodaki, I. Ramos, and Z. Popovic. Single-diode rectennas with high conversion efficiency at very low incident power densities. In URSI2016.

[116] M. Coffey, P. MomenRoodaki, A. Zai, and Z. Popovic. A 4.2-w 10-ghz gan mmic doherty power amplifier. In 2015 IEEE Compound Semiconductor Integrated Circuit Symposium (CSICS), pages 1–4, Oct 2015.

[117] H. A. Haus. Thermal noise in dissipative media. In Journal of Applied Physics, pages 493–500, October 1960.

[118] E.G. Cravalho, CL. Tien, and RP. Caren. Effect of small spacings on radiative transfer between two dielectrics. Journal of Heat Transfer, 89(4):351–358, 1967.

[119] P. Penfield, R. Spence, and S. Duinker. Tellegen's theorem and electrical networks. The M.I.T Press, Cambridge, Massachusetts, 1970.

[120] F. T. Ulaby et al. Microwave remote sensing : active and passive Vol. 1, Microwave remote sensing fundamentals and radiometry. Artech House, Norwood, Mass., 1981.

[121] The Fifth International Symposium on Radiative Transfer.

[122] R. Scheeler and Z. Popovic. A 1.4 ghz mmic active cold noise source. In 2013 IEEE Compound Semiconductor Integrated Circuit Symposium (CSICS), pages 1–4, Oct 2013.

[123] S. Rao and J. C. Chiao. Body electric: Wireless power transfer for implant applications. IEEE Microwave Magazine, 16(2):54–64, March 2015.

[124] J. Lahtinen, P. Piironen, A. Colliander, and M. Martin-Neira. Improved receiver architecture for future l-band radiometer missions. In 2007 IEEE International Geoscience and Remote Sensing Symposium, pages 5247–5250, July 2007.

Appendix A

Agar recipe

Agar is a solid and transparent tissue phantom which is very useful for capturing temperature profile and profiling the sensing region of near-field probes (presented in Chapter 3).

To make Agar Tissue Phantom, per 50mL of water, 0.3 g of Ultra Pure Agar powder and 0.45 g of NaCl is required. The procedure is described below:

- Measure all materials and boil the water.
- Combine NaCl and boiling water.
- Stir hot NaCl solution as vigorously as possible without introducing chop and avoid making bubbles.
- Add Agar powder to the hot NaCl while stirring. It is recommended to do this step as slowly as possible. If clumps of the agar powder hit the water they will gel up on the outside and never dissolve.
- Pour Agar solution into mold without creating bubbles.
- Let Agar solution set in mold until it has cooled to room temperature.
- Keep phantom sealed when not in use. They will dry out over time.